School of Science

Department of Imaging and Applied Physics

Hydrogen Storage Studies of Nanoparticulate Al and TiMn Based Compounds

Julie Andrianny Murshidi

This thesis is presented for the Degree of

Doctor of Philosophy

of

Curtin University

September 2012

DECLARATION

"To the best of my knowledge and belief this thesis contains no material previously published by any other person except where due acknowledgement has been made. This thesis contains no material which has been accepted for the award of any other degree or diploma in any thesis".

Julie Andrianny Murshidi

Signature:

Date: 27st September 2012

ABSTRACT

Concerns about the impact that fossil fuels have on the environment and their increasing price to the consumer have led to research being undertaken to evaluate and refine other energy carriers that will be comparable to fossil fuels. Significant interest has been associated with hydrogen. Hydrogen is widely known as a promising energy carrier for the transportation sector. However at present no known material or storage means exists that satisfies all requirements to enable high-volume automotive application. Transition to using hydrogen storage technology in vehicles might first include its implementation in specialty vehicles, portable power supply and stationary power supply. Due to this fact, research into materials based hydrogen storage has grown significantly over the past decade. Of the wide variety of materials based hydrogen storage, three different materials were chosen as the primary focus of this project; (1) Aluminium nanoparticles, (2) AlH_3 nanoparticles and (3) TiMn alloy.

Al nanoparticles were synthesised by mechanochemical reactions of $AlCl_3 + 3Li \rightarrow Al + 3LiCl$ using different LiCl:Al volume ratios (6.786:1 , 9.665:1 and 12.544:1). LiCl was used as the buffer. Sample synthesised without the addition of buffer led to the formation of Al nanoparticles with an average particle size of 50 nm. Addition of sufficient quantity of buffer resulted in the formation of Al with average particle sizes down to 13 nm. The addition of LiCl as a buffer helps to separate the synthesized Al particles, essentially restricting particle growth and promoting nanoparticle formation. Attempted hydrogenation of Al nanoparticles (13 nm) using a mixed $H_2/scCO_2$ media showed no H_2 absorption. This indicates that an Al particle size less than (13 nm) is required to introduce hydrogen into pure Al at pressure and temperature attempt herein (73.8 bar and 31.1°C). Furthermore the presence of oxide layer (Al_2O_3) on Al nanoparticles during $scCO_2/H_2$ reaction limited the rate of hydrogen permeation on Al nanoparticles.

AlH_3 nanoparticles were synthesised by mechanochemical reactions of the $3LiAlH_4$ + $AlCl_3$ using different $LiCl:AlH_3$ volume ratios (0.76:1, 2:1, 5:1 and 10:1) at 77 K. The addition of LiCl as a buffer leads to the reduction of the synthesized AlH_3 crystallite size, restricting AlH_3 decomposition and preventing high Al yields. Quantitative Rietveld results coupled with hydrogen desorption measurements suggest the presence of an amorphous AlH_3 phase in mechanochemically synthesized samples. TEM results show that the synthesized AlH_3 comprised of 10 - 30 nm particle size range. For hydrogen desorption measurements, it is clear that AlH_3 particle size reduction when ball milling using buffer does effectively increase the H desorption rate compared to the case without using buffer. For hydrogen absorption measurements, decomposed AlH_3 nanoparticles with 10 - 30 nm in size underwent pressures of 280 bar at -196 °C, 1420 bar at 25°C, 1532 bar at 50°C, 1734 bar at 100°C and 1967 bar at 150°C with no hydrogen absorption was detected.

Ti-Mn alloy compounds with the composition $TiMn_2$, $Ti_{0.97}Zr_{0.019}Mn_{1.5}Cr_{0.57}$ and $Ti_{0.7875}Zr_{0.2625}Mn_{0.8}Cr_{1.2}$ were synthesised and compared to the commercially available $Ti_{0.97}Zr_{0.019}V_{0.439}Fe_{0.097}Cr_{0.045}Al_{0.026}Mn_{1.5}$ alloy composition. An amorphous Ti-Mn alloy was formed when the starting reagents were mechanical alloying for 40 h. The corresponding crystalline phase TiMn was formed when the amorphous alloy was annealed at 800°C. The addition of a process control agent (Toluene) leads to the formation of a carbide phase (TiC) in the samples. The presence of impurities, carbide (TiC) and oxide (TiO) phases resulted a decrease in C14 laves phase wt.% in the synthesised samples. Only 37.24, 31.5 and 32.81 wt.% C14 phase was formed in $TiMn_2$, $Ti_{0.97}Zr_{0.019}Mn_{1.5}Cr_{0.57}$ and $Ti_{0.7875}Zr_{0.2625}Mn_{0.8}Cr_{1.2}$ respectively. The result also showed that the theoretical value of 1.9 hydrogen wt.% could not be reached by these samples.

TABLE OF CONTENTS

CHAPTER 5: TITANIUM MANGANESE ALLOY

LIST OF FIGURES

LIST OF TABLES

ACKNOWLEDGEMENTS

In the name of Allah, the Most Gracious and the Most Merciful

Alhamdulillah, all praises to Allah for the strengths and His blessing in completing this Ph.D. thesis.

Special appreciation goes to my supervisor, Prof. Craig Buckley, for his supervision and constant support. His invaluable help of constructive comments and suggestions throughout the experimental and thesis works have contributed to the success of this research. Not forgotten, my appreciation to my co-supervisor, Dr. Mark Paskevicius for all his support and knowledge regarding this topic.

A special thank you is given to the Malaysian Government and Ministry of Science, Technology and Innovation Malaysia (MOSTI) for awarding me with a Ph.D. scholarship.

I would like to express my appreciation to: All the office staffs and technicians in the Department of Imaging and Applied Physics for their co-operations. Dr. Drew Sheppard for his technical help, information and discussions. Glen Lawson for providing valuable assistance in all things lab-based. Ross Williams for his help with XRD analysis. Dr. Martin Saunders, Dr. Rob Hart and Tony for their assistance with TEM investigations. Elaine Miller and William Rickard for their help with SEM investigations.

Sincere thanks to all my friends especially Anna Lisa, Teoh, Nurul, Somwan, Abdullah, Hatem and others for their kindness and moral support during my study. Thanks for the friendship and memories.

Last but not least, my deepest gratitude goes to my beloved parents Mr. Hj. Murshidi Mat and Mrs. Hjh. Bibi Mansor and my darling husband Ir. Musalkurnain Md Zin for their endless love, prayers, encouragement and understanding. For my beautiful children, Muhammad Adam Danial and Mayeda Fahima this is my special present for both of you.

To those who indirectly contributed in this research, your kindness means a lot to me. Thank you very much.

COPYRIGHT DECLARATION

"I warrant that I have obtained, where necessary, permission from the copyright owners to use any third-party copyright material reproduced in the thesis, or to use any of my own work in which copyright is held by another party".

Julie Andrianny Murshidi

Signature:

Date: 27st September 2012

CHAPTER 1: Introduction and Overview

1.1 Introduction to Project

There are currently concerns about the impact that fossil fuels have on the environment and their increasing price to the consumer. These concerns have led to research being undertaken to evaluate and refine other energy carriers that will be comparable to these fossil fuels. Significant interest has been associated with hydrogen[1-4].

Great potential for diversity of supply is an important reason why hydrogen is such a potential solution to our energy security needs. Hydrogen can be produced using abundant and diverse domestic resources, including fossil sources, biological methods, nuclear energy and renewable energy sources[1-4]. Hydrogen can be converted to water, generating energy without releasing harmful emissions, thus reducing greenhouse gas emissions, pollutants and our dependence on fossil fuels.

The chemical energy per mass of the H_2 (120 MJ kg^{-1}) is approximately three times greater than that of other chemical fuels (e.g., on average the equivalent value for liquid hydrocarbons is 43 MJ kg^{-1})[5]. However the energy density of hydrogen (on volumetric basis) is very low compared to gasoline or other hydrocarbons. For example, 1 L of gasoline (31.7 MJ/L, 8.8 kWh/L) contains approximately six times as much energy as a litre of hydrogen compressed to 70 MPa (4.7 MJ/L, 1.3 kWh/L)[5]. Materials based hydrogen storage has demonstrated the ability to increase the density of hydrogen by a factor of more than twice that of liquid hydrogen, resulting in hydrogen densities of up to 21.1 MJ/L hydrogen[5].

Hydrogen is widely known as a promising energy carrier for the transportation sector. However, at present, no known material or storage means exists that satisfies all requirements to enable high-volume automotive application such as the ability to store

hydrogen at adequate densities as well as release hydrogen at sufficient rates. According to the US Department of Energy (D.O.E.)[6-8], transition to using hydrogen storage technology in vehicles might first include its implementation in specialty vehicles (forklifts, mining vehicles and airport ground support), portable power supply (laptops, mobile phones, emergency lights and military radios) and stationary power supply (remote-area power supply (RAPS), uninterrupted power supply (UPS) and renewable energy storage system). Due to this fact, research into materials based hydrogen storage has grown significantly over the past decade[5,9-11].

1.1.1 Project Aims and Significance

The primary focus of this project was to synthesise and to investigate the properties of nanoparticles (Al and AlH_3) and intermetallic compounds (TiMn alloys) as suitable candidates for material based hydrogen storage (hydride materials) in specialty vehicles, portable power supply and stationary power supply applications. For this type of application, the location between hydride material and fuel cell (Fig. 1-1) or the location of the hydride material between an electrolyser and a fuel cell (Fig. 1-2) sets rather strict boundary conditions for the performance of the hydride material. The selected fuel cell operates at atmospheric pressure therefore it must be possible to discharge the hydride against a 1 bar pressure with minimum operating temperature (10 - 70°C)[2,12,13]. On the other hand the maximum charging pressure is limited by the electrolyser. The maximum charging pressure was reported to be in the 10 - 20 bar[14] range but with present electrolyser technology, this charging pressure can be achieved at 30 - 70 bar[15,16]. Therefore a suitable metal hydride should be able to operate at the temperatures and pressures that the electrolyser and fuel cell require.

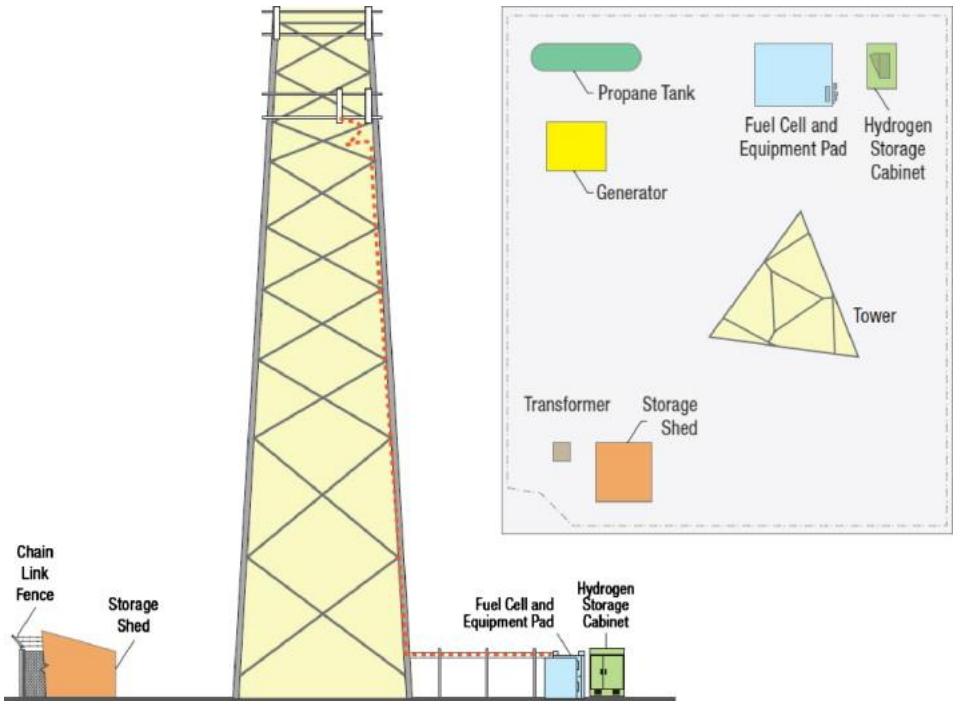

Figure 1- 1.Schematic of a typical telecommunication back-up power system[5].

For renewable energy-hydrogen systems (Fig. 1-2), solar and wind energy can be used to produce hydrogen by water electrolysis[14,17-19]. Water electrolysis is a method for converting electrical energy into a chemical form. The power required for hydrogen production can be supplied through a solar photovoltaic (PV) array or wind turbine. Hydrogen produced can be stored in metal hydrides and later can be converted back into electricity using a fuel cell. This electricity can be used to supply a load greater than the PV and wind turbine can supply alone. Unfortunately, solar and wind energy are not reliable because of their dependence on natural phenomena. Solar energy is not available at night or during cloudy conditions. Wind energy is also available intermittently and with variable capacity. This makes it difficult to obtain a continuous energy flow, and consequently the impossibility of supplying the time-varying load demand of the users in different locations. So the advantage of an energy storage system is that the energy can be stored as hydrogen that can be stored for a long period

of time to overcome the intermittence of renewable energy sources. In addition, when the system is in operation it has zero greenhouse gas emissions. The system is classified as a stand-alone power supply system because the power supply to a household does not need to be connected to the main electricity grid. For other portable and stationary back-up power applications (Fig. 1-1), the system consists of a hydride material, fuel cell and battery/capacitor without using an electrolyser[5]. Compared to batteries and generators, fuel cells offer longer continuous run time, lower maintenance costs and greater durability in harsh environments over a wider range of temperatures [5,20].

For specialty vehicles applications, the system consists of a hydride material, fuel cell, balance of plant (BOP) components, along with a battery/ultra capacitor to provide additional power for start-up, heavy lifting and pushing transients[5]. This system involves movement of materials and equipment from one work station to another[5,12]. The operational time of these types of vehicles can vary significantly over a shift, ranging from a few hours to 24 hours per day. The power load during operation is generally somewhat transient where the load varies over each operational shift.

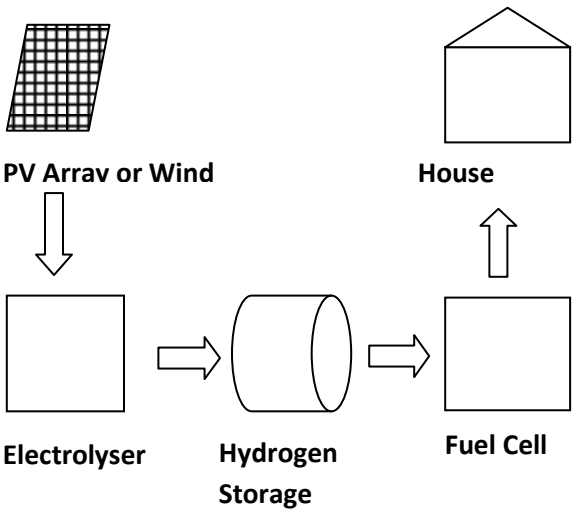

Figure 1- 2.Schematic of a typical renewable energy-hydrogen system.

For Al and AlH_3 nanoparticles

- To synthesise nanoparticles (Al and AlH_3) via mechanochemical techniques. The objective is to decrease the hydrogenation pressure from 28 kbar (this pressure is much too high to be of practical use) using a supercritical solution of CO_2 mixed with hydrogen and to systematically measure the relationship between particle size and hydrogen storage properties of the synthesized nanoparticles in the size ranges of 1 – 100 nm (the thermodynamic and kinetic properties of Al-H system are expected to be altered by particle size) to make it suitable for portable and stationary back-up power applications.

For Intermetallic compounds:

- To synthesise intermetallic compounds (TiMn alloys) via mechanical alloying techniques. The objective is to optimize the pressure, temperature, kinetics and cycling characteristics of low wt.% materials to make it suitable for a stationary renewable energy storage system coupled with an electrolyser.

1.1.2 Research Plan

Based on the significance and objectives mentioned in the previous section, the proposed research plans were as follows:

- Synthesised nanoparticles (Al and AlH_3)
    - To investigate the effect of using different buffer amount and milling time in synthesizing nanoparticles by using x-ray diffraction (XRD), scanning electron microscopy (SEM), transmission electron microscopy (TEM), energy dispersive spectrometer (EDS) and small angle x-ray scattering (SAXS).

- To investigate the hydriding properties (thermodynamic and kinetics of absorption and desorption) by using supercritical fluid chromatography (SCF) and high pressure hydrogen absorption.

- Synthesised intermetallic compounds (TiMn alloys)

Prior to synthesising TiMn intermetallic compounds, the commercial alloy ($Ti_{0.97}Zr_{0.019}V_{0.439}Fe_{0.097}Cr_{0.045}Al_{0.026}Mn_{1.5}$) was characterized with respect to its structure, morphology and hydriding properties in order to understand the effect of substituting Zr for the Ti site and V, Fe, Cr and Al for the Mn site within TiMn alloy. Based on these results, different TiMn alloy compositions and its partial substitution were synthesised.

- To investigate the effect of using process control agent (PCA) and different ball to powder ratio (BPR) in synthesising intermetallic compounds by using x-ray diffraction (XRD), scanning electron microscopy (SEM) and energy dispersive spectrometer (EDS).
- To investigate the effect of different alloy compositions and partial substitution in their crystal structure, phase component and hydriding properties by using x-ray diffraction (XRD), manual rig and automatic rig.

1.2 Electrolyser

Electrolysis is the route of a direct electric current through an ionic substance (either molten or dissolved in a suitable solvent), resulting in chemical reactions at the electrodes and separation of materials (Fig. 1-3). The main components required to achieve electrolysis are an electrolyte, a direct current (DC) supply and two electrodes.

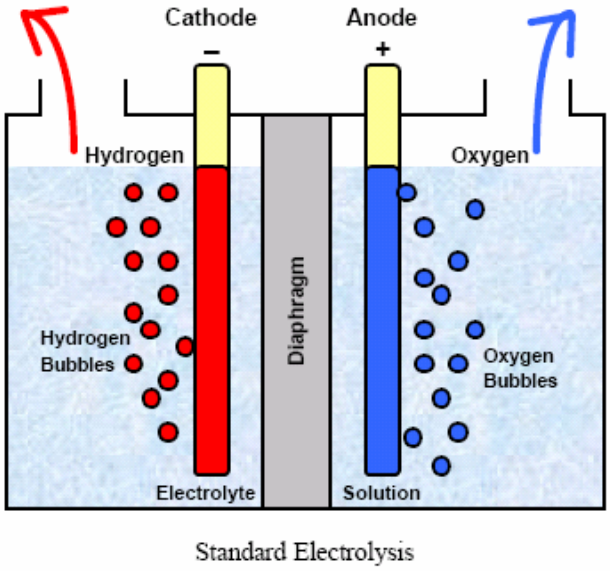

Figure 1- 3.Schematic of an electrolysis cell[21].

At the moment most commercial electrolysers (Table 1-1) use two different technologies which are alkaline and proton exchange membrane solid polymer (PEM) electrolysis (Figure 1-4 and Table 1-2)[22].

Table 1- 1:Commercially available electrolysis units[23,24].

Company	Technology	Operating Range Available Today			
		System Energy Requirement (kWh/kg)	H_2 Production Rate (kg/yr)	Power Required for Max. H_2 Production Rate (kW)	H_2 Product Pressure (bar)
Avalence	Unipolar Alkaline	56.4 - 60.5	320 - 3600	2 - 25	Up to 690
Proton	PEM	62.3 - 70.1	400-7900	3 - 63	~14
Teledyne	Bipolar Alkaline	59.0 - 67.9	2200-33,000	17 - 240	5 - 8
Stuart	Bipolar Alkaline	53.4 - 54.5	2400-71000	15 - 360	25
Norsk Hydro	Bipolar Alkaline (high pressure)	53.4	7900-47,000	48 - 290	~16
Hystruc	PEM	-	-	-	~31

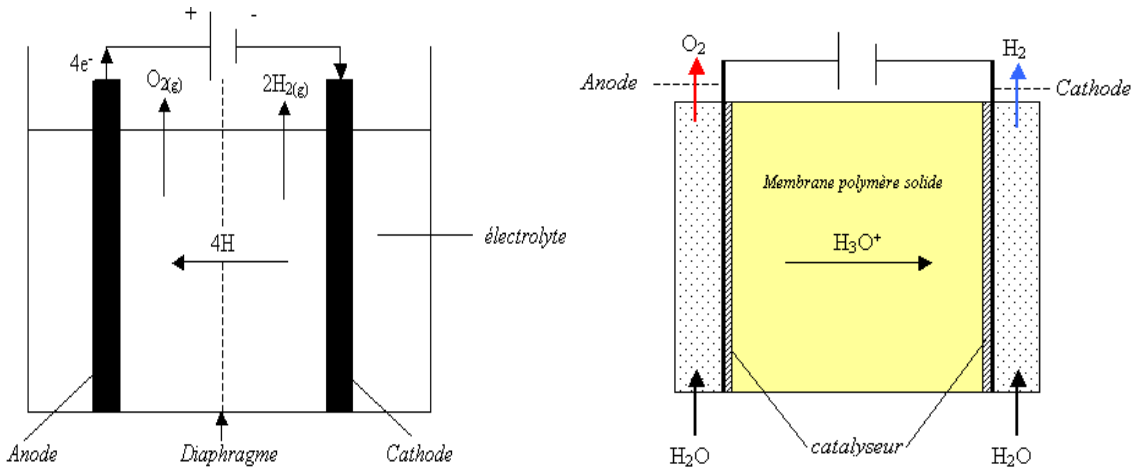

Figure 1- 4 Principle of operation[22].

Table 1- 2:Technical data of alkaline and PEM electrolyser[22].

Type	Temperature of operation (°C)	Pressure of operation(bar)	Electric consumption (kWh / Nm^3 of H_2)	Energy Efficiency (%)	Life duration (years)	State of development
Alkaline	50 - 100	3 - 30	4 - 5	75 - 90	15 - 20	marketed
PEM	80 - 100	1 - 70	6	80 - 90	~17	development

1.3 Fuel Cell

Fuel cells are electrochemical devices that directly convert chemical energy stored in fuels such as hydrogen to electrical energy and they produce only water as reaction product (Fig. 1-5)[25]. The cell consists of two electrodes that are separated by an electrolyte. The electrodes are connected through an external circuit. Hydrogen is oxidized at the negative electrode (the anode) according to equation (1.1)[2]. The protons formed enter the electrolyte and are transported to the cathode. At the positive electrode (cathode) oxygen reacts according to equation (1.2)[2]. Electrons flow in the external circuit during these reactions. The oxygen ions recombine with protons to form water as shown in equation (1.3)[2]. The reaction product water has to be removed from the cell[2].

$$\mathbf{H_2 \rightarrow 2H^+ + 2e^-} \qquad \mathbf{(1.\ 1)}$$

$$\mathbf{O_2 + 4e^- \rightarrow 2O^{2-}} \qquad \mathbf{(1.\ 2)}$$

$$\mathbf{O^{2-} + 2H^+ \rightarrow H_2O} \qquad \mathbf{(1.\ 3)}$$

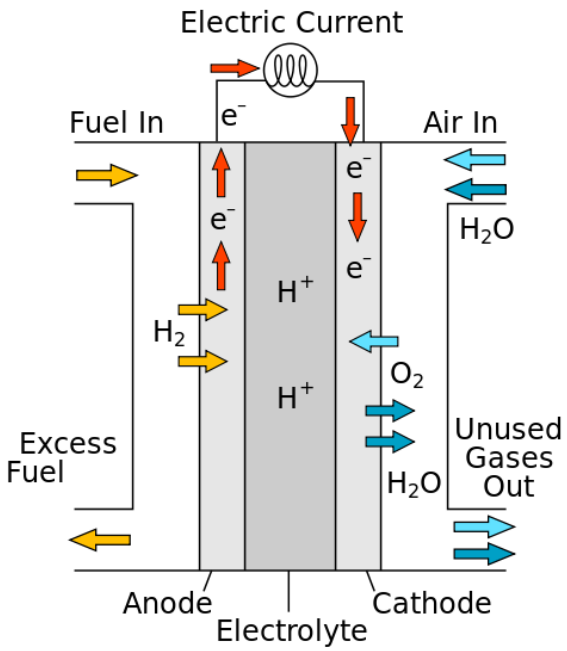

Figure 1- 5.Schematic of a PEM fuel cell[25].

1.3.1 History

In 1839, Sir William Robert Grove invented the first fuel cell[26]. In 1950s, General Electric Company (GE) began developing fuel cells and in 1962 the company was awarded the contract for the Gemini space mission[12]. The 1 kW Gemini fuel cell system had a platinum loading of 35 mg Pt/cm^2 and performance of 37 mA/cm^2 at 0.78 V[27]. In 1960s improvement were made by incorporating Teflon in the catalyst layer directly adjacent to the electrolyte, as was done with the GE fuel cell at the time[12]. Early 1970s onward, a fluorinated Nafion® membrane was fully adopted[12]. Research and development in PEMFCs did not receive much attention and funding from the federal government, in particular the U.S. Department of Energy (D.O.E.) and industry until a couple of decades ago or so when a breakthrough method for reducing the amount of platinum required for PEMFC were developed and subsequently improved by Los Alamos National Laboratory (LANL) and others[12]. This breakthrough method made it possible to increase

the utilization of active catalyst and at the same time to reduce the amount of precious platinum metal needed. Though many technical and associated fundamental breakthroughs have been achieved during the last couple of decades, many challenges such as reducing cost and improving durability while maintaining performance remain prior to the commercialization of PEM fuel cells[2,12].

1.3.2 Types of Fuel Cell

Four categories of fuel cells with pure hydrogen as the fuel are alkaline fuel cells (AFCs), phosphoric acid fuel cells (PAFCs), direct methanol fuel cells (DMFCs) and polymer electrolyte membrane (PEM/PEMFCs/PEFCs) fuel cells[2,12]. Among these fuel cells, the PEM fuel cell is a promising candidate as a next generation power source due to its properties such as low operating temperature, high power density and easy scale-up[2,12]. The four types of fuel cells are shown in Table 1-3.

Table 1- 3:The summary of the four types of fuel cells[2].

Type	Electrolyte	Temperature of operation (°)
PAFC	Phosphoric acid	150 - 200
DMFC	Methanol	60 - 120
PEM/PEMFC/PEFC	Proton exchange membrane	40 - 90
AFC	Potassium hydroxide solution	<80

1.3.3 Applications of PEM fuel cell technology and its current status

Several reports have identified numerous near-term, non-automotive markets for the successful application of hydrogen and fuel cells including stationary, portable and specialty vehicles[5,12,28]. In these studies, the power of an electric passenger car, utility vehicles and buses range from 20 kW to 250 kW[5]. The stationary power provided by general fuel cells has a wide range, 1 - 50 MW[5]. Some small-scale stationary generation is 1 - 100 kW. The portable power is usually in the range of 5 - 50 W[5]. Appendix B shows a list of major companies in this fuel cell transportation, small stationary and portable sector[29-32]. The DOE recognizes that likely routes for commercialization of direct hydrogen fuel cells in vehicles, portable power supply and stationary power supply applications that may have fewer technical challenges than automobiles and therefore are expected to be more readily deployed[5,12].

1.4 Metal Hydride Storage

1.4.1 Introduction

Hydrogen can be stored as[2]:

- Physical storage of compressed hydrogen gas in high pressure tanks (up to 70 MPa).
- Physical storage of cryogenic liquid hydrogen (cooled to -253°C) in insulated tanks.
- Storage in advanced material – on the surface (physisorption / adsorption) or within the structure (chemisorptions / absorption) of certain materials, as well as in the form of chemical precursors that undergo a chemical reaction

to release hydrogen. The potential energy (Fig. 1-6) shows a shallow minimum for physisorbed hydrogen, a deep minimum for chemisorbed dissociated hydrogen, a rather deep minimum for near surface hydrogen and periodic minima for hydrogen dissolved on interstitial site for the host metal separated from each other by diffusion barriers[33].

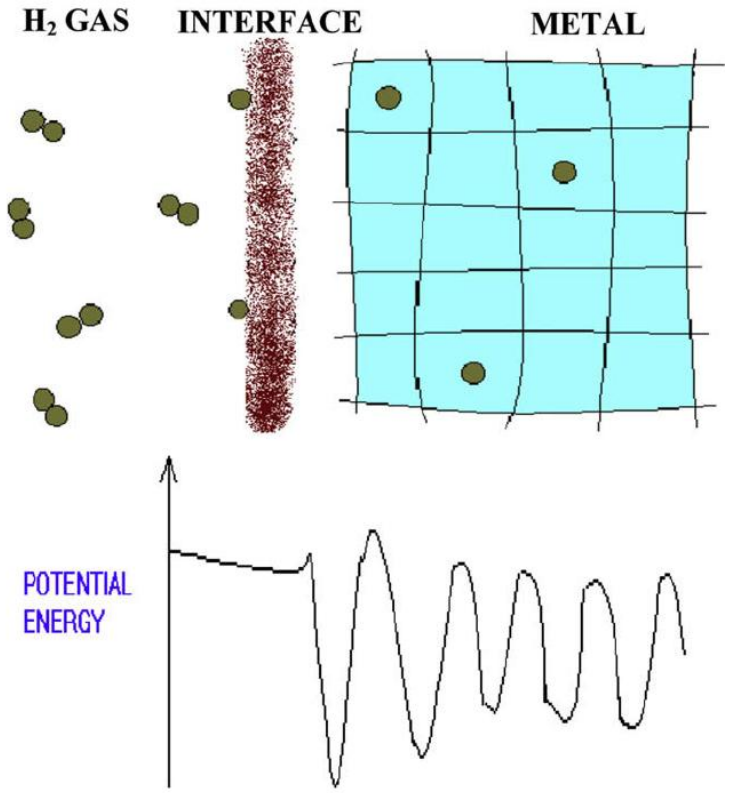

Figure 1- 6.Schematic potential energy for dissociation of molecular hydrogen at an interface and the solution of hydrogen atoms in the bulk[33].

In other words, metal hydrides can be visualized as materials which are capable of functioning like a “sponge” for absorbing and “squeezing out” hydrogen, the mechanical action being provided by small change in temperature and pressure[33].

1.4.2 PCT

The metal-hydrogen system consists of a metallic material, hydrogen gas and an interface region between them as shown in equation (1.4)[34].

$$\mathbf{M} + \left(\mathbf{X}/\mathbf{2}\right)\mathbf{H_2} \leftrightarrow \mathbf{MH_x} + \mathbf{Heat} \qquad \textbf{(1. 4)}$$

Hydrogen gas adsorbs onto the interface region. At the interface, the molecules are dissociated into individual hydrogen atoms that can absorb or dissolve into the metal phase. The random dissolution of hydrogen atoms in the metal phase is known as the α-phase. Within the metallic phase, the hydrogen atoms can start to arrange themselves in a specific configuration with the metal atom, forming the metal hydride phase, called the β-phase. Where and how the β-phase is nucleated and grows is a characteristic of the material[35,36].

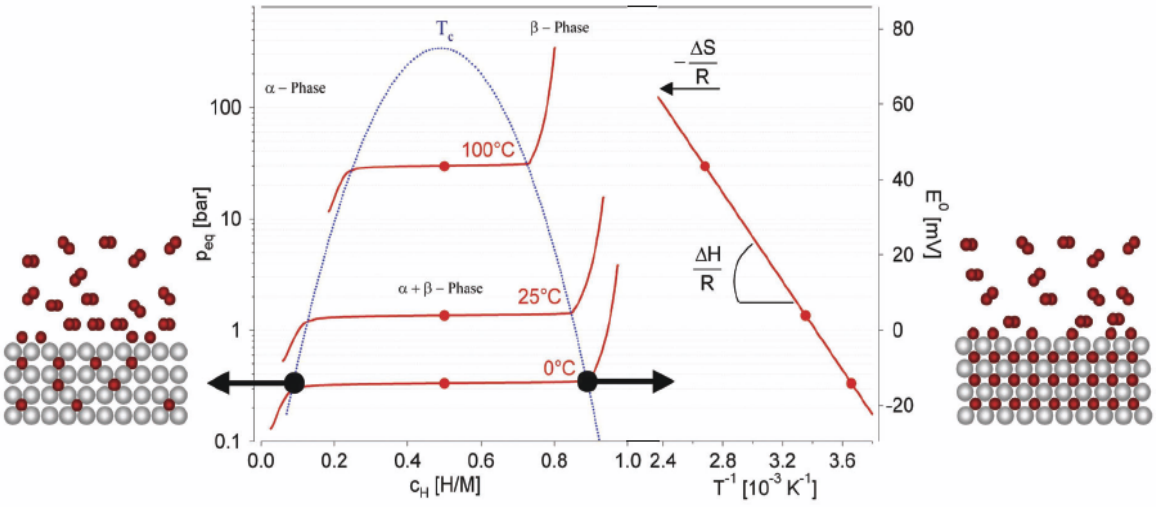

Figure 1- 7.Pressure-concentration-temperature plot of a typical hydrogen absorption or desorption process (left) and van't Hoff curve (right)[36].

As long as the solid solution and the hydride coexist, the PCT curves (hydrogen pressure at a given temperature as a function of hydrogen concentration in the material) present a plateau. The length of this plateau represents the hydrogen amount which can be reversibly stored at that temperature by small pressure changes. When the $\alpha \rightarrow \beta$ transition is completed, the hydrogen pressure again increases sharply with the concentration. The region of the diagram where the two phases coexist ends at a critical point T_c, over which the $\alpha \rightarrow \beta$ transition is direct[37]. The equilibrium pressure is related to the entropy and enthalpy by the van't Hoff equation that is plotted in the right section of Fig.1-7[36]. When examining whether or not a particular metal hydride is suited to some applications, the temperature and pressure properties can be analysed in a van't Hoff plot. The van't Hoff equation (equation 1.5) related the equilibrium fugacity of hydrogen gas (f_{eq} in bar), a reference fugacity (f_0) constant of 1 bar, the change in enthalpy (ΔH) between the hydride phase and non-hydride and hydrogen phases (J/mol H_2), the change in entropy (ΔS) between the hydride phase and non-hydride and hydrogen phases (J/mol H_2/K), the gas constant (R = 8.314472 J/mol/K), and the temperature (T) in K[36,38]. It should be noted that the van't Hoff equation is often provided in the literature with a pressure term replacing the fugacity term in equation (1.5), which is not strictly correct and only valid at very low pressure where the ideal gas law can be assumed valid[38,39]**.** The fugacity (f) is the activity of the real gas which provides a better representation of the chemical potential of the system then pressure (p) itself.

$$\ln\left(\frac{f_{eq}}{f_0}\right) = \frac{\Delta H}{RT} - \frac{\Delta S}{R} \qquad \textbf{(1.5)}$$

van't Hoff plots are very useful in the selection of metal hydrides as they clearly show which metal hydrides have the operating temperatures and pressures desired for a particular application. However, the representative of the van't Hoff equation as a single

straight line is not correct, as effects such as hysteresis and plateau sloping give experimental van't Hoff plots as a series of lines.

1.4.3 Activation

Activation is the procedure needed to hydride a metal the first time and to bring it up to maximum H-capacity and hydriding-dehydriding kinetics. The ease of H_2-penetration depends on surface structure and barriers, such as dissociation catalytic species and oxide films. A second stage of activation involves internal cracking of metal particles to increase reaction surface area[34,40].

1.4.4 Kinetics

The kinetics of hydride material involves the rate and mechanism(s) in hydrogen uptake and release. The mechanisms are includes surface interactions, mass transport phenomena and nucleation[5]. These mechanisms could act as the kinetic barrier. Kinetics of hydriding and dehydriding can vary markedly from alloy to alloy[34]. Many room temperature hydrides have excellent intrinsic kinetics, so that the cycling of storage containers tends to be limited by heat transfer designs or accidental surface contamination[34]. There are some materials that are kinetically limited, especially at low temperature[34]**.** Catalysts can also be added to metal hydride mixtures to aid the activation process if necessary[41]. The metal hydrides chosen for this system must have moderately high reaction kinetics at the chosen operating conditions, so that the cycling metal hydride can occur in a reasonable time period. For special vehicles, portable and static applications, the time to refuel the supply is not a critical as automobile applications[5]. Refueling may be accomplished off-board where the hydrogen fuel can

simply be exchanged. However, hydrogen release rates and conditions may be very similar to that of an automobile where the storage material should supply a hydrogen pressure of at least 0.5 MPa to fuel cell[5].

1.4.5 Cyclic Stability

Alloys and intermetallic compounds are usually metastable and may disproportionate, which is the tendency to break up metallurgically to form stable, not easily reversed hydrides[34]. Even if very pure hydrogen is used, disproportionation can occur with a resultant loss of reversible capacity[34]. However, experimentation has shown that disproportionation can be reduced by heating of the metal hydride to temperatures above the operating conditions that originally produced the decrepitation[42,43]. Metal hydrides can experience a decrease in the amount of hydrogen they can absorb as they undergo extended cycling[44,45]. For the system to be sustainable and economically viable, it is necessary that the metal hydrides chosen have a high level of cyclic stability. The cyclic stability of the chosen metal hydrides will dictate the length of time for which the system can cycle without need of maintenance or replacement of components.

1.4.6 Hysteresis

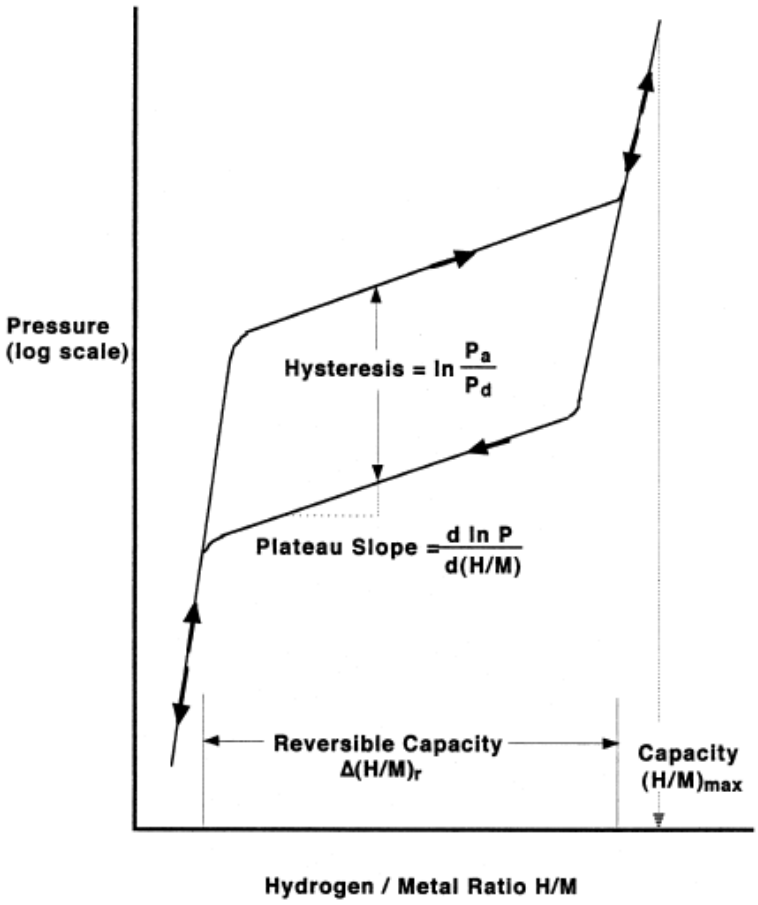

Figure 1- 8.Isothermal pressure-composition hysteresis loop [34].

Many metals experience hysteresis as they cycle (Fig.1-8), where the pressure of the hydrogenation reaction is different to that of the dehydrogenation reaction. Hysteresis is affected by the history of a sample as well as the way it was prepared, so there can be differences in the hysteresis of the same metal hydride, based on these properties[40].

1.4.7 Cost

For material-based hydrogen storage to be a practical alternative for near-term markets, the cost of the materials must be competitive with that of storage in high pressure cylinders. In addition, the hydrogen-fuel cell system must be competitive with other forms of energy such as petroleum and diesel generators or batteries. According to the London Metal Exchange, the price for Al is about $3.04/kg[46]. For an alloy, the cost is influenced by several factors including the raw material cost, melting and annealing cost, metallurgical complexities, profit and the degree of PCT precision needed for the particular application[10,34]. For the TiMn alloy, the raw material costs are relatively inexpensive, with the exception of titanium. However ferro-titanium ($8.70/kg) is less expensive than pure titanium ($27.50/kg)[47]. Therefore having a hydrogen storage alloy with Ti and Fe components allows for a reduced system cost.

1.5 Nanoparticles

1.5.1 Properties

Nanomaterials can be classified into nanocrystalline materials and nanoparticles. Nanocrystalline materials are polycrystalline bulk materials with grain sizes in the nanometers range (less than 100 nm), while nanoparticles refer to ultrafine dispersive particles with diameters below 100 nm[48]. Fig. 1-9 shows the two possible geometrical outcomes of the combined X-ray lineshape/TEM measurement technique for nanomaterials[49].

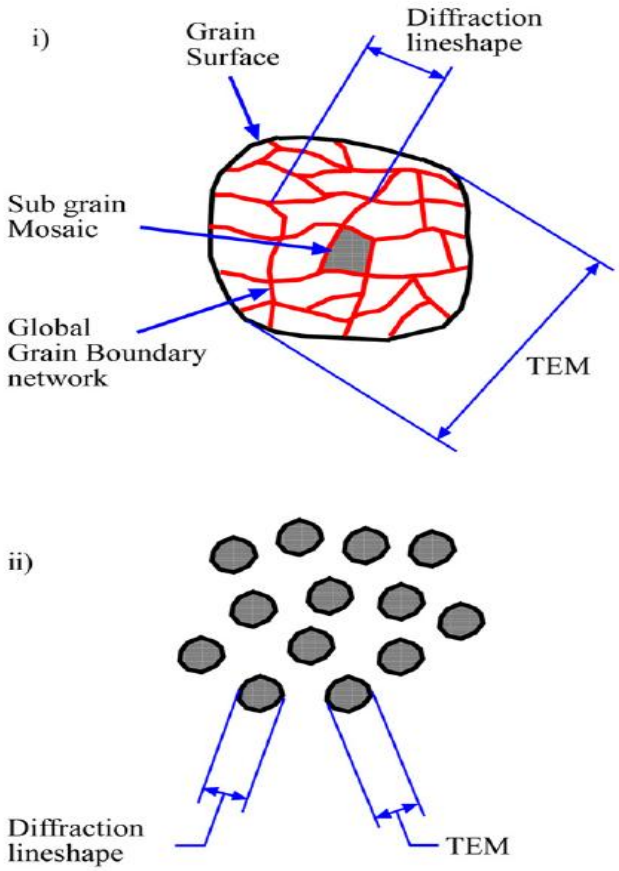

Figure 1- 9.A typical schematic of nanocrystalline material (i) and nanoparticles (ii)[49].

Nanoparticles exhibit properties that differ substantially from those of bulk materials, as a result of a small particle dimension, high surface area, quantum confinement and other effects[41]. When the particle size is reduced beyond certain range (called critical particle size), most of the atoms will be exposed to the surface (high surface-to-volume ratio)[48,50]. For isolated spherical particles, the specific surface area (SSA) is equal to $4\pi r2/(4/3\pi r3\rho)=3/r\rho$ where r is the particle radius and ρ is its density[51]. For particles that are in contact with one another, their SSA is approximately half of this value[51]. From Fig. 1-10, it shows that the surface area directly alters the proportion of atoms at or near the free surface (i.e. ~30 - 50% of the atoms in a 5 nm particle are influenced by its surface compared to a few percent for a 100 nm particle)[51]. It is at this region where the properties of the material begin to differ drastically from that of the bulk materials.

Surface atoms have lower coordination than that in bulk materials[50]. Generally they are found to occupy the less stable top and bridge sites[50]. Therefore the average number of bonds between constituents is lower for smaller clusters[50]. This could explain why the decomposition temperature, the kinetics and thermodynamics of hydrogen uptake and release can be improved by using nanoparticles instead of bulk metal hydride materials[41,50,52-54].

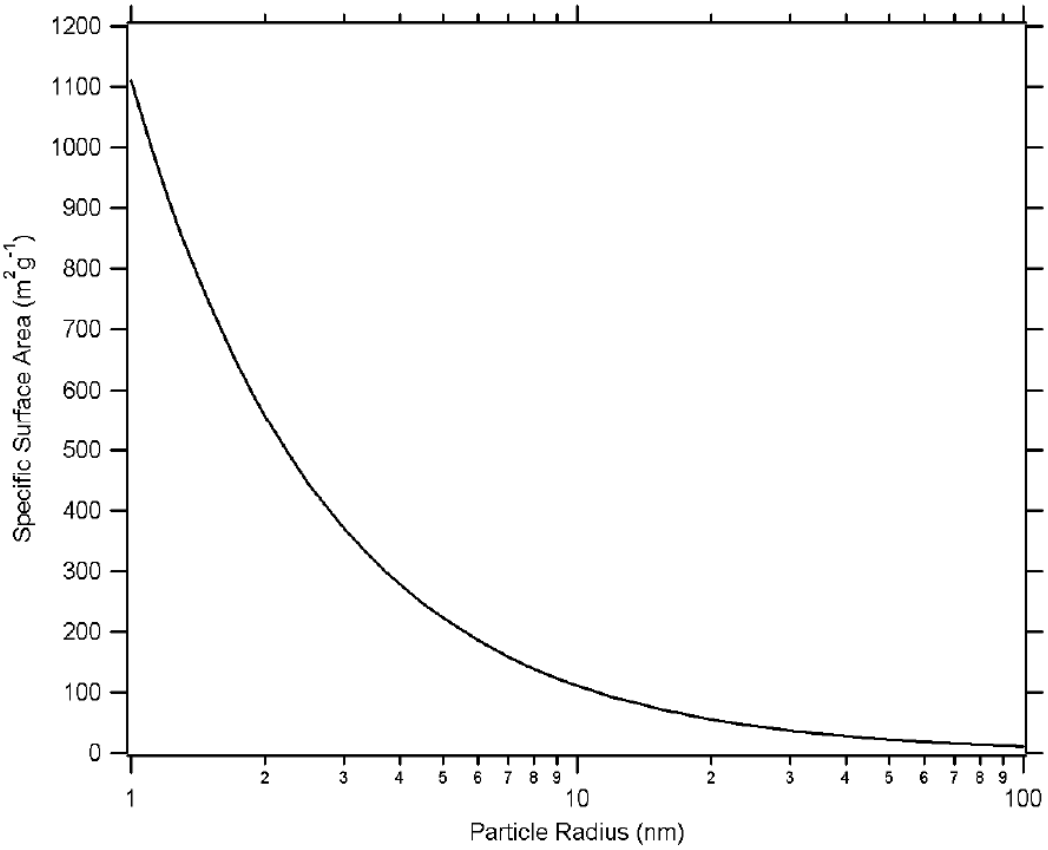

Figure 1- 10.Specified surface area values of different sized Al nanoparticles using theoretical calculation. The Al nanoparticles are assumed not in contact with one another[51].

1.5.2 Synthesis

Many techniques have been developed for the synthesis of nanoparticles including vapor, liquid and solid-state approaches[48,55,56]. The vapor approach involves physical vapor deposition, chemical vapor deposition and aerosol spraying. The liquid approaches range from sol-gel to wet chemical methods. The solid-state approach takes place by mechanical milling, mechanical alloying, mechanochemical and cryomilling. Herein the mechanochemical and cryomilling techniques are utilised for synthesising Al and AlH_3 nanoparticles.These techniques have been shown to have advantages over other methods of producing nanoparticles in terms of low cost, small particle sizes, low agglomeration, narrow size distributions and uniformity of crystal structure and morphology[55,57,58]. Mechanical alloying technique is utilized for processing intermetallic compound. This technique has been used to produce several advanced materials such as equilibrium, nonequilibrium (amorphous, quasicrystals, nanocrystalline) and composite materials[56,59].

1.5.2.1 Mechanochemical

This technique is based on the following solid state displacement reaction as shown in equation (1.6)[48]

$$\boldsymbol{A_xC + yB \rightarrow xA + B_yC} \qquad \textbf{(1. 6)}$$

where A_xC and *B* are precursors, *A* is the desired product and B_yC is a by-product of the reaction. It involves mechanical activation of this solid state displacement reaction in a ball mill. Therefore mechanical energy is used to induce chemical reactions. The precursors typically consist of mixtures of oxides, chlorides and/or metals that react either during milling or during subsequent heat treatment to form a composite

powder[48]. This composite powder consists of the dispersion of ultrafine particle within a soluble salt matrix. Usually a buffer, often the by-product of the reaction (salt matrix), is added to the starting precursors during the mechanochemical technique. Addition of buffer can control the particle size distribution, to prevent their subsequent growth and suppress their agglomeration. The ultrafine particles are then recovered by selective removal of the matrix phase through washing with an appropriate solvent[55,57,58,60].

1.5.2.2 Cryomill

This process involves milling at cryogenic temperatures (77 K) and/or milling of materials is done in cryogenic media such as liquid nitrogen[56,61]. The advantages of using cryomilling compared with milling at room temperature is that the extremely low temperature of liquid nitrogen will suppresses recovery and recrystallization and leads to finer grain structures and more rapid grain refinement[61].

1.5.2.3 Mechanical Alloying

This process involves milling mixtures of powders (of different metals or alloys) together. Material transfer is involved in this process to obtain a homogeneous alloy. Factors affecting the mechanical alloying are types of mills, types of milling tool, types of milling media, milling atmosphere, BPR, milling time and milling temperature[48,56,59].

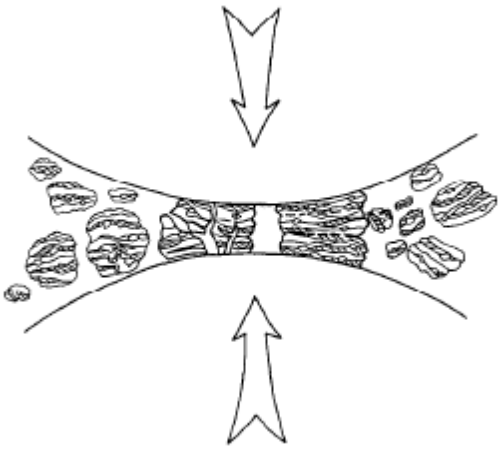

Figure 1- 11.Ball-powder-ball collision of powder mixture during mechanical alloying[59].

The main process takes place in a mill during mechanical alloying is the ball-powder-ball collision. Powder particles are trapped between the colliding balls during milling and undergo repeated welding, fracturing and rewelding processes which define the ultimate structure of the powder (Fig.1-11)[56,59,62]. In order to mechanically alloying successfully, a balance between fracturing and cold welding must be established[56,59]. However this condition is critical to achieve due to cold welding. Cold welding can be reduced by modifying the surface of the deforming particles by addition of suitable process control agent (PCA)[56,59]. This PCA will impede the clean metal to metal contact necessary for cold welding. Another approach is by modifying the deformation mode of the powder particles[59]. This will make the particles fracture before they are able to deform to the large compressive strain necessary for flattening and cold welding. This condition can be achieved by cooling the mill chamber.

1.5.2.3.1 Process Control Agent (PCA)

PCA is also referred as lubricant or surfactant. They can be solids, liquids or gases. A PCA is added to the powder mixture during milling to reduce the effect of cold welding[56,59]. The most important PCAs include stearic acid, hexane, methanol and ethanol[56]. Majority of these PCAs decompose during milling, interact with the powder and form compounds and these get incorporated in the form of inclusions and/or dispersion into the powder particles during milling[56].

CHAPTER 2: Experimental

2.1 Material synthesis

2.1.1 Glove box

Unless otherwise specified all reagents and reactions were prepared in an mBraun, argon glove box (Fig. 2-1). The glove box function is to minimise oxygen (O_2 <5 ppm) and moisture (H_2O <1 ppm) contamination of samples by monitoring the oxygen and moisture content, and constantly purifier the glove box with argon whenever the oxygen and moisture content reach an unwanted level. The glove box has a large and small antechamber which can be evacuated for putting items (chemicals, samples and apparatus) inside or outside the glove box.

Figure 2- 1.The mBraun glove box.

2.1.2 Aluminium nanoparticles

The starting reagents were Li (Sigma-Aldrich, ≥99.9%), $AlCl_3$ (Sigma-Aldrich, 99%) and LiCl (Sigma-Aldrich, 98%).

Milling was performed using a custom-made 316 stainless steel ball milling canister (Fig. 2-2a) attached to a Glen Mills Turbula T2C shaker mixer (Fig. 2-2b). The particle and grain size of the starting reagents used in mechanochemical synthesis can have a significant effect on the resulting product phase particle size[63]. Therefore the reagents were all individually pre-milled for 12 h prior to use. LiCl was used as a buffer. Then the mixture of starting reagents with different LiCl:Al volume ratios (6.786:1, 9.665:1 and 12.544:1) were milled for another 6 h using a ball to powder mass ratio of 35:1 with 316 stainless steel balls of 7.9 mm and 12.7 mm diameter (Fig. 2-2a).

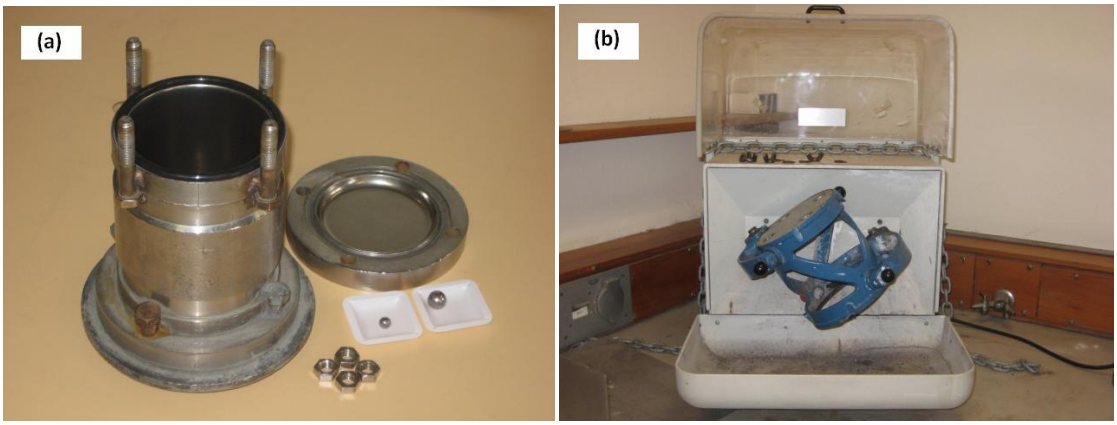

Figure 2- 2.(a) A custom made ball milling canister with 650 cm^3 internal volume and balls of 7.9 mm and 12.7 mm diameter (b) A Glen Mills Turbula T2C shaker mixer.

To remove the LiCl by-product / buffer phases, the reacted particles were washed with 30 ml of tetrahydrofuran (THF) solvent by stirring for 2 h using a magnetic stirrer (Fig. 2-3). Samples were sealed within 50 ml fluorinated ethylene propylene (FEP) centrifuge tubes (Fig. 2-4b). Following each wash, the particles were recovered from the solvent by

means of centrifugation (Fig. 2-4a). Centrifugation was undertaken until liquid / solid particle separation was complete. The liquid phase was then decanted via syringe or pipette within a glovebox. These washing steps were repeated 3 times until the solvent was completely removed. Washed particles were subsequently dried overnight under argon.

Figure 2- 3.A magnetic stirrer was used to wash the synthesised particles with THF.

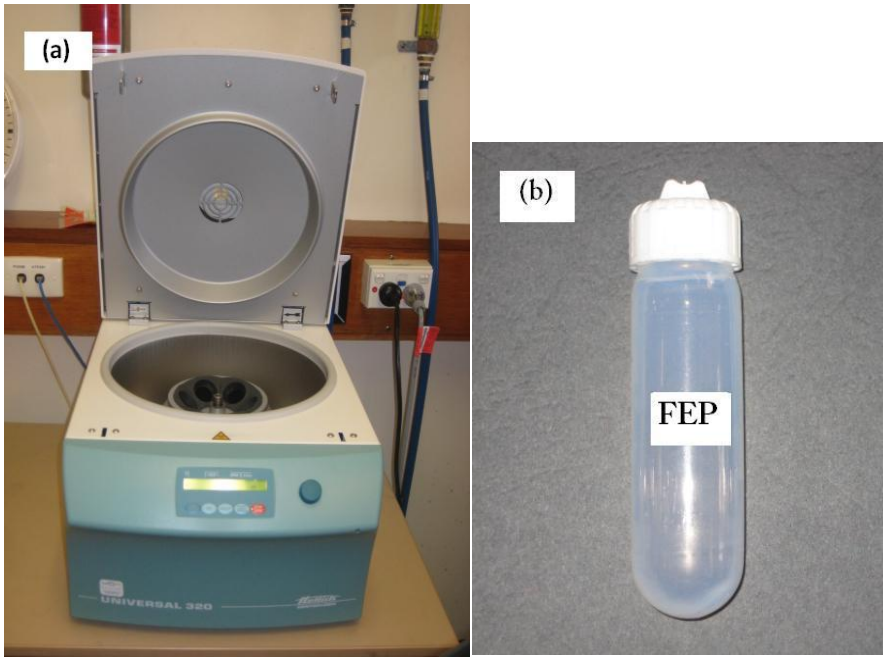

Figure 2- 4.(a) A UNIVERSAL320 centrifuge (9000 rpm) was used for centrifugal separation of solid-liquid samples (b)50 ml fluorinated ethylene propylene (FEP) centrifuge tubes .

2.1.3 Alane nanoparticles

The starting reagents were $LiAlH_4$ (Sigma-Aldrich, ≥95%), $AlCl_3$ (Sigma-Aldrich, 99%) and LiCl (Sigma-Aldrich, 98%).

Milling was performed in a SPEX 6850 cryomill using a custom-made 440c stainless steel rod milling canister (Fig. 2-5b) held within two electromagnets in a chamber that is filled with liquid nitrogen (Fig. 2-5a). Cryogenic milling is the preferred synthesis method in synthesising AlH_3 because low milling temperatures restrict AlH_3 decomposition. The small milling rod (32 g) is magnetically displaced 20 times per second with 1 g sample quantities placed within the canister between the end caps to provide a milling action at 77 K. LiCl was used as a buffer. The mixture of starting reagents with different LiCl: AlH_3 volume ratios (0.76:1, 2:1, 5:1 and 10:1) were milled for 30 minutes using a rod to

powder mass ratio of 32:1 respectively. The sample was milled in a stepwise fashion (milled for 2 – 5minutes and stopped for ~30 minutes incrementally) in an attempt to restrict the amount of heat build-up during milling.

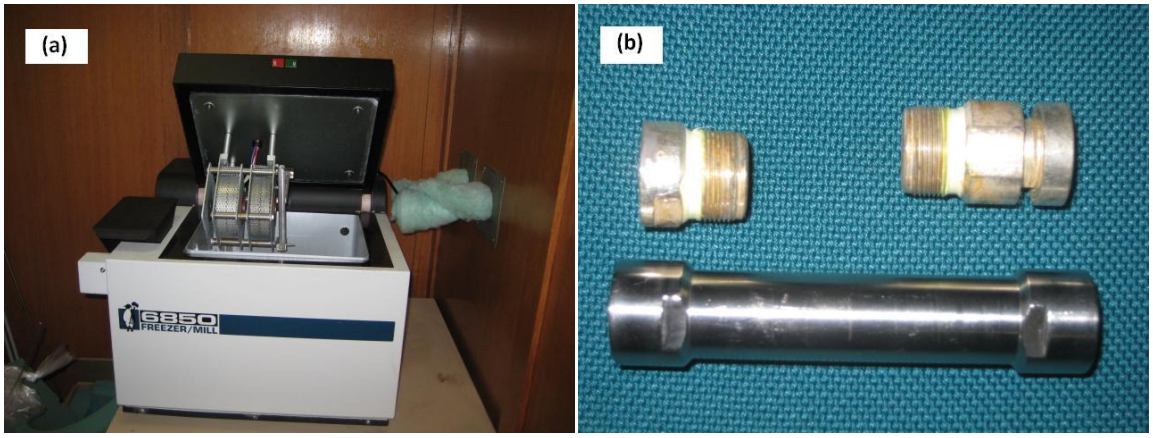

Figure 2- 5.(a) The SPEX6850 Freezer mill equipment and a (b) custom-made rod milling canister with 14.3 cm^3 internal volume.

2.1.4 Titanium manganese (TiMn) alloy

2.1.4.1 Commercial sample

The $Ti_{0.97}Zr_{0.019}V_{0.439}Fe_{0.097}Cr_{0.045}Al_{0.026}Mn_{1.5}$ alloy was investigated as-supplied without further alteration from Sigma-Aldrich Australia.

2.1.4.2 Synthesised samples

2.1.4.2.1 Mechanical Alloying Technique

The starting materials were Ti (Aldrich, 99.7%, -100 mesh), Zr (Aldrich, 99.7%, -100 mesh), Mn (Aldrich, 99.99%) and Cr (Aldrich, 99+%, -325 mesh).

Five alloys of nominal composition $TiMn_2$, $TiMn_{1.5}$, $Ti_{0.97}Zr_{0.019}Mn_{1.5}Cr_{0.57}$ and $Ti_{0.7875}Zr_{0.2625}Mn_{0.8}Cr_{1.2}$ were prepared by mechanical alloying the starting materials with toluene in a custom made ball milling canister (650 cm^3 internal volume) attached to a Glen Mills Turbula T2C shaker-mixer. Toluene was used as a process control agent. Milling was performed under a high purity argon atmosphere using a ball-to-powder (mass) ratio of 12:1 with balls of 7.9 mm and 12.7 mm diameter and milling time of 40 h. The as milled samples were removed from the canister in a glove box under argon. The samples were put into the 316 stainless steel sample cell and annealed at 800°C under vacuum for 3h. Reactive powders like Ti and its alloy powders react rapidly with oxygen, nitrogen and hydrogen[56,64]. The levels of oxygen and water vapour must be kept very low for an optimum result[64]. This can be achieved either by annealing under 100 % argon or vacuum[64,65]. DSC and DTA measurements showed that the crystallization temperature of the as-milled TiMn samples were around 700 – 900°C[65,66]. Heating to these crystallization temperatures led to the formation of the crystalline phase TiMn alloy.

2.2 Characterization

2.2.1 X-ray diffraction (XRD)

The chemical evolution of the reactant mixtures during processing (Al and AlH_3) and the lattice parameter before and after hydrogenation (TiMn alloys) were conducted using the X-Ray Diffraction (XRD) technique. This technique was performed using a BrukerD8 Advance diffractometer (Cu K_α radiation) with a 2θ range of 20° - 100° using 0.02° steps with operating conditions of 40 kV and 40 mA (Fig. 2-6a). The instrument configuration is given in Table 2-1. The sample was loaded into an XRD sample holder in an argon glovebox and sealed with a poly (methyl-methacrylate) (PMMA) airtight bubble to prevent oxygen/moisture contamination during data collection (Fig. 2-6b). The

crystallite sizes were determined from an LVol-IB method that provides a good measure of the volume-weighted average crystallite size[67]. The structural parameters were refined from the diffraction data using Rietveld refinement in TOPAS (Bruker AXS, Karlsruhe, Germany) via a fundamental parameters approach.

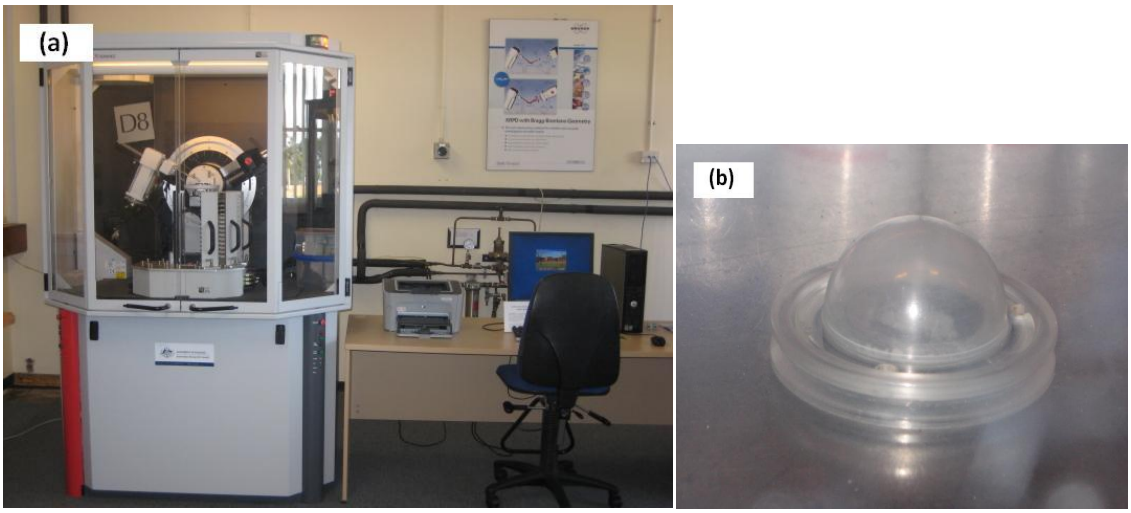

Figure 2- 6.(a) The Bruker D8 Advance diffractometer at Curtin University and (b) a poly (methyl-methacrylate) (PMMA) airtight bubble.

Table 2- 1:X-Ray Diffraction (XRD) instrumental parameters.

Parameter	D8
Radiation (wavelength)	Cu (1.5418 Å)
Operating voltage	40 kV
Operating current	40 mA
Detector	Linear PSD (3º 2ϑ)
Monochromator	(Ni filter)
Lorentz-Polarisation factor	0
Goniometer radii	250 mm
Source length	12 mm
Sample length	25 mm
Receiving slit length	17 mm
Receiving slit width	-
Fixed divergence slit angle	0.3°
Primary Soller slit angle	2.5°
Secondary Soller slit angle	2.5°

2.2.2 Scanning Electron Microscope (SEM)

Microstructural observations of as-received and hydrogen cycled alloys were conducted on a Philips XL-30 Scanning Electron Microscopy (SEM) at Curtin University using a secondary electron detector whilst operating at 15 keV (Fig. 2-7a). The microscope was coupled with an Oxford Instruments energy dispersive X-Ray spectrometer (EDS) for elemental analysis. Samples were briefly (<1 - 2 min) exposed to air and were not coated prior to imaging in the SEM. Samples were prepared by sprinkling the particles onto carbon tape fixed to a SEM sample holder (Fig. 2-7b and c).

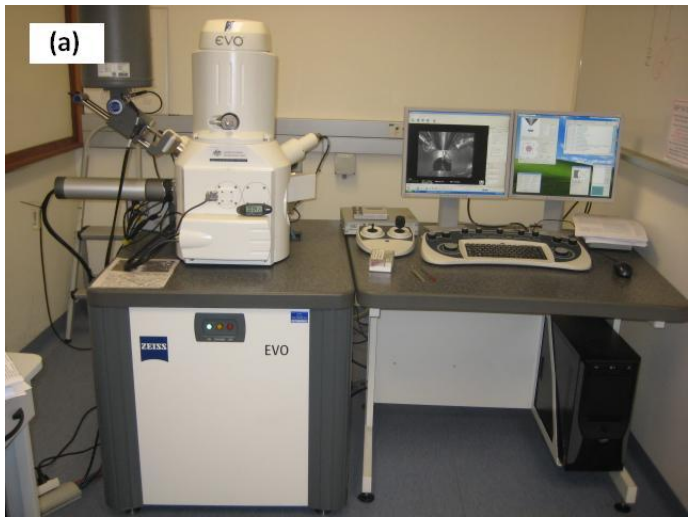

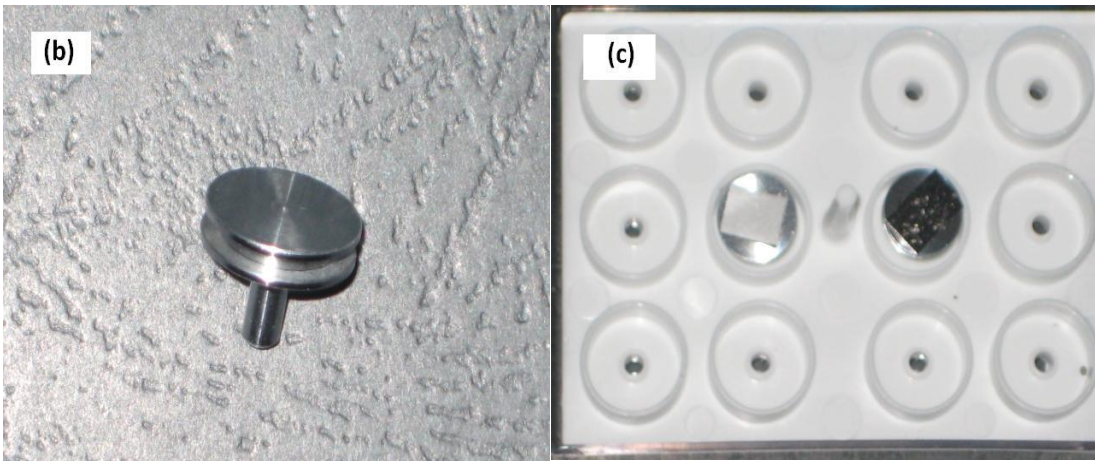

Figure 2- 7.(a) The Philip XL-30 scanning electron microscopy at Curtin University (b) SEM sample holder (c) Carbon tape was placed on the top of the SEM sample holder before the sample particles were sprinkled on it.

2.2.3 Energy Dispersive X-ray Spectrometer (EDS)

EDS provides elemental analysis of selected sample regions during transmission electron microscopy (TEM) investigations. The interaction between charged electrons and different elemental constituents of the sample cause characteristic x-rays to be emitted, which can be detected by a detector with a range of energy channels. Each element

emits x-rays with different energies allowing elemental determination. The electron beam can be directed toward specific parts of a sample during imaging allowing EDS to be performed on minor sample features of interest.

2.2.4 Transmission Electron Microscopy (TEM)

The particle morphology and high resolution transmission electron microscopy (HRTEM) for lattice imaging of individual unwashed and washed samples was examined by using a JEOL 3000F FEGTEM instrument operating at 300 kV at the University of Western Australia and JEOL JEM2011 instrument operating at 200 kV at Curtin University (Fig. 2-8). The microscope was coupled with an Oxford Instruments energy dispersive X-Ray Spectrometer (EDS) for elemental analysis.

Figure 2- 8.The JEOL JEM2011 instrument at Curtin University.

Samples were prepared by ultrasonically dispersing the unwashed and washed particles in toluene (Fig. 2-9a) and then evaporating a drop of the dispersion onto 200 mesh copper grids with holey carbon support films (Fig. 2-9b). Samples were briefly (<1 - 2 min) exposed to air prior to imaging in the TEM.

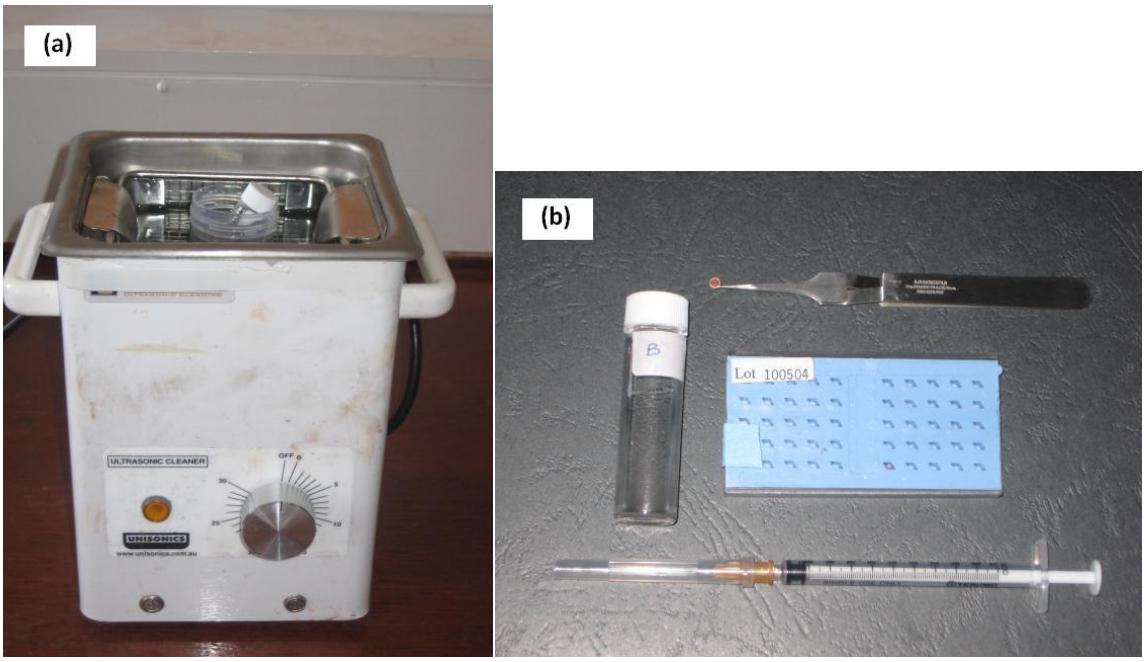

Figure 2- 9.(a) An ultrasonic bath equipment and (b) TEM sample preparation apparatus.

2.2.5 Small X-ray Scattering (SAXS)

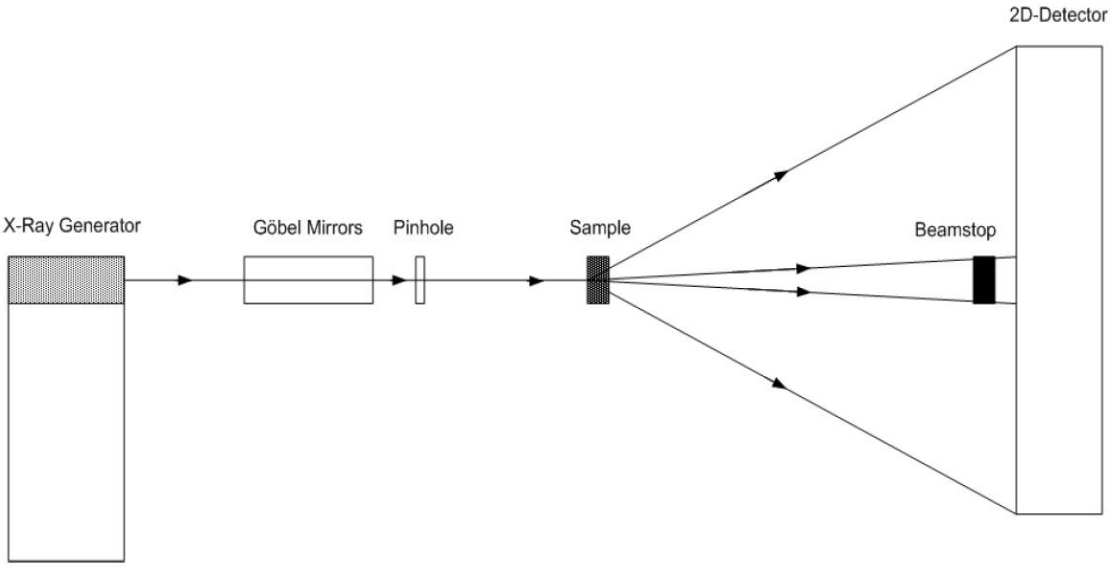

Figure 2- 10.SAXS optics. Graphic courtesy of Mark Paskevicius [39].

In Fig. 2-10, x-rays are generated, collimated by the Göbel mirrors and a pinhole and then encounter the sample. When the x-rays encounter the sample, they are scattered and are projected upon a 2-dimensional detector whilst the primary beam is halted by a beamstop. The scattered x-rays are due to interaction between the incident x-ray wave and the electrons within the sample. An oscillating electric moment was produced in the atom which produced scattered field. The scattered intensity is measured as a function of the scattering angle. For analysis purpose, the scattered intensity is measured as a function of the scattering vector according to equation

$$\boldsymbol{q = \frac{4\pi \sin 2\theta}{\lambda}} \qquad \textbf{(2. 1)}$$

where θ is the scattering angle and λ is the wavelength (CuK_{α}=1.5418 Å).

The average particle size was recorded with a Bruker Nanostar SAXS instrument at Curtin University (Fig. 2-11). Samples were loaded within glass capillaries (1.0 mm diameter) and sealed temporarily with plasticine in an argon glovebox. Then the

capillaries were sealed permanently with a flame outside the glovebox to prevent contamination during data collection. Data were recorded at a detector distance of 23.2 cm using a wavelength, λ, of 1.5418 Å (Cu K_α) with a 2D multiwire detector for 3 h per sample. These data were converted to absolute intensity, $I_{abs}(q)$(details can be found elsewhere [39]).

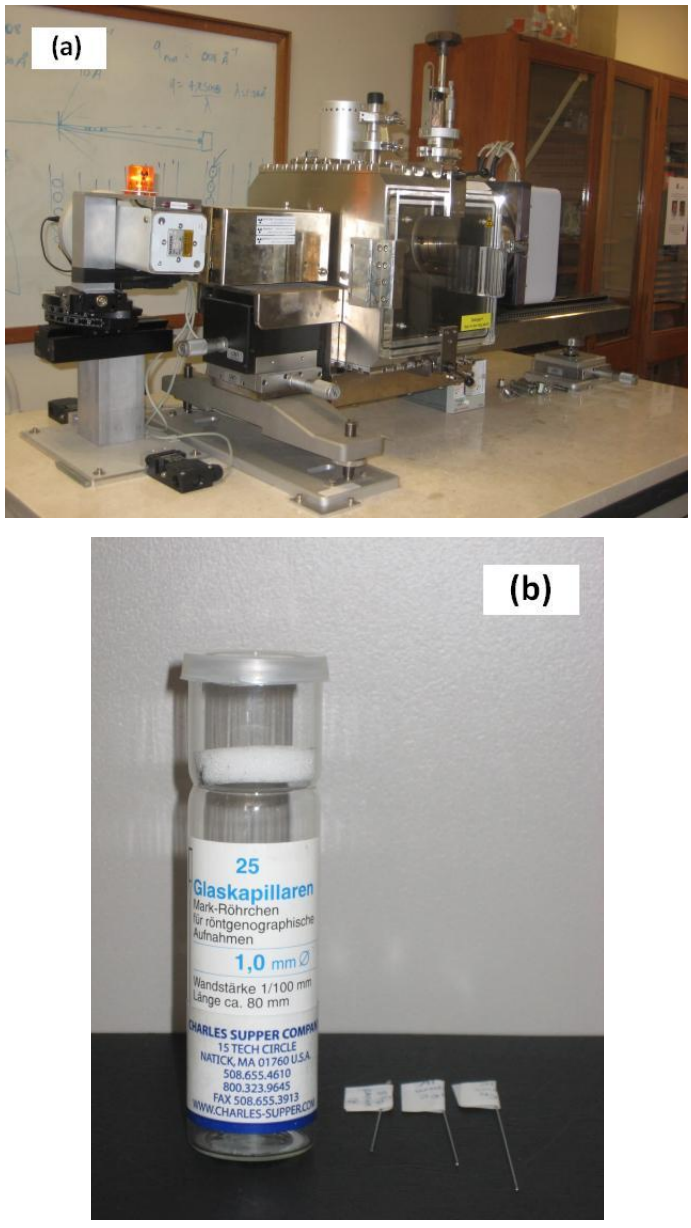

Figure 2- 11.(a) The Bruker Nanostar SAXS instrument at Curtin University and (b) capillary glasses with 1.0 mm diameter.

When the data has been converted to absolute intensity scale, a unified Guinier/power-law approach (details can be found elsewhere[68-70]) was used to model the converted data by using the Irena package[71] for IGOR Pro (Wavemetrics, Oregon).

The Irena package provides a fitting package that enables the user to obtain the relevant parameters from the unified model. The small angle scattering data set must be converted to an absolute scale first in order to obtain accurate values for the power-law prefactor constant *B* and the Guinier exponential prefactor *G*. Irena also provides a global normalised mathematical fitting uncertainty and mathematical fitting uncertainties for each of the refined variables in the unified model. Then from this unified model, the relevant parameter such as the average particle size, specific surface area or volume fractions can be identified[72] and the physical properties of the sample interest(aggregate, primary particle and atomic structure) can be interpreted.

2.3 Hydrogen Measurement Equipment

2.3.1 Types of equipment

There are 3 types of hydrogen sorption equipment to measure the quantity of absorbed and desorbed hydrogen from a sample[73,74]. The gravimetric apparatus (thermogravimetrics), where the sample weight loss is measured; the volumetric apparatus (sieverts / manometric), where the hydrogen pressure changes due to hydrogen sorption in the reaction chamber of known volume is measured and the volumetric apparatus (flow-controlled), where the quantity of gas by integrating gas flow over the time period required to fill the sample cell is measured.

In this study, hydrogen sorption measurement were undertaken using custom made volumetric apparatus (Sieverts) as shown in Fig. 2-12 (manual rig), Fig. 2-13 (automatic rig), Fig. 2-14 (supercritical carbon dioxide rig ($ScCO_2$) and Fig. 2-15 (high pressure rig).

2.3.1.1 Manual Rig

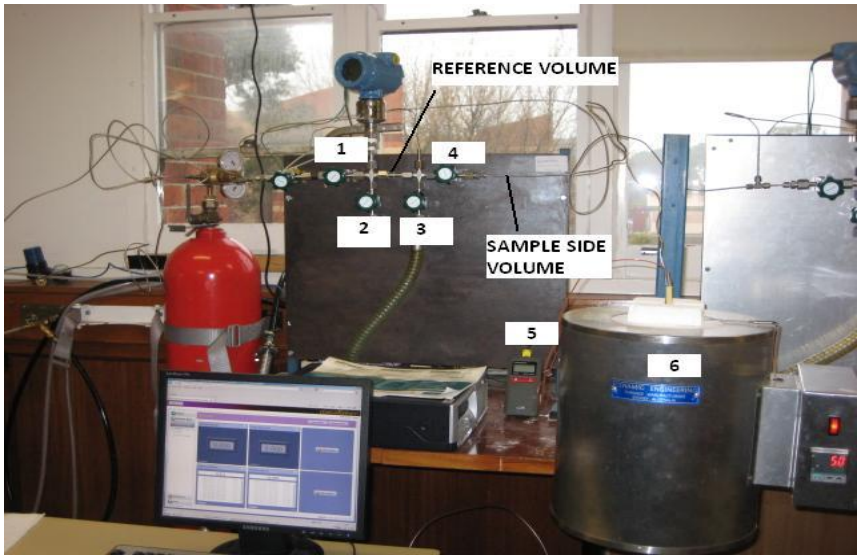

Figure 2- 12.A custom made manual rig at Curtin University. It consist of (1) valve 1, (2) valve 2, (3) valve 3, (4) valve 4, (5) thermocouple and (6) tube furnace.

A manual sieverts apparatus[75] was utilised with 316 stainless steel components (Swagelok, Australia) and only the calibration volume component that is built from 304 L stainless steel. It has 2 distinct volumes (reference volume and sample side volume) and the diaphragm valves operate manually. This apparatus was rated up to hydrogen pressures of 24 MPa.

The pressure is measured using a pressure gauge (Rosemount, model 3051S, Emerson Process Management, Australia) with a precision and accuracy of 14 mbar. This pressure gauge operates using 'gauge pressure' that is relative to atmospheric pressure. Therefore an atmospheric pressure reading is also recorded using a barometer (Baromec M1975, Mechanism Ltd., England).

The temperature is measured using a thermocouple (K-type, Hinco Instruments, Australia). It penetrates deep within the reference volume in order to determine the ambient temperature. For higher temperatures application, a Labec tube furnace were

used (Laboratory Equipment P/L, Australia) where the temperature was calibrated using a K-type thermocouple at a set sample depth. For cryogenic temperature (77 K), the sample cell was put into a flask filled with liquid nitrogen during the measurement.

For the hydrogen absorption measurement, this apparatus operates by inputting hydrogen gas into a known reference volume (V_r) to the desired pressure at a given temperature (Valve 1 is slowly opened and then closed). The pressure and temperature are recorded as initial reference side pressure (P_r) and initial reference side temperature (T_r). Then the hydrogen gas is allowed to enter the known sample side volume (V_s), which also contains the sample of interest (V_{sample}) (Valve 4 is slowly opened). Once equilibrium has been reached between the hydrogen gas and the sample, the pressure and temperature are recorded again (Valve 4 is slowly closed). This time the pressure and temperature are recorded as final equilibrium pressure (P_e) and final equilibrium temperature (T_e). These steps are then repeated until no absorption takes place and the sample has reached its maximum hydrogen content for a given pressure and temperature. The values of P_e and T_e become the initial sample side pressure (P_s) and initial sample side temperature (T_s) respectively.

For hydrogen desorption measurements, this apparatus operates by evacuating the system for 30 minutes (Valve 3 and 4 are slowly opened). Then the initial reference side pressure (P_r) and initial reference side temperature (T_r) are recorded (Valve 3 and 4 are slowly closed). At this time the P_r is recorded as zero. Valve 4 is then opened and once the equilibrium has been reached between the sample and the hydrogen gas, Valve 4 is slowly closed. The pressure and temperature are recorded again. This time the pressure and temperature are recorded as final equilibrium pressure (P_e) and final equilibrium temperature (T_e). These steps are then repeated until no desorption takes place and the sample has released its maximum hydrogen content. The values of P_e and T_e become the initial sample side pressure (P_s) and initial sample side temperature (T_s) respectively.

The details of hydrogen sorption calculations can be found in section 2.3.2 of this chapter. For the hydrogen desorption measurements of AlH_3, analysis on any residual gas was not undertaken. This is due to the fact that AlH_3 contains 10.1 wt.% hydrogen and this value is consistence with the result obtained for the desorption measurement of AlH_3.

2.3.1.2 Automatic Rig

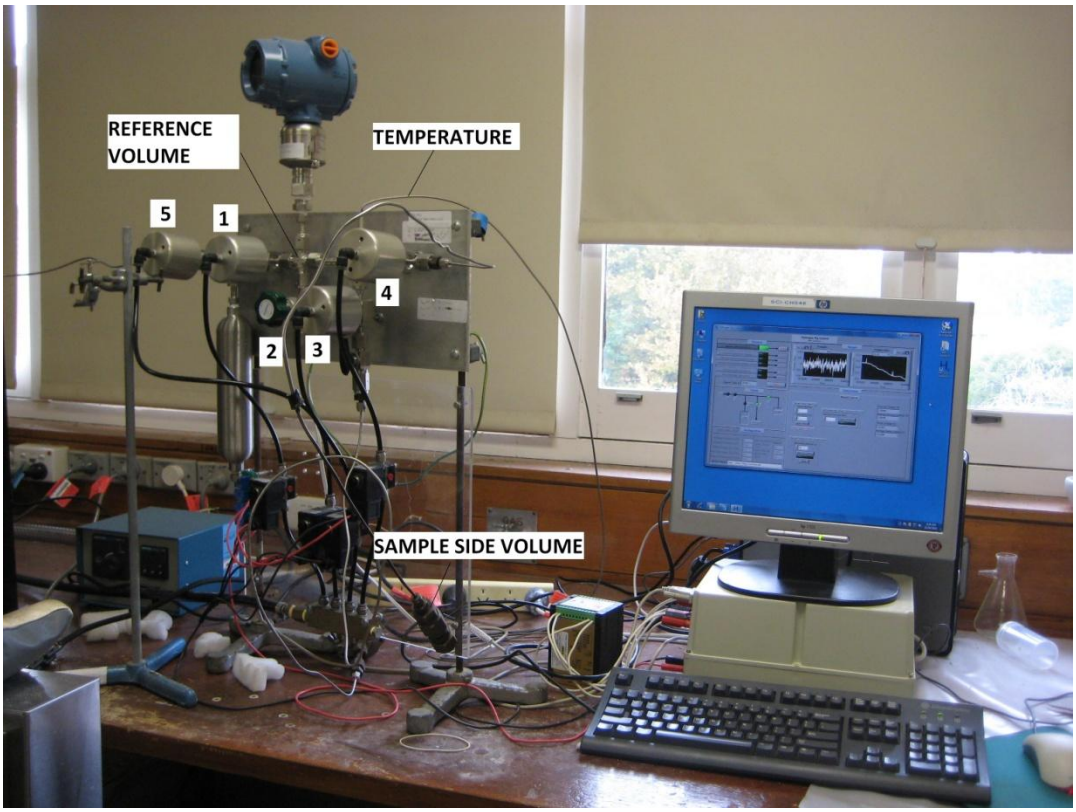

Figure 2- 13.A custom made automatic rig at Curtin University. It consist of (1) valve 1, (2) valve 2, (3) valve 3, (4) valve 4 and (5) valve 5.

An automated Sieverts apparatus[39] was utilised, with computer controlled pneumatic valves and computer inputs for pressure and temperature as shown in Fig. 2-13.

The temperature measurements were recorded using a 4-wire platinum resistance temperature device (RTD).

The pressure was recorded using a digital pressure gauge (Rosemount 3051S calibrated up to 150 bar with a precision and accuracy of 14 mbar).

2.3.1.3 $ScCO_2$ Rig

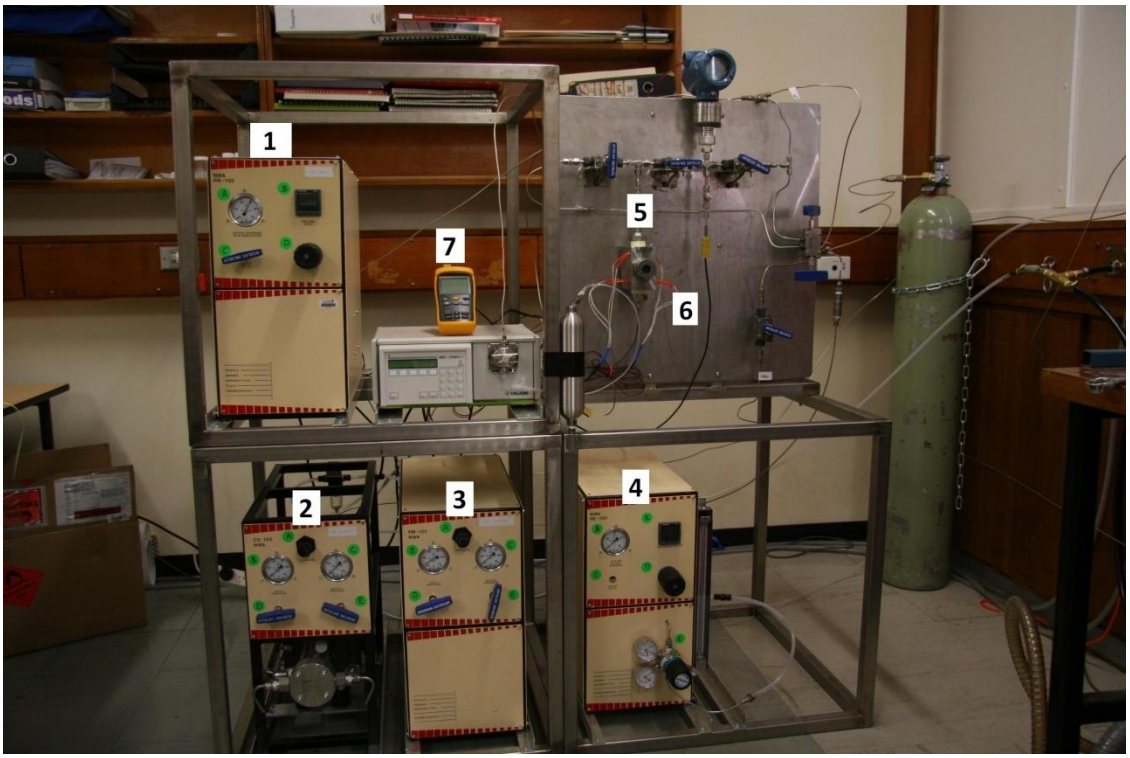

Figure 2- 14.A custom-made supercritical carbon dioxide ($ScCO_2$) rig at Curtin University. It consist of (1) CO_2 delivery, (2) H_2 compressor, (3) CO_2 condenser, (4) expander (5) high pressure reaction vessel, (6) thermostat and (7) thermocouple.

A $ScCO_2$ Sieverts apparatus was utilised using the same principles and components as a manual apparatus, but with a 50 ml stainless steel high pressure reaction vessel, CO_2 pump (CO_2 condenser and CO_2 delivery), H_2 compressor, expander, thermostat and the

apparatus was rated up to hydrogen pressures of 660 bar. Liquid CO_2 and H_2 gas were admitted to high pressure reaction vessel and the reaction mixture in this vessel was then heated to 40 - 50°C, thereby forcing the CO_2/H_2 mixture into supercritical phase.

2.3.1.4 High pressure Rig

Figure 2- 15.A custom made high-pressure rig at Curtin University. It consists of (1) H_2 compressor, (2) expander, (3) sample chamber and (4) thermocouple.

A high pressure Sieverts apparatus was utilised having the same principles and components as a manual apparatus, but with stainless steel high pressure reaction vessel, H_2 compressor, expander and the apparatus was rated up to hydrogen pressures of 4 kbar. For hydrogen desorption measurements, the pressure was recorded using a digital pressure gauge (Rosemount 3051S). For hydrogen absorption measurements, the pressure was recorded using a pressure indicator (WIKA PH6400 calibrated up to 4 kbar with an accuracy of 0.1% full scale) or a digital pressure gauge (Rosemount 3051S). In

the case where Rosemount 3051S was used, the sample chamber must be held in a flask that is filled with liquid nitrogen during pressure and temperature measurement to avoid any damage to the digital pressure gauge and the actual pressure was calculated using an iterative solving technique (details can be found in Appendix C). The hydrogen absorption measurements were also repeated where a pressure indicator (Presens Precise calibrated up to 2 kbar with an accuracy of 0.02% full scale) was used to record the pressure.

According to the ideal gas law ($PV = nRT$), if the temperature changes and the number of gas molecules are kept constant, then either pressure or volume (or both) will change in direct proportion to the temperature[76]. In this case when the sample chamber is held in liquid nitrogen, the samples underwent pressures of 280 bar at -196°C. When the sample chamber is held out of liquid nitrogen, the pressure increased from 280 to 1420 bar at 25°C. When the sample chamber was heated at 50°C, 100°C and 150°C, the pressure increased to 1532, 1734, 1967 bar respectively.

The temperature measurements were recorded using a k-type thermocouple in both cases.

2.3.2 Hydrogen sorption calculations

An outline of the steps involved in calculating n_{ADS}, the total number of moles absorbed by the sample at ambient and non-ambient temperature can be found in Appendix D[75].

2.3.3 Hydrogen sorption procedure

2.3.3.1 Aluminium nanoparticles

Unwashed and washed Al nanoparticles were loaded in a 50 ml stainless steel high pressure reaction vessel under an argon gas atmosphere (Fig. 2-14). Before any measurements were undertaken, the reference volume and reaction vessel were completely evacuated for 30 minutes at 25°C. Liquid CO_2 (150 - 200 bar) was admitted to this vessel from a CO_2 cylinder with the aid of a CO_2 pump (CO_2 condenser and CO_2 delivery). H_2 (150 - 250 bar) was added from the H_2 cylinder to this vessel with the aid of a H_2 compressor. The reaction mixture in this vessel was then heated to 40 - 50°C, thereby forcing the CO_2/H_2 mixture into supercritical phase for 1 week. The CO_2 becomes supercritical at 73.8 bar and 31.1°C. At this point, the vessel was cooled to room temperature and all volatile material was removed by venting and pumping for 1 h. The reaction vessel was then disconnected from the other components and transported into an inert atmosphere glove box. The hydrogen desorption properties of the samples were determined using a custom-built automated Sieverts apparatus (Fig. 2-13). Before any measurements were undertaken, the reference volume and sample chamber were evacuated for 1 h at 25°C. Once this process was complete, the desorption measurements of pressure and temperature were recorded over the next 48 hours. The samples were heating at 100°C to test for hydrogen release.

2.3.3.2 Alane nanoparticles

The hydrogen desorption properties of the samples were determined using a custom-built manual Sieverts apparatus (Fig.2-12). Before any measurements were undertaken, the reference volume and sample chamber were completely evacuated for 30 minutes at 25°C. Then the samples were left at room temperature for 24 hours, followed by the sample chamber heated to 50°C, 100°C and 150°C and held at each temperature for 24

hours respectively in order to study the kinetic property and maximum desorbed H_2 wt.% of the samples.

Hydrogen absorption measurements were performed in a high pressure Sieverts apparatus (Fig. 2-15).Non-ambient sample temperatures were generated using a sealed tube furnace. Before any measurements were taken, the synthesised samples were fully desorbed by heating at 150°C under vacuum for 24 h. Then the samples underwent pressures of 280 bar at -196°C, followed by the sample chamber underwent pressure of 1420 bar at 25°C, 1532 bar at 50°C, 1734 bar at 100°C and 1967 bar at 150°C and held at each pressure for 24 hours respectively. In this case the actual pressure was calculated using an iterative solving technique (details can be found in Appendix C section of this chapter).

2.3.3.3 Titanium manganese

The hydrogen sorption properties of the alloy were determined using a custom-built automated Sieverts apparatus (Fig.2-13). Before any measurements were undertaken the sample was first evacuated for 1 h at 25°C to remove any adsorbed gas. Activation of the alloy was then undertaken by first introducing 50 bar of hydrogen into the sample chamber at room temperature for 1 h, followed by an evacuation step. This hydrogen absorption/desorption activation cycle was undertaken 3 times. After completion of the activation process, the residual hydrogen within the sample was removed via evacuation at room temperature for 24 h. The pressure-composition isotherm (PCI) measurements were subsequently performed at 25°C, 40°C and 60°C while being careful to verify that the sample was at pressure equilibrium at each collected data point.

CHAPTER 3: Aluminium nanoparticles

3.1 Introduction

Aluminium is cheap, safe, plentiful and is widely used in 21st Century technologies. It is the third most abundant element (after oxygen and silicon) and the most abundant metal in the earth's crust as shown in Figure 3-1[77]. It makes up about 8% by weight of the earth's solid surface[78,79].

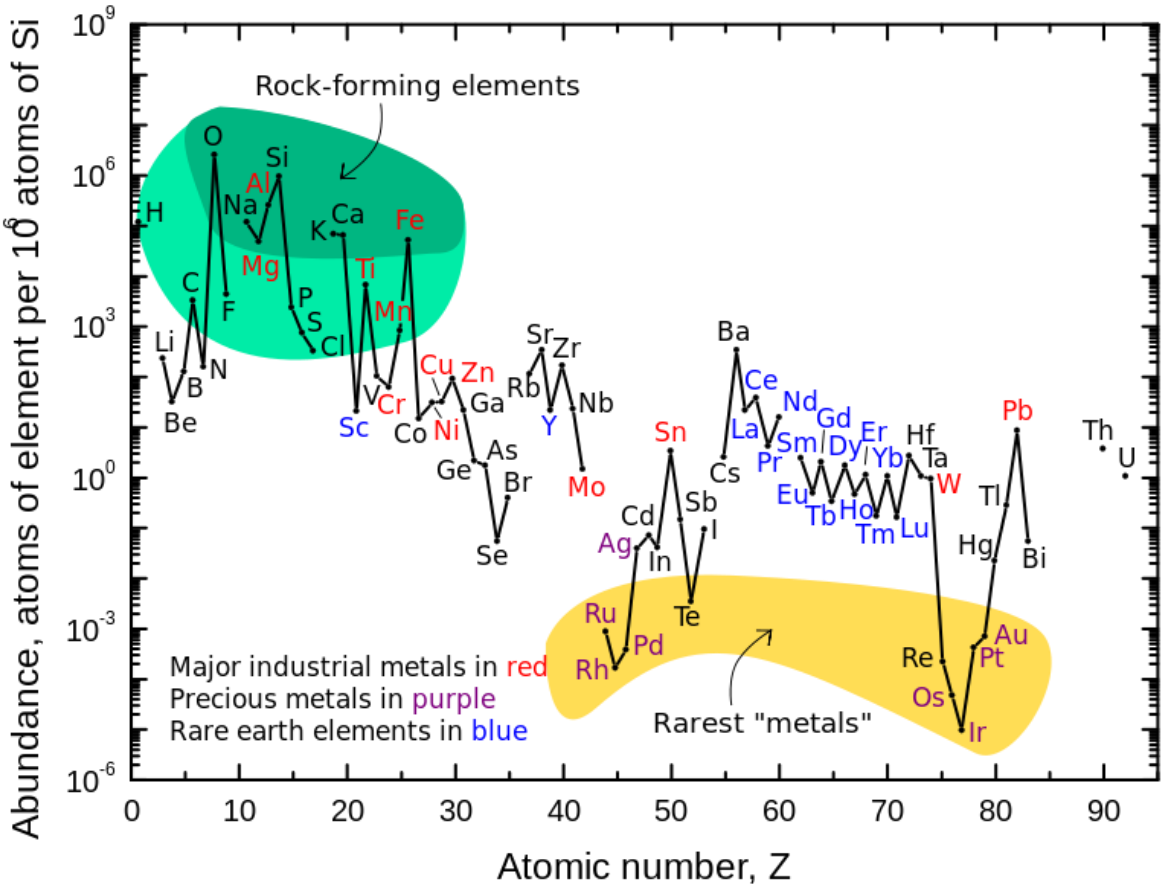

Figure 3- 1.The abundance (atom fraction) of the chemical elements in earth's crust as a function of atomic number[77].

Global production of aluminium was 31.9 million tonnes in 2005[80]. It increased to 42 - 45 million tonnes in 2012, driven by Chinese output[80,81]. Al is theoretically 100% recyclable without any loss of its natural qualities. Recycled Al is known as secondary Al but maintains the same physical properties as primary Al. At the London Metal Exchange, Al prices closed at $3,036.5/tonne or $3.04/kg (28th March 2012)[82].

3.1.1 Applications

Al has found many applications in a wide range of household, transportation, packaging, construction and aerospace industries[77,83,84]. Micrometer-sized Al particles are used in paint[85] and pyrotechnics (thermite reactions and solid rockets fuels)[86,87]. Recent research has focused on the application of Al nanoparticles in the medical[88], and biochemical[89] fields and to increase combustion efficiency of thermites and decrease the ignition time of propellant materials[87,90].

From an energy storage point of view, Al is a very attractive candidate for a development of high-capacity hydrogen storage material through its reaction with hydrogen[91,92] to form AlH_3[93,94]. The major drawback is the extremely high pressure and temperature (28 kbar at 300°C) required for the absorption of gaseous H_2 into bulk Al to produce AlH_3[95]. Since the temperatures and pressures required for the hydrogenation of bulk Al to produce AlH_3 are much too high to be of practical use, it has been suggested that AlH_3 might be made at lower temperatures and pressures using nanoparticulate Al [54,96] and by using supercritical carbon dioxide fluids ($scCO_2$)[97,98].

Theoretical calculations have shown that Al surfaces do not dissociate molecular hydrogen under normal conditions[99] because Al has a low affinity for hydrogen due to a relatively large activation barrier[100].Theoretical calculations for small Al clusters[101] have

been compared to experimental results for the bulk[102] in order to study the relationship between particle size and enthalpy for the Al-AlH_3 system. Pressures greater than 2 kbar are required to introduce hydrogen into pure Al nanoparticles greater than 10 nm in size at temperature ranging from 77 to 473 K (-196 to 199°C)[91]. Reactive Al compounds that were nanosized and supported on surface-oxidized carbon nanofibers (CNF) or confined in ordered mesoporous silica (OMS) exhibit lower dehydrogenation temperature and faster kinetics than those of their bulk materials[103,104]. Much effort has been devoted to the synthesis of Al/AlH_3 nanoparticles that can be stabilized by coatings or organic surface passivation agents for trapping Al particles to keep them nanoscale during the AlH_3 decomposition and protecting the Al nanoparticles postproduction from surface oxidation[105,106].

Other studies used a mixture of supercritical CO_2 and H_2 with Al metal, resulting in partial hydrogenation, giving around 0.3 wt.% H_2[97,98]. Supercritical sc$CO_2$was used as a solvent to effect the hydrogenation of Al, thereby forming AlH_3. The thermodynamic properties of AlH_3 vitiate conventional gas-solid synthesis: AlH_3 is thermochemically on the cusp with respect to decomposition to Al and H_2 (α, β and γ phases of AlH_3 have ΔH_{dehyd} values of ca.+6, -4 and +l kJ mol^{-l}, respectively[98]. Thus, even at very high pressures of H_2, the modest thermal input needed to overcome the activation barrier will place the system thermodynamically in favour of the elements (i.e. to the left of Equation 3.1)[98].

$$\mathbf{Al + 1.5H_2 \leftrightarrow AlH_3} \qquad \mathbf{(3.\ 1)}$$

Supercritical scCO_2 has unique properties to overcome this antagonistic interplay between the kinetic and thermodynamic properties of the system[107-109]. The total miscibility of H_2 with scCO_2 is a distinct advantage in this respect, allowing effective concentrations of hydrogen equivalent to hundreds of bar to be attained easily and efficiently[107-109], and favouring the thermodynamics of AlH_3 over the elements. In other

words, hydrogenation of Al to formed AlH_3 may be able to be accomplished at lower H_2 pressures using $scCO_2$ fluid. The details can be found in section 3.2.2.3 of this thesis.

3.1.2 Synthesis

The popular and simple process for preparation of rather large Al nanoparticles has previously been achieved by chemical methods[105]. Method A consists of the following[105]: reaction of $LiAlH_4$ and $AlCl_3$ at 164°C in 1,3,5-trimethylbenzene produces nano-Al with an average mean coherence length (crystallite size) of 160 ± 50 nm. The by-product LiCl is removed by washing with MeOH at -25 or 0°C. Method B consists of the following[105]: nano-Al is produced by decomposition of $H_3Al(NMe_2Et)$ under reflux in 1,3, 5-trimethylbenzene (ca. 100 - 164°C), with or without added decomposition catalyst $Ti(O\text{-}i\text{-}Pr)_4$. Here the mean particle size (40 - 180 nm) and degree of aggregation of the nano-Al depended on the mole percentage of decomposition catalyst used (0 - 1%). Later, this chemical method was modified by using ethylene glycol (EG) as a solvent instead of 1,2,3-trimethyl benzene, which produced Al with a 50 nm particle size[110].

Other researchers have also produced Al nanoparticles by using pulsed laser ablation of Al targets in ethanol, acetone and ethylene glycol[111,112]. Comparison between ethanol and acetone clarified that acetone medium leads to finer nanoparticles (mean diameter of 30 nm) with narrower size distribution (from 10 to 100 nm)[111,112]. However, thin carbon layer coats some of them, which was not observed in the ethanol medium.

Reactive Al compounds ($NaAlH_4$) have been nanosized and supported on surface-oxidized carbon nanofibers (CNF) or confined in ordered mesoporous silica (OMS) by using impregnation and drying techniques[103,113].The OMS consists of mesopores with a diameter of around 10 nm and the CNF diameter is 5 – 20 nm[103,113].

A mechanochemical method has also been used to synthesise Al nanoparticles[91]. The synthesized nanoparticles were found to be ~25 - 100 nm from TEM and average size of 55 nm was determined from SAXS measurements[91]. The mechanochemical technique involves mechanical activation of solid-state reactions caused by collisions between particles and balls inside a mill. It is a simple, economical and environmentally friendly technique. A buffer, often the by-product of the reaction, was added to the starting reagents during the mechanochemical reaction in order to control the particle size distribution, to prevent their subsequent growth and suppress their agglomeration. Removal of the buffer was usually carried out through a solvent dissolution technique followed by solid-liquid separation (washing)[57,114-117].

3.2 Supercritical carbon dioxide ($scCO_2$)

3.2.1 Supercritical fluid

A supercritical fluid is any substance at a temperature and pressure above its critical point (T_c-critical temperature and P_c-critical pressure), where distinct liquid and gas phases do not exist[118-120]. It can effuse through solids like a gas, and dissolve materials like a liquid. Furthermore, close to the critical point, small changes in pressure or temperature result in large changes in density, allowing many properties of a supercritical fluid to be fine tuned.In the pressure-temperature phase diagram (Fig. 3-2), the boiling that separates the gas and liquid region ends at the critical point, where the liquid and gas phases disappear to become a single supercritical phase[119].

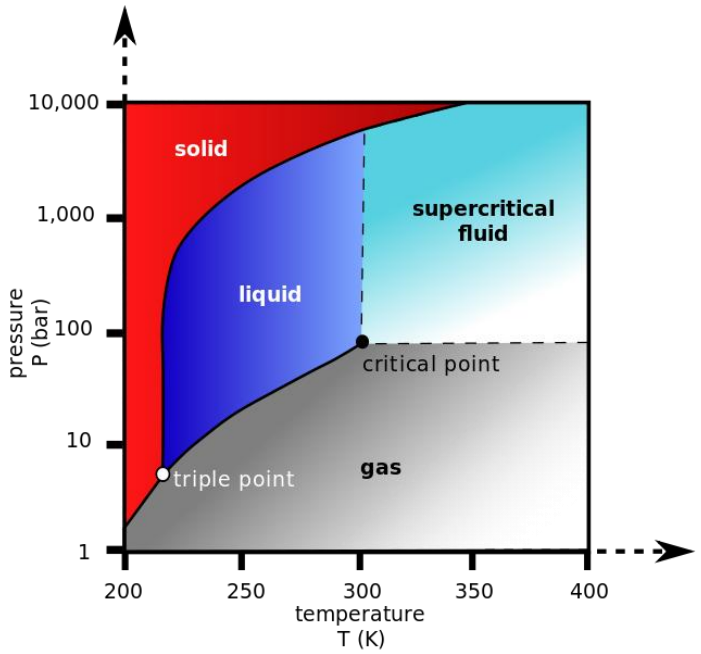

Figure 3- 2.Phase diagram of a common supercritical fluid, where P_c is the critical pressure and T_C is the critical temperature[119].

In general terms, substances in the supercritical fluid region have properties between those of gas and liquid phases[118]. From the gas phase, this supercritical region exhibits properties such as lower viscosity, higher diffusivity, expansion to fill their container and complete miscibility with other gases[118]. In the liquid phase, the supercritical region exhibits the ability to dissolve solids and has higher densities than the gas phase[118].

Table 3- 1: Density (ρ), diffusivity (D) and viscosity (η) for typical liquids, gases and supercritical fluids[118].

Comparison of Gases, Supercritical Fluids and Liquid			
	Density (kg/m^3)	**Viscosity (µPa·s)**	**Diffusivity (mm^2/s)**
Gases	1	10	1–10
Supercritical Fluids	100–1000	50–100	0.01–0.1
Liquids	1000	500–1000	0.001

Table 3-1 shows the range of values for density (ρ), viscosity (η) and the diffusion coefficient (D) for common supercritical fluids[118]. Supercritical fluids can penetrate a solid faster than liquid solvents because of higher diffusivity than the liquid phase. Combinations of these factors increase the effectiveness of permeating a solid sample. Furthermore, it is possible to transport dissolved solutes out of a sample matrix using supercritical fluids due to its low viscosity[118]. The solvent powers of supercritical fluids come from the relatively high density, which can range anywhere between gas or liquid phases. The density directly affects the solubility, providing this useful, tuneable, solvent property of supercritical fluids. Supercritical fluids are also completely miscible with other gases, compared with the very poor solubility of gases in similar solvents in the liquid phase[118,121,122]. This may prove useful in the hydriding process of Al nanoparticles by using hydrogen dissolved in supercritical fluids, which will be discussed in detail in section 3.4 of this chapter.

3.2.2 Supercritical carbon dioxide ($scCO_2$)

3.2.2.1 Properties of $scCO_2$

$ScCO_2$ is a fluid-like state of carbon dioxide at or above its critical temperature (T_c) and critical pressure (P_c)[118,123]. If the temperature and pressure are both increased from standard temperature and pressure (STP) to be at or above the critical point for carbon dioxide, it can adopt properties between a gas and a liquid. More specifically, it behaves as a supercritical fluid above its critical temperature (31.1°C) and critical pressure (72.9 atm/7.39 MPa), expanding to fill its container like a gas but with a density like that of a liquid.

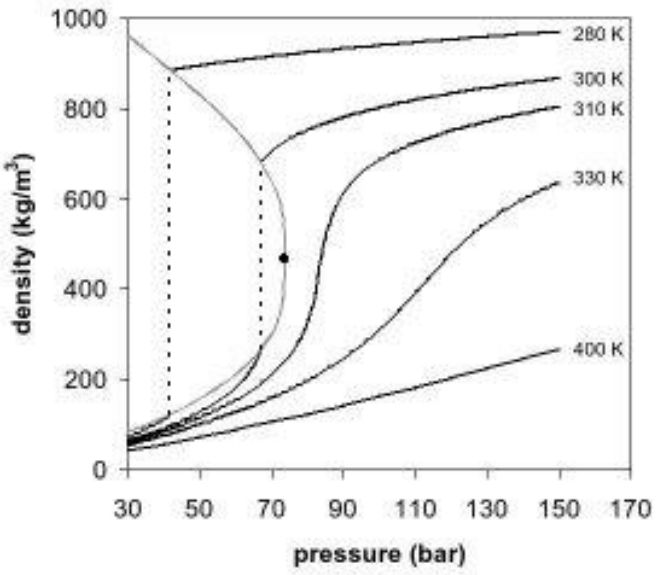

Figure 3- 3.Carbon dioxide density-pressure phase diagram [124].

The dissolving power of $scCO_2$ is due to its density[123,125]. Fig. 3-3 shows the density-pressure phase diagram for carbon dioxide[124]. At well below the critical temperature (280 K), as the pressure increases, the gas compresses and eventually (at just over 40 bar) condenses into a much denser liquid, resulting in the discontinuity in the line (vertical dotted line)[124]. The system consists of 2 phases in equilibrium, a dense liquid and a low density gas[124]. As the critical temperature is approached (304.25 K), the density of the gas at equilibrium increases, and the density of the liquid decreases [124]. At the critical point (dot in Fig. 3-3), there is no difference in density, and the 2 phases become one supercritical fluid phase[124]. Thus, above the critical temperature a gas cannot be liquefied by pressure. At slightly above the critical temperature (310 K), the pressure-density line in Fig. 3-3 is almost vertical[124]. A small increase in pressure causes a large increase in the density of the supercritical phase. Many other physical properties also show large gradients with pressure near the critical point, e.g. viscosity, the relative permittivity and the solvent strength, which are all closely related to the density. At higher temperatures, the fluid starts to behave like a gas. For carbon dioxide at 400 K,

the density increases almost linearly with pressure[124]. These factors allow $scCO_2$ to select specific materials for extraction during a supercritical fluid extraction process. This can be done by fine tuning the pressure and temperature of the $scCO_2$ to dissolve and extract only one phase of a mixture.

3.2.2.2 Applications

Supercritical $scCO_2$ has found a wide range of applications in manufacturing products, as a working fluid, in the sterilization of biomedical materials and as a solvent[126]. A hydrogenation process is one example of a chemical reaction that uses $scCO_2$ as a solvent. It was found that hydrogenation processes in $scCO_2$ exhibit higher hydrogenation rates and selectivity compared to conventional organic solvents[127,128]. This increased rate is due to (1) enhancement of dissolved H_2 concentration due to the miscibility of H_2 in $scCO_2$, (2) decrease of mass transfer resistance for the lower viscosity and higher diffusivity of $scCO_2$, (3) possible modification of substrate reactivity through molecular interactions between CO_2 and substrates and (4) possible change of catalyst specific activity via modification of metal nanoparticles[127,129].

3.2.2.3 Mixtures of $scCO_2$ and H_2

The solubility of gaseous hydrogen in common solvents is not very high[129]. However when $scCO_2$ is used as the solvent, hydrogen is completely miscible with $scCO_2$ and this is beneficial for the enhancement of hydrogenation reactions[128,129]. It was reported that the concentration of H_2 in a supercritical mixture of H_2 (85 atm) and CO_2 (120 atm) at 50°C is 3.2 M (mol/L), while the concentration of H_2 in a conventional solvent such as THF (tetrahydrofuran) under the same pressure is merely 0.4 M[108]. Therefore, heterogeneous reactions involving these gases may become homogeneous reactions in

sc-CO_2 (where reactants exist in the same phase), and the speed and yield of such reactions can be greatly improved[108]. Another study[109] showed that *sc*-CO_2 with 1% addition of H_2 (Fig. 3-4) showed a diffusion coefficient an entire order of magnitude larger than pure *sc*-CO_2.

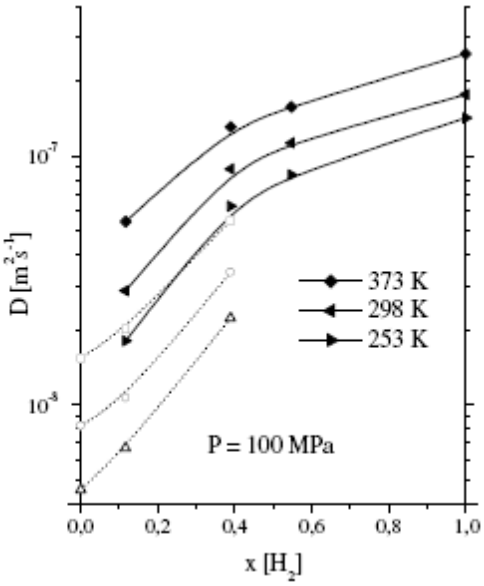

Figure 3- 4.Isobars of the concentration dependence in the binary mixture CO_2 / H_2 (full symbols, H_2: open symbols, CO_2)[109].

Organic or inorganic compounds can be added to supercritical fluids to further increase its solvent power[119]. With regards to $scCO_2$, tetrahydrofuran (THF), diethyl ether (Et_2O) or methyl oxide (Me_2O) can be added to assist in dissolving or suspending the hydrogen storage material and catalysing absorption[98]. In this patent, a Me_2O compound has been used and a room temperature combination of H_2 (10 - 40 bar) and CO_2 (60 - 80 bar) becomes supercritical when heated to 60 – 100°C[98]. It was reported that 0.3 wt.% H_2 was adsorbed into Al during the $scCO_2$ /H_2 process[98].

3.3 Results and discussions

The mechanochemical reaction of $AlCl_3$ + 3Li → Al + 3LiCl proceeded to completion through the reduction of $AlCl_3$ with lithium to form Al nanoparticles and LiCl as the reaction products. These Al nanoparticles were embedded within a buffer (LiCl) matrix that was later removed through a washing procedure. In order to understand the effect of different buffer quantities on the particle size distribution and agglomeration of Al, samples were milled for 6 h with different LiCl:Al volume ratios of 6.786:1 (sample A), 9.665:1 (sample B) and 12.544:1 (sample C) as outlined in Table 3-2. It was expected that larger Al particles would be formed using low levels of buffer and smaller Al particles would be formed in samples with high buffer. In lower levels of buffer, because the volume fraction of the buffer phase is low, it cannot restrain the particle growth and agglomeration of the crystallites. In higher levels of buffer, the volume fraction of the buffer phase is sufficient to prevent particle agglomeration during mechanochemical reaction and therefore controls the particle size distribution.

Table 3- 2:Al samples synthesis details.

Sample	Ball to powder ratio	Pre-milling time (h)	Milling time (h)	LiCl buffer (g)	Product volume ratio (LiCl:Al)
A	35:1	12	6	0	6.786:1
B	35:1	12	6	2	9.665:1
C	35:1	12	6	4	12.544:1

Fig 3-5a shows XRD patterns of as-milled (unwashed) samples A, B and C. The patterns consist of peaks associated with Al and LiCl. A new peak associated with $LiAlCl_4$ was observed in the pattern of sample A. This suggests that the reaction between Li and $AlCl_3$ undergoes a secondary reaction of the $4AlCl_3 + 3Li \rightarrow Al + 3LiAlCl_4$ due to excess $AlCl_3$ being used. The $AlCl_3$ peak is not present in the XRD pattern as it often undergoes significant crystalline deformation during milling. No other peaks are evident in all unwashed samples, which suggest that the reaction was complete.

Fig. 3-5b shows XRD patterns of washed samples A, B and C. After washing with a tetrahydrofuran (THF) solvent, the presence of only Al peaks indicates the successful removal of the LiCl phases, however it is likely that trace of LiCl is still present in undetectable quantities (<1 wt.%). Some $LiCl.H_2O$ was detected in the sample B due to free water either reacting during milling in a slightly unsealed vial or acquired during transfer and unintentional handling of the hygroscopic powder outside of the argon filled glove box[115].

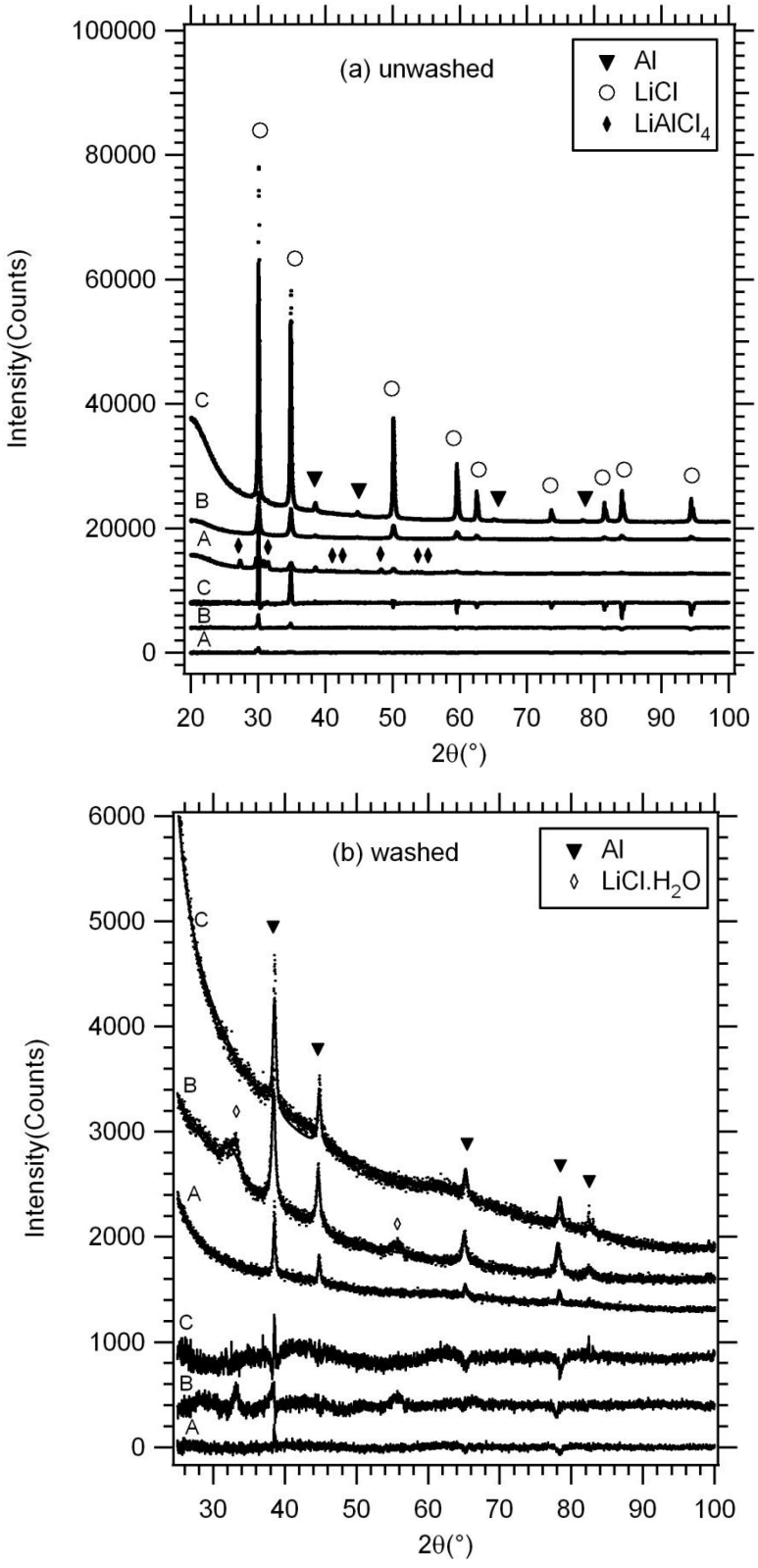

Figure 3- 5.XRD patterns of (a) unwashed and (b) washed sample A, B and C.

All XRD patterns in Fig. 3-5 were analysed using the Rietveld method in TOPAS (Bruker AXS). Rietveld fitting results are provided in Table 3-3 that outline phase wt.% and crystallite sizes of unwashed and washed Al samples. Al crystallite sizes decreased from 22.1 ± 1.0 nm to 13.8 ± 4.5 nm for unwashed sample A and C respectively. For washed samples, Al crystallite sizes decreased from 19.3 ± 0.6 nm to 12.1 ± 0.7 nm for sample A and C respectively. The addition of LiCl led to a reduction of the Al crystallite size. However further increase in the LiCl:Al volume ratio has little effect on the Al crystallite size as revealed by the small difference in Al crystallite size for sample B and C. Both XRD crystallite sizes and SAXS particle sizes (in Fig. 3-9) show similar trends although crystallite size and particle size are different.

For reaction $AlCl_3 + 3Li \rightarrow Al + 3LiCl$, all the starting reagents were individually pre-milled prior to use. Therefore the starting reagent with smaller particles size is formed. During a mechanochemical reaction, deformation, fracture and welding of these reactant particles occur repeatedly during ball/reactants collision events. Plastic deformation of the particles occurs, which decompose into sub-grain boundaries. With further milling, the sub-grain size decreases and nanometer size sub-grain boundaries become randomly oriented. As a result, the reaction products inherit the nanoscale microstructure of the reactants. Such nanocomposite structures can be converted into nanoparticles by selective dissolution of one phase, provided the grains of the insoluble phase do not percolate through the milled particles[58]. Furthermore, using LiCl:Al volume ratios from 6.786:1 to 9.665:1 during this mechanochemical reaction helps to separate the synthesized particles, essentially restricting particle growth and promoting nanoparticle formation. Combination of these small starting reactants particles and buffer have resulted an effective reaction volume. As the result of this effective reaction volume, a reduction of the Al crystallite and particle size was obtained. The same factors are also applied on synthesising MgH_2 nanoparticles (down to ~7 nm) using mechanochemical reaction[53,130]. However, increasing the LiCl:Al volume ratios from 9.665:1 to 12.544:1 has little effect on the synthesized Al particle size. At this point, the

effective reaction volume is mainly associated with the particle size of the starting reactants rather than buffer content, providing the same milling condition is applied. This was due to the starting reagents all being individually pre-milled prior to use. This result is consistent with the previous study of the synthesis of ZnS nanoparticles using the mechanochemical method[63,131].

Table 3- 3:Rietveld results for XRD patterns in Figure 3-5 from unwashed and washed mechanochemically synthesized Al using LiCl:Al volume ratios of 6.786:1 (sample A), 9.665:1 (sample B) and 12.544:1 (sample C) respectively. Mathematical fitting uncertainties are provided (2 standard deviations).

Samples	Phase	Wt.%	Crystallite size (nm)
Unwashed A	Al	9.9 ± 0.4	22.1 ± 1.0
	LiCl	46.2 ± 0.6	11.5± 0.3
	$LiAlCl_4$	43.9 ± 0.7	33.0 ± 1.6
Unwashed B	Al	5.0 ± 0.7	16.0 ± 1.6
	LiCl	94.9 ± 0.7	16.7 ± 0.3
Unwashed C	Al	5.2 ± 0.5	13.8 ± 4.5
	LiCl	94.8 ± 0.5	38.6 ± 0.7
Washed A	Al	100	19.3 ± 0.6
Washed B	Al	54.2 ± 3.6	11.9 ± 0.4
	$LiCl.H_2O$	45.8 ± 3.6	3.3 ± 0.6
Washed C	Al	100	12.1 ± 0.7

Fig. 3-6 shows TEM images of washed sample A, B and C. TEM images of washed samples consist of large aggregates and agglomerates of smaller Al particles. Nanoparticles were found to be ~10 - 50 nm. LiCl buffer prevents Al particle growth by physically separating the nanoparticles during milling, but after the salt is removed by washing, nanoparticles come into contact and particle agglomeration can occur.

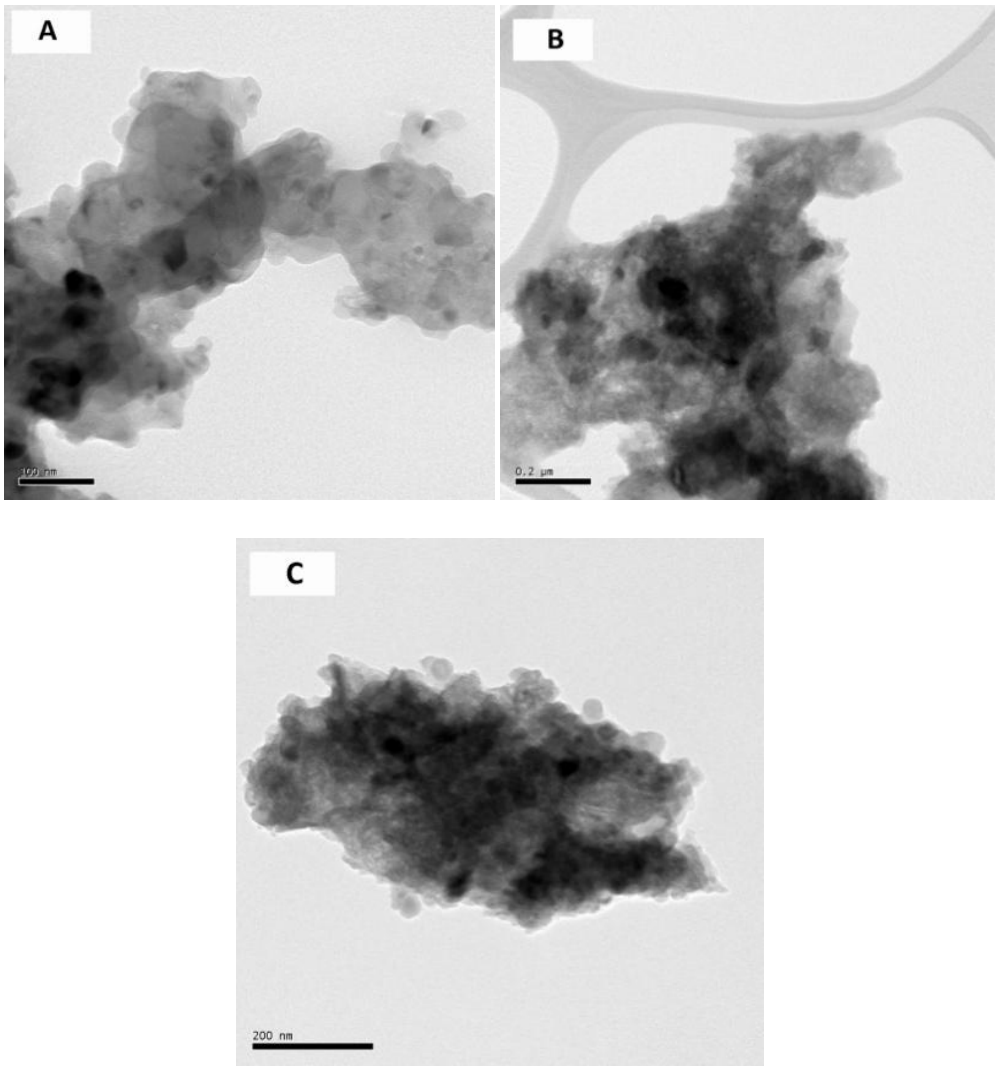

Figure 3- 6.TEM micrographs of washed sample A, B and C.

Fig. 3-7 shows HRTEM micrographs of unwashed and washed sample C. The distance between lattice fringes was found to be 2.33 Å, which is in good agreement with the *d*-spacing of (111) *hkl* planes of Al (2.31 Å). EDS data as provided in Fig. 3-8B also verifies the presence of high quantities of Al and low quantities of Cl in washed samples suggesting that the washing process was close to completion. The unwashed samples shown in Fig. 8A were identified to be Cl-rich. EDS also showed the existence of O for both samples, as a result of unavoidable TEM sample air exposure. Si, Cu and C are present from the TEM grid component.

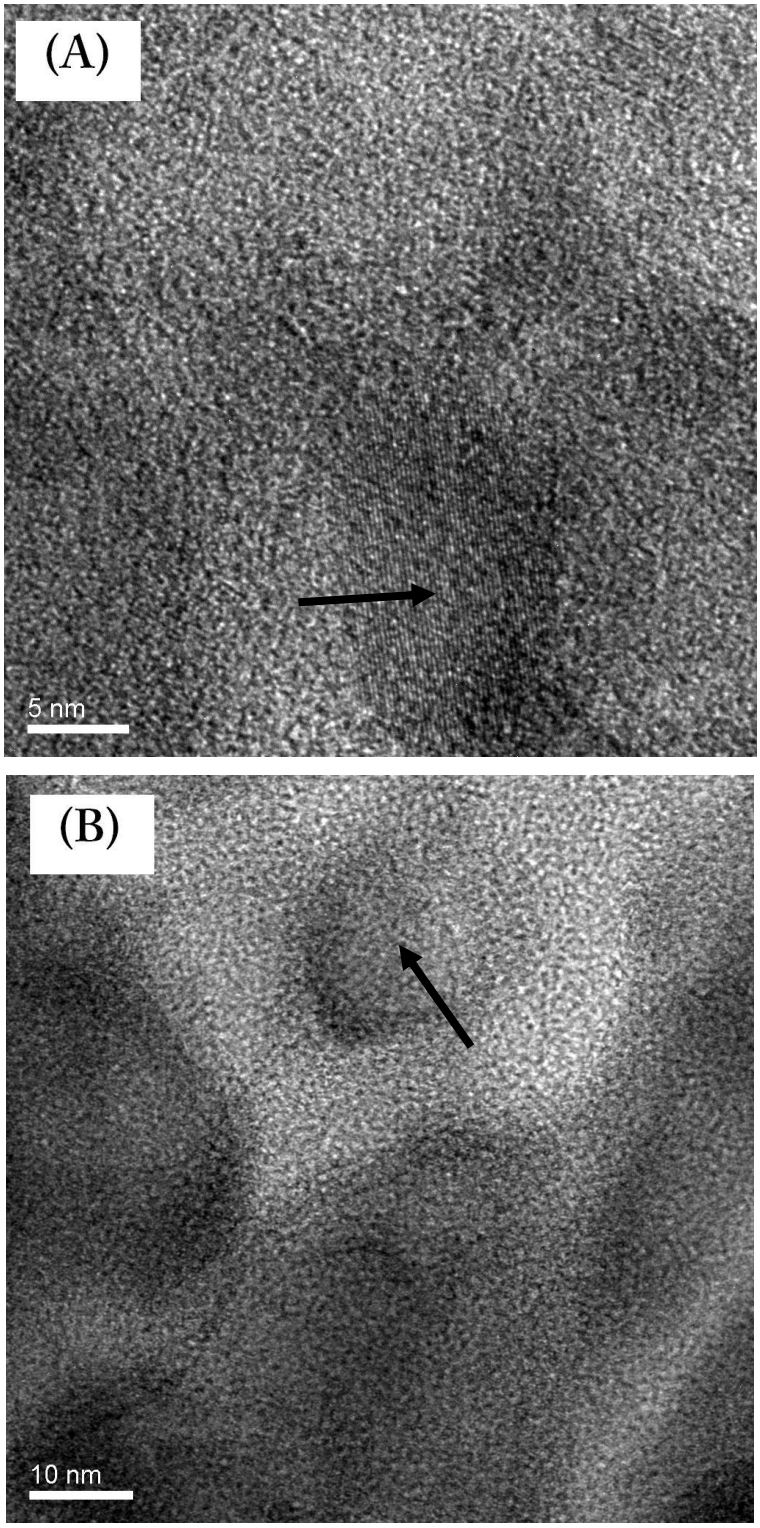

Figure 3- 7.HRTEM micrographs of lattice fringing (shown by the black arrow) of unwashed (A) and washed (B) samples C.

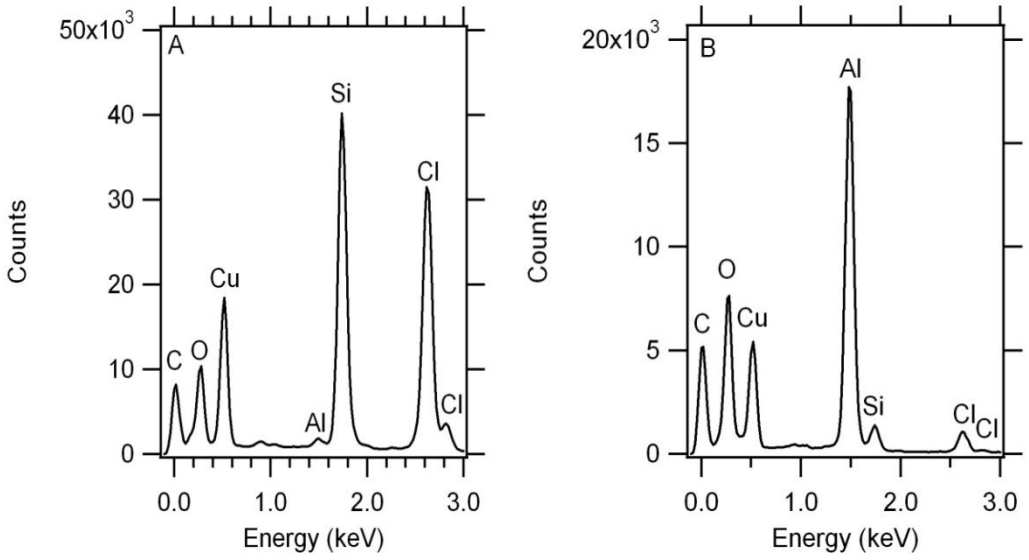

Figure 3- 8.EDS spectroscopy of (A) unwashed and (B) washed sample C.

Fig. 3-9 shows SAXS data for the washed Al nanoparticles. A power law relationship between scattered intensity and the scattering vector *q* dominates the data set and there is a hump in the data set at low-*q*, which has been attributed to a Guinier region generated by the average aluminium nanoparticle size. The data was modelled using the unified equation[70] with the Irena package[71] for Igor Pro (Wavemetrics, Oregon, USA). It is reasonable to assume that the particles are roughly spherical from TEM investigations so that the radius of gyration can be related to the aluminium particle size via $R_g = \sqrt{3/5}r$ where *r* is the particle radius, resulting in an overall average particle size (diameter) of 55 nm (sample A), 15 nm (sample B) and 13 nm (sample C) respectively.

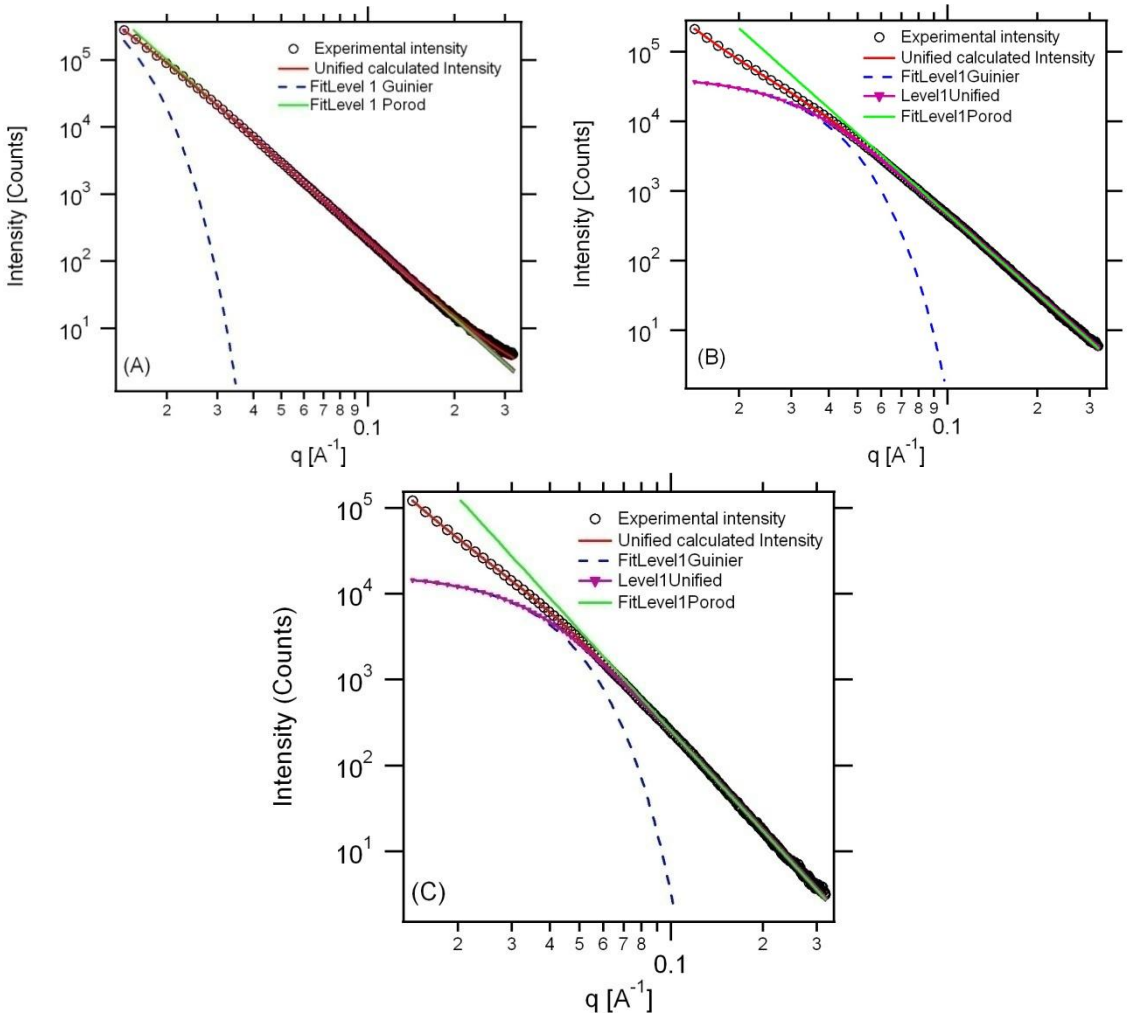

Figure 3- 9.SAXS data from washed sample A, B and C with average particle size of 50 nm, 15 nm and 13 nm respectively.

Hydrogen absorption measurements were performed on unwashed and washed Al sample using sample C as these particles were the smallest to be synthesised. A reaction between Al and hydrogen to form AlH_3 was attempted using $scCO_2$ fluid as a reaction medium. A mixture of H_2 (150 - 250 bar) and CO_2 (150 - 200 bar) was heated to 40 – 50 °C, thereby forcing the CO_2 to become a supercritical phase and the H_2 to dissolve within. The Al samples were held within this supercritical phase for 1 week with no hydrogen absorption detected using either the $ScCO_2$ rig (pressure measurements), the Sievert apparatus or XRD measurements (phase identification).

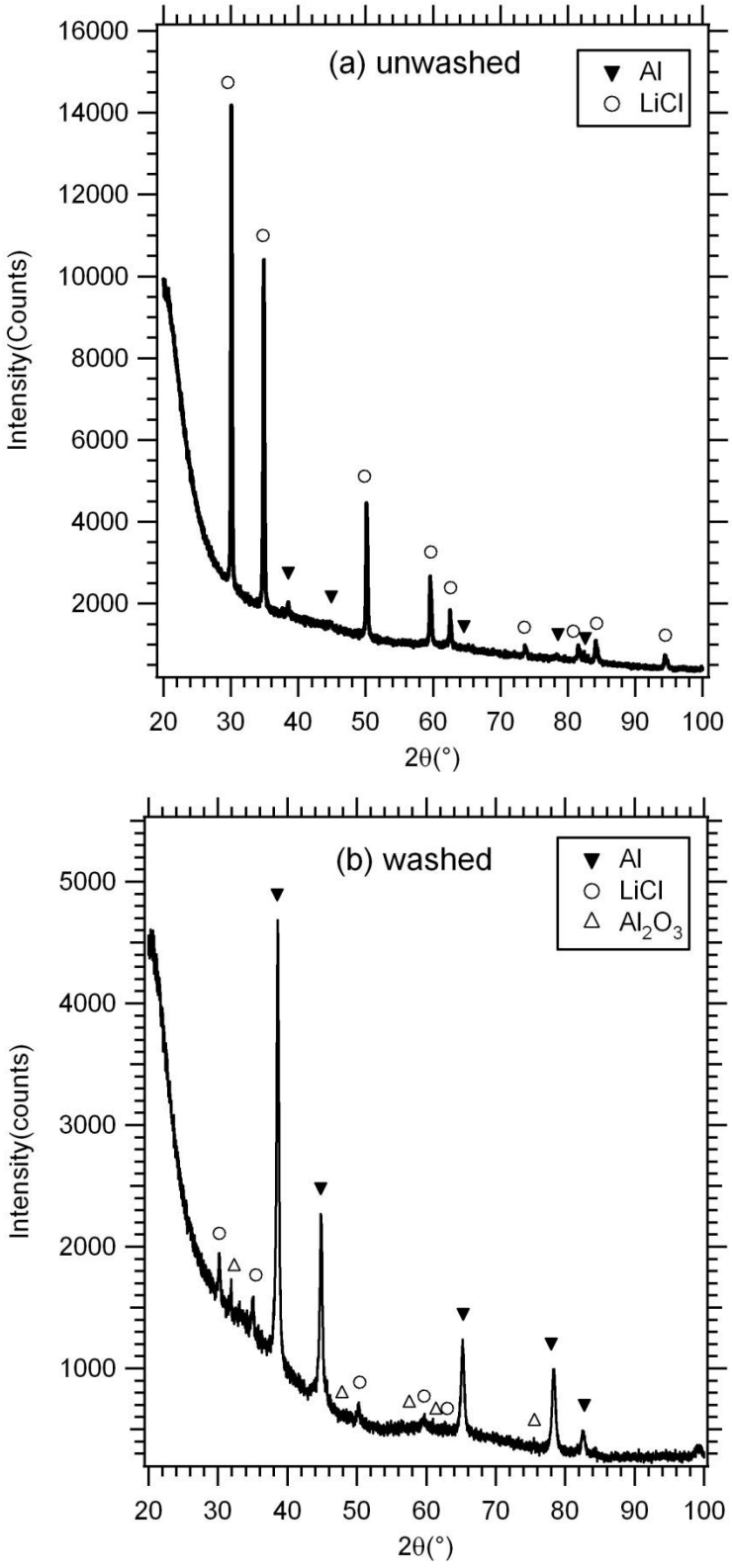

Figure 3- 10.XRD patterns of (a) unwashed and (b) washed sample C after $scCO_2$ / H_2 reaction.

The XRD pattern of the unwashed and washed sample C after the attempted $scCO_2/H_2$ reaction is shown in Fig. 3-10. AlH_3 was not detected in either sample. Several small peaks related to Al_2O_3 were observed in the pattern of the washed sample. No Al_2O_3 peaks were detected in the unwashed sample. This was due to the unwashed particles being surrounded by buffer phase. The oxidation of Al in CO_2 is a theoretical certainty[122] based on Al standard enthalpies of formation in the forward direction of equation (3.2).

$$2Al + 1.5CO_2\,(g) = Al_2O_3 + 1.5C \quad \textbf{(3. 2)}$$

$$AlH_3\,(s) \rightarrow Al\,(s) + 3/2H_2\,(g) \quad \textbf{(3. 3)}$$

From table 3-4, reaction in equation (3.2) proceeds in the direction in which $\Delta G < 0$ indicating that Al thermodynamically favours oxidation over conversion to AlH_3. Although this format of calculation does not consider the kinetics of the oxidation process, based on the XRD pattern in Fig. 3-10, it shows that the speed of the oxidation process was significantly faster than the forward hydriding process in equation (3.3) during $scCO_2/H_2$ reaction. The presence of this oxide layer (Al_2O_3) on Al nanoparticles can be detrimental to molecular[132] and even atomic[133] hydrogen permeation. Furthermore the rate of hydrogen transport through a surface layer of Al_2O_3 was found to decrease rapidly with oxide thickness of only 1 - 3 nm[134,135]. Thus, the properties and the thickness of the oxide layer may be the most important limitation on the rate of hydrogen uptake attempted herein.

Table 3- 4:Standard enthalpy (*ΔH*) and entropy (*ΔS*) values are used to determine the change in Gibbs free energy (*ΔG*) per mol of Al in equation (2) over the temperature range -23 - 127°C.

Temperature (°C)	Δ*H* (kJ)	Δ*S* (JK^{-1})	Δ*G* (kJ)
-23.1	-542.2	-157.2	-502.9
26.8	-542.7	-158.8	-495.0
76.8	-543.0	-159.7	-487.1
126.8	-543.1	-160.0	-479.1

It is expected that the thermodynamics and kinetics properties of the Al-H system will be altered by using Al nanoparticles[93]. Studies have shown an increase in the kinetics of desorption when using smaller particle size[54,94]. Significant changes in thermodynamic properties are theoretically predicted for Al nanoparticles smaller than its critical particle size (1 nm)[50,52]. Below its critical size, the total energy becomes more positive as shown in Fig. 3-11[50]. This result suggests that the Al-H system becomes more thermodynamically unstable. Above this critical size, the total energy is almost constant and similar to that of the bulk Al. Therefore hydrogen can absorb easily into nano Al below its critical size, a consequence of its highly unstable system. If the predicted critical particle size (1 nm) is correct and compared to the hydrogen absorption measurement attempt herein (using Al with 13 nm particle size), then it has been experimentally demonstrated that no significant changes in thermodynamics sorption properties when Al nanoparticles larger than its critical particle size were used. This result is also consistent with the previous experimental study using Al with 30 - 50 nm particles size with no hydrogen absorption was reported[91].

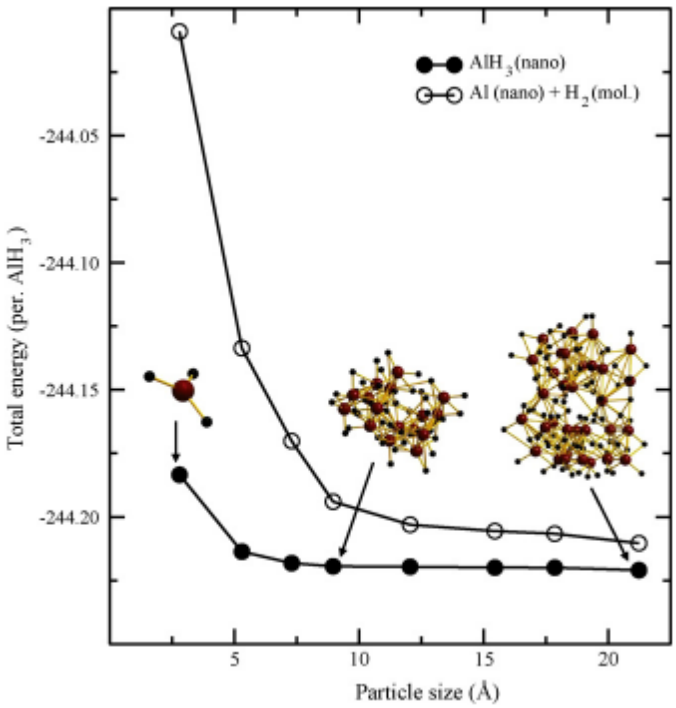

Figure 3- 11.Calculated total energy as a function of particle size for the AlH_3 nano-clusters and nano particles of Al with the H_2 molecule (i.e. $E_{Al}(nano) + (3/2)E_{H_2}(mol)$) [50].

Furthermore, the mechanism which reportedly allowed H_2 to be absorbed more effectively in a supercritical medium for Al is still not fully understood. Although 0.3 wt.%[98] and 0.0178 ± 0.0005 wt.%[122] H_2 was reported to absorb during the $scCO_2/H_2$ process, no explanation is given on what mechanism allows H_2 to permeate the Al surface in a supercritical medium. It should also be noted that these findings have not been published in the scientific literature to date, and may not be reproducible. There might be a possibility that $scCO_2$ alters the chemical reaction, catalyses the dissociation of diatomic hydrogen molecules or simply permeates the Al surface and carries the H in with it. The experimental methods used to determine the 0.3 wt.% H_2 absorbed into Al during $scCO_2/H_2$ process was not described[98]. The released gas was not confirmed as hydrogen in both experiments[98,122]. It is possible that the released gas was actually some impurity or excess CO_2 that was trapped beneath the surface during the $scCO_2/H_2$ process.

3.4 Conclusion

Al nanoparticles were synthesised by mechanochemical reactions of $AlCl_3$ + 3Li → Al + 3LiCl using different LiCl:Al volume ratios (6.786:1 , 9.665:1 and 12.544:1). Sample synthesised without addition of buffer led to the formation of Al nanoparticles with average particle size of 50 nm. Addition of sufficient quantity of buffer resulted in the formation of Al with average particle sizes down to 13 nm. The addition of LiCl as a buffer helps to separate the synthesized Al particles, essentially restricting particle growth and promoting nanoparticle formation. A hydriding reaction by using combination of Al nanoparticles (13 nm) and $scCO_2$ media showed no H_2 absorption. This indicates that Al particle size less than its critical particle size (< 13 nm) are required to introduce hydrogen into pure Al at pressure and temperature attempt herein (73.8 bar and 31.1°C). Furthermore, the oxidation of Al in CO_2 occurred during $scCO_2/H_2$ reaction forming an oxide layer (Al_2O_3) on Al nanoparticles. The presence of this oxide layer limited the rate of hydrogen permeation on Al nanoparticles.

3.5 Future work

Based on theoretical[50,52] and experimental[96] studies, pure Al nanoparticles must be synthesised < 1 nm in order to cause significant thermodynamic destabilisation of Al-H system. This can be accomplishing by incorporating pure Al into a mesoporous silica scaffold or within a nanoporous carbon scaffold (nanotube or aerogel) because the pore size can be synthetically adjusted and these scaffolds are relatively inert. The scaffold serves as an effective structure-directing agent that restricts the particle size of the Al while providing a framework that mitigates sintering. Alternative supercritical fluids that do not create an oxide layer on the Al particle surface should be investigated and explored. Organic or inorganic compounds can be added to the alternative supercritical fluids to increase its solvent power. Although we could hydride the Al nanoparticles

below its critical size to form AlH_3, on the other hand these AlH_3 would want to decompose very quickly due to its fast kinetics with such a small particle size.

CHAPTER 4: Aluminium trihydride nanoparticles

4.1 Introduction

Aluminium trihydride (AlH_3) is a metastable, crystalline solid with a volumetric hydrogen density of 0.148 kg H_2/L and a gravimetric hydrogen density of 10.1 wt.%. It has been used as a reducing agent, explosive, rocket fuel, hydrogen source for portable power system, military applications and automotive applications[93,136,137].

4.1.1 Synthesis

$AlH_3$was first synthesized in 1942 when were it was prepared as an $AlH_3.2N(CH_3)_3$ (amine complex)[138]. A few years later in 1947 an ethereal solution of $AlH_3$was synthesized by a reaction between LiH (or $LiAlH_4$) and $AlCl_3$ in diethyl ether without removing the ether as shown in reaction (4.1) and (4.2) respectively[139].

$$\mathbf{3LiH + AlCl_3 + \mathit{n}Et_2O \rightarrow AlH_3.\mathit{n}Et_2O + 3LiCl} \quad \textbf{(4. 1)}$$

$$\mathbf{3LiAlH_4 + AlCl_3 + \mathit{n}Et_2O \rightarrow 4AlH_3.\mathit{n}Et_2O + 3LiCl} \quad \textbf{(4. 2)}$$

In 1955, an effort to remove the ether from the alane succeeded by filtering the etherated AlH_3solution into an inert liquid followed by drying under a vacuum for 12 hours[140]. Approximately 20 years after this a total of seven phases of AlH_3 were synthesized and characterized. This approach was similar to the AlH_3 developed in 1947 and 1955 but with an additional desolvation reaction after the formation of etherated AlH_3 solution. The desolvation reaction involved the heating of a solution of etherated AlH_3 in a mixture of ether and benzene. An excess of $LiAlH_4$ or $LiBH_4$ was also added to

the etherated AlH_3solution in order to decrease the desolvation temperature and to control AlH_3 etherate separation. Finally the AlH_3 was washed with diethyl ether or dilute acid to remove the excess $LiAlH_4$ or $LiBH_4$[141]. The typical reactions involved in synthesizing microcrystalline α-AlH_3 (100 - 200 nm) are shown in reaction (4.3) and (4.4).

$$\mathbf{4LiAlH_4 + AlCl_3 + Et_2O \rightarrow 4AlH_3.nEt_2O + 3LiCl \downarrow + LiAlH_4 + Et_2O} \quad \textbf{(4. 3)}$$

$$\mathbf{4AlH_3.nEt_2O + LiAlH_4 + LiBH_4 + Et_2O \rightarrow 4AlH_3 + Et_2O \uparrow + LiAlH_4 \downarrow + LiBH_4 \downarrow} \quad \textbf{(4. 4)}$$

Based on reactions (4.3) and (4.4), many other AlH_3 phases have been synthesized through slight modification of the reaction temperature, time and techniques.

The γ-AlH_3 phase (space group *Pnnm*) can be prepared by heating at a lower temperature (~60 °C) without using excess $LiBH_4$. Another approach involved grinding a dry mixture of AlH_3 etherate with $LiAlH_4$ and heating to 70 – 80 °C under vacuum. The β-AlH_3 phase (space group $Fd\bar{3}m$) typically forms within the first 1 - 2 hour along with γ-AlH_3 phase during reaction (4.3) and (4.4). Desolvation in a sealed pressure reactor or reacting $LiAlH_4$ with $AlCl_3$ using a cryomill has been used to prepare α'-AlH_3 phase[141,142]. AlH_3 with different phases has also been synthesized using mechanochemical[143] and cryomill[142-145] techniques.

AlH_3 can be synthesized by using different starting materials. $LiAlH_4$ in reaction (4.5) can be replaced by other complex hydrides containing such as AlH_4^-, AlH_6^{3-}, AlH_5^{2-}, BH_4^- and NH_2^- anions with alkali metals, alkaline earth metals and transition metals as counter ions[144]. Furthermore $LiAlH_4$ may also be replaced by binary hydrides of alkali metals, alkaline earth metals and 3d transition metals[144]. $AlCl_3$ may be replaced by $AlBr_3$ and AlI_3 or halides from alkali, alkaline earth metals, transition metals, Ga or In [144]. From these reactions a halide is expected to be formed as a by-product in addition to AlH_3.

$$3LiAlH_4 + AlCl_3 \rightarrow 4AlH_3 + 3LiCl \quad \textbf{(4. 5)}$$

4.1.1.1 Mechanochemical

The mechanochemical technique involves mechanical activation of solid-state reactions causing collisions between reactant particles and balls inside the mill. A solid-state reaction allows the reactant particles to chemically react without the presence of a solvent. It is a simple, economical and environmentally friendly technique. During milling, repeated deformation, fracture and welding of reactant particles occur during ball/powder collision events[58,131,146].

The mechanochemical technique for synthesizing AlH_3 at room temperature resulted in a mixture of α-AlH_3, α'-AlH_3 and Al phases[142-144], showing that mechanochemical milling at room temperature can provides more than enough energy to allow AlH_3 to release hydrogen and form aluminium metal nanoparticles. The number of AlH_3 phases can be controlled by using different ball to powder ratios, ball sizes, milling temperature and milling time[142-144]. Approximately 50% of the synthesised AlH_3 decomposes to Al during the first hour of milling when higher ball to powder ratio and larger balls were used[143]. The number of AlH_3 phases was reported to decrease with increased milling time[143,144].

4.1.1.2 Cryomill

The cryomilling technique originally evolved as a variation of mechanical milling and involves putting the milling media in liquid nitrogen (approximately 77K), and using processing parameters in order to gain nanostructured particles. The advantages of using cryomilling compared with milling at room temperature is that the extremely low temperature of liquid nitrogen will suppresses recovery and recrystallization and leads to finer grain structures and more rapid grain refinement[61]. Cryomilling forms high AlH_3 yields and minimises the decomposition of AlH_3 to Al compared to room temperature

milling[143]. AlH_3has also been reported to form by cryomilling alanate and aluminium halides or by adding additives[144]. Another study shows that the α'-AlH_3 phase synthesized from cryomilling decomposes either partially by a single reaction step (equation 4.6) or by two decomposition steps (equation 4.7)[144,145].

$$\alpha'\text{-}AlH_3 \rightarrow Al + (3/2)H_2 \quad \textbf{(4. 6)}$$

$$\alpha'\text{-}AlH_3 \rightarrow \alpha\text{-}AlH_3 \rightarrow Al + (3/2)H_2 \quad \textbf{(4. 7)}$$

4.1.2 Structures

AlH_3 can exist in several crystal structure phases (α, α', β, γ, δ, ε and ζ) depending on different ways of synthesizing AlH_3[93,141,147]. The α-AlH_3 phase crystallises in the trigonal space group, $R\bar{3}c$, with a hexagonal unit cell. The structure consists of corner connected AlH_6octahedral with normal bridge bonds, Al-H-Al. This structure is also similar to α'-AlH_3 and β-AlH_3 phases which crystallise in an orthorhombic *Cmcm* and cubic space group respectively[142,148]. On the other hand, the structure for γ-AlH_3 phase which crystallizes in the orthorhombic *Pnnm* space group consists of double-bridge bonds, Al-2H-Al in addition to the normal bridge bonds. As a result, both corner and edge connected AlH_6 octahedra are present in γ-AlH_3 phase[147,149]. All structures and morphologies of AlH_3 phases are shown in Fig. 4-1 and Fig. 4-2.

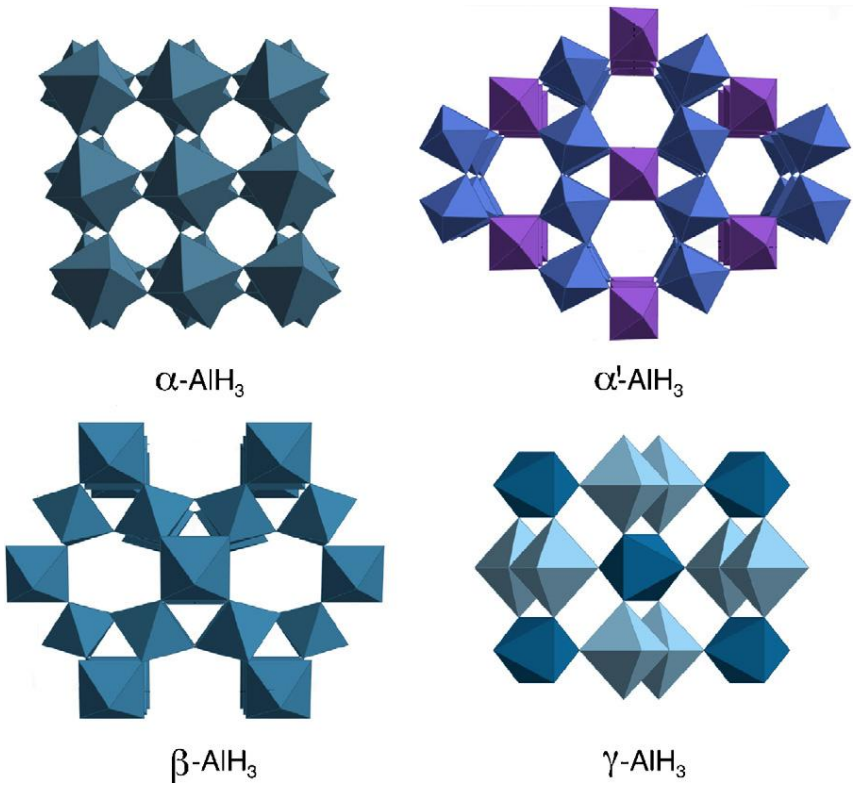

Figure 4- 1.Structures of α-AlH_3, α'-AlH_3, β-AlH_3 and γ-AlH_3[93].

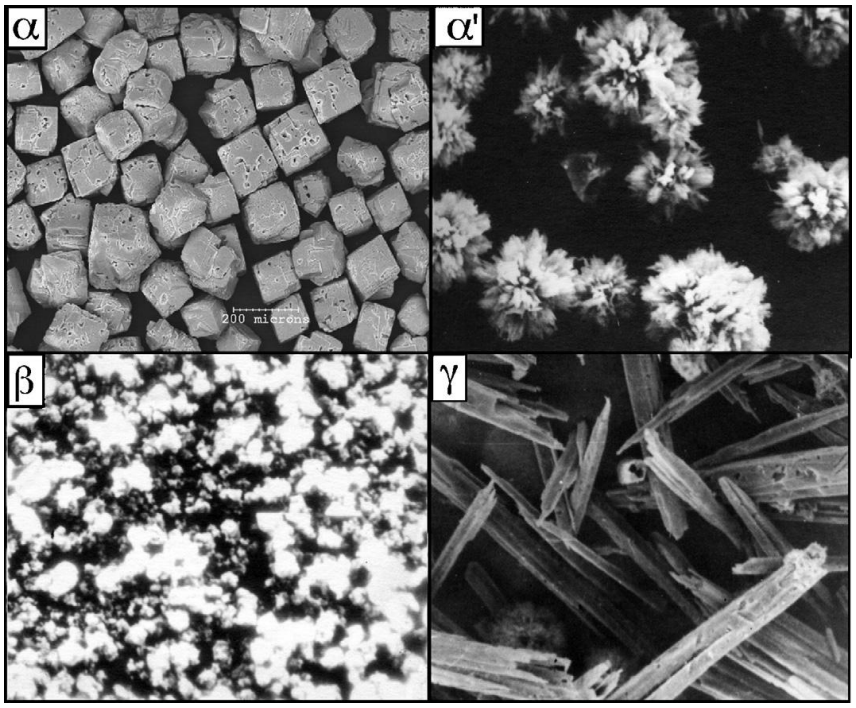

Figure 4- 2.Morphologies of α-AlH_3, α'-AlH_3, β-AlH_3 and γ-AlH_3 phases[93].

4.2 Kinetics

Earlier kinetic studies of AlH_3 decomposition were all focused on α-AlH_3 which was prepared by the Dow Chemical Company[54,102,150-155]. Recently the study was conducted on freshly synthesised β, γ and α-AlH_3[156]. The Dow AlH_3 samples consist of large particles (50 - 100 µm) and had a thick surface oxide layer. For freshly synthesised AlH_3 samples, they consist of small particles (100 - 200 nm) and had a relatively oxide-free surface.

It was also found that freshly prepared alane has much smaller activation energy (E_a) and Arrhenius parameters (A and σ) compare to Dow prepared alane (Table 4-1). These are due to the reduced particle sizes and reduced surface oxide layers in the freshly prepared samples. However a similar study on larger crystallites of α-AlH_3 showed activation energy (104 kJ/mol)[157], similar to the value measured from the smaller 100 - 200 nm particles (102 kJ/mol). This suggests that the enhanced stabilization (higher activation energy) in Dow alane is primarily due to thick oxide layer rather than the crystallite size (which has a smaller effect)[93,157].

Table 4- 1:Kinetic values (E_a, A and σ) for the alane phases[152,158]. The E_a was determined from the slope of an Arrhenius plot (*ln (k) versus 1/T*). A and σ were determined from $k(T) = Aexp\left(\frac{-E_a}{RT}\right)$ and $k(T) = \frac{k_B T}{h}\sigma exp\left(\frac{-E_a}{RT}\right)$ respectively.

Reference	Phase	$E_a(kJ/mol)$	A	σ
[156]	$\alpha - AlH_3$	102.2±3.2	1.2×10^{10}	1.9×10^{-3}
	$\beta - AlH_3$	92.3±8.6	8.8×10^{8}	1.4×10^{-4}
	$\gamma - AlH_3$	79.3±5.1	8.5×10^{6}	1.4×10^{-6}
[152]	$\alpha - AlH_3$	150.3±10.0	3.5×10^{16}	-
[157]	$\alpha - AlH_3$	104	-	-

These hydrides decompose into aluminium metal and hydrogen gas. For α-AlH_3 phase, it decomposes in a direct decomposition step: α-AlH_3→Al+(3/2)H_2 while for β and γ-AlH_3 phases, two decomposition steps occurs: (1) β or γ-AlH_3→Al+(3/2)H_2 and (2) β or γ-AlH_3→α-AlH_3→Al+(3/2)H_2[158-160]. Below 100 °C, some of these phases undergoing direct decomposition (step 1) while the remaining phase first transforms to α-AlH_3 and followed by decomposition (step 2). At elevated temperatures (>100 °C), these phases transform to the α-AlH_3 followed by decomposition (step 2). It was found that the direct decomposition of the β or γ-AlH_3 is faster compare to α-AlH_3 due to their less stability with respect to α-AlH_3.

There was significant decrepitation from the decomposition of AlH_3 to Al and H_2[153,161] which were contrary to findings by Sandrock *et al.*[54]. Theoretically when α-AlH_3completely desorbs to form Al cuboid and evolving hydrogen gas, the density increased from 1.486 to 2.71 g/cm^3. This is due to crystal size and transformation structure from hexagonal α-AlH_3 (lattice parameter: *a*=4.449 Angstrom and *c*=11.804 Angstrom[162] to face centered cubic (fcc) Al (*a*=4.0496 Angstrom[163]).

Recent interest in using AlH_3 for low temperature fuel cell applications has led many studies being undertaken to destabilizing the hydride and enhancing its decomposition rate. Fuel cell required rapid hydrogen evolution rates at low temperature (100 °C). A reduction in particle size by using ball milling reduced the temperature for AlH_3 decomposition (hydrogen desorption)[54,155] and enhanced the hydrogen desorption rate [93,164] as shown in Fig. 4-3[93].

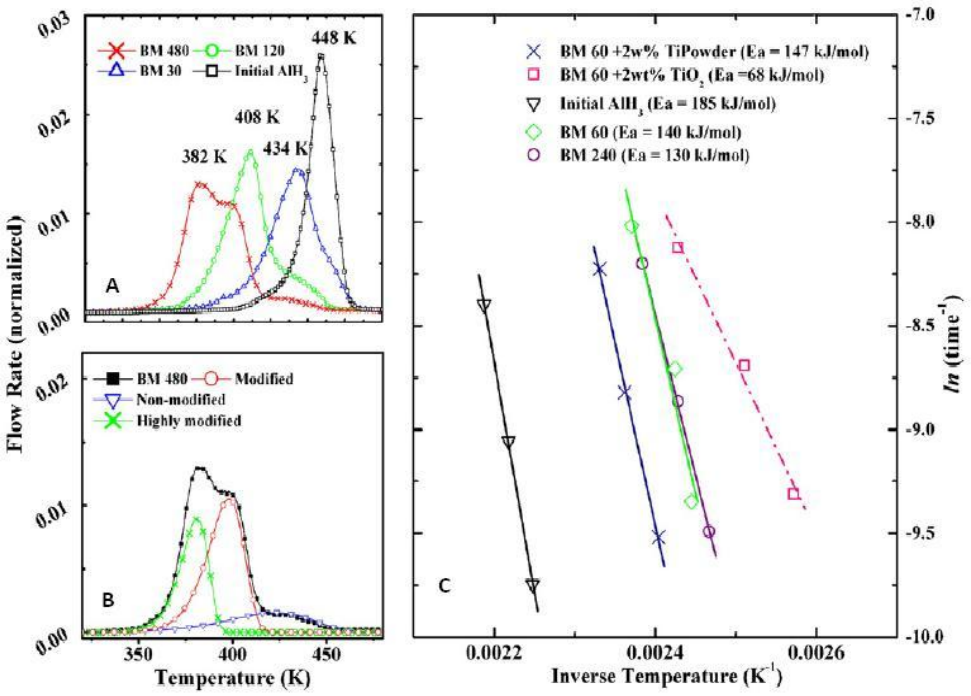

Figure 4- 3.Effect of different ball milling times on decomposition rate (A), effect of ball milled Dow Chemical sample for 480 min.TDS spectrum showing its significant destabilization and formation of two different fractions with reduced stabilities (B) and effect of milling and addition of Ti in reducing activation energy are shown from the Arrhenius plot (C)[93].

Thermal stability was found to be decreasing with decreasing crystal size and defect[141]. The effect of particle size on the thermal stability of AlH_3 is a product of solid-phase reaction kinetics as given by NMR measurements[165] and shown in Fig. 4-4. The fact that particle is related to the kinetics indicates that the decomposition reaction occurs at the grain surface which would be due of its defect nature.

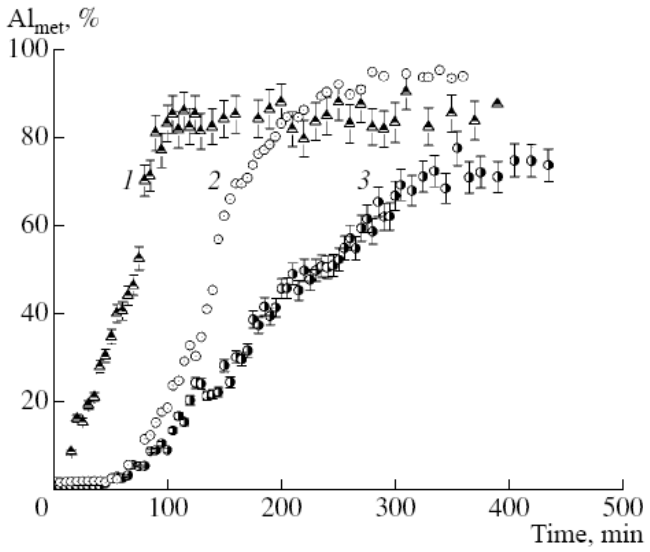

Figure 4- 4.Isothermal kinetic curves of metallic Al content in the thermolysis of AlH_3. Measurement were conducted using NMR technique at 380 K with different grain size of (1) less than 50, (2) 100-150 and (3) more than 150 μm. The polydispersity of the grain are shown by the slight steps on the curves[165].

Furthermore, the using of dopants or catalytic additives (alkali metals, alkaline earth metals and transition metals) has also demonstrated a destabilization effect[54,144,155,164]. Addition of alkali metal hydrides (LiH, NaH, KH and $LiAlH_4$) helped in accelerated hydrogen desorption rates at low temperature[54,155]. The dopants are expected to form "surface layers or islands of alanate that serve as 'windows' for hydrogen evolution from the decomposition AlH_3 (Fig. 4-5).

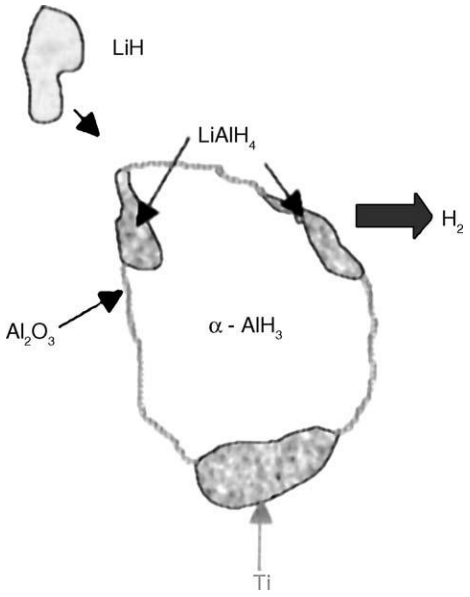

Figure 4- 5.Alanate phase particles ($LiAlH_4$) formed by ball milling of AlH_3 and LiH to produce H_2-transparent $LiAlH_4$ windows[155].

Significant room temperature decomposition was observed when adding Ti to LiH[155]. The effect of Ti on the decomposition kinetics are even pronounced when the dopants is added in solution (added as $TiCl_3$) during the AlH_3 synthesis[93]. Ti-catalyzed α-AlH_3 (~10 ppm) showed two kinetic enhancements compared to uncatalyzed α-AlH_3. Isothermal decomposition curves at temperature from 60°C to 192°C (Fig. 4-6) demonstrate that the first enhancement is a reduction in the induction period at the onset of decomposition (evident at higher temperatures). The second enhancement is an increase in the rate of hydrogen evolves (evident at lower temperatures).

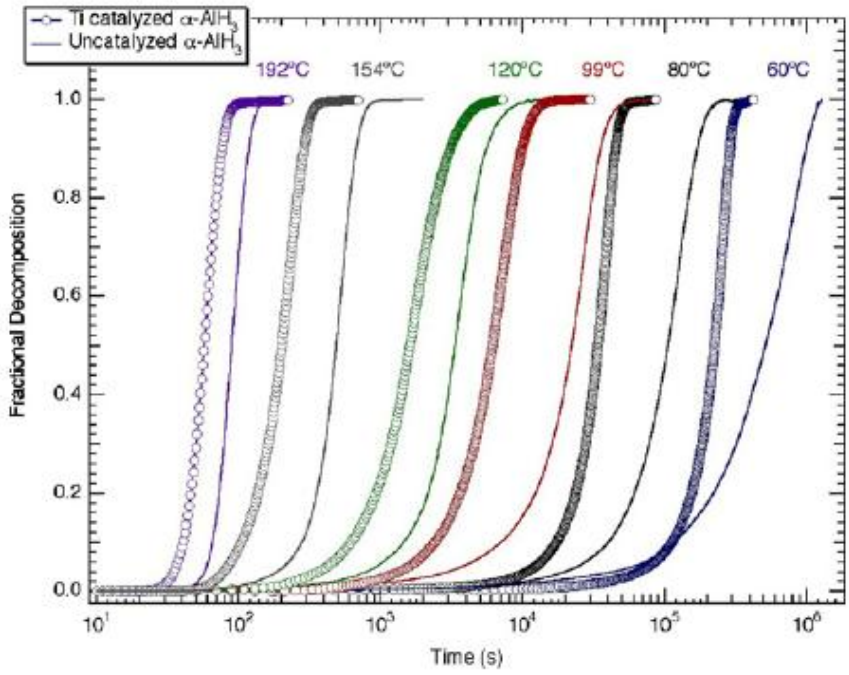

Figure 4- 6.Isothermal decomposition curves for catalyzed and uncatalyzed α-AlH_3[93].

Another studies reported that the thermal stability of AlH_3 and its decomposition activation energy are both highly dependent on the synthesis condition and sample purity. A post-synthesis thermal treatment has been shown to increase the desorption rate[157]. Other studies using light (irradiation) on AlH_3 resulted in the decrease in activation energy by 15 - 20% compare to non-irradiated "fresh" sample when exposed to visible light in just a few minutes[154,166].

4.3 Thermodynamics

AlH_3 decompose into Al metal and hydrogen gas. From this decomposition reaction, the thermodynamic properties of AlH_3 were determined either by experimental [102,158,160] or theoretical[167,168] methods. The thermodynamic properties are interrelated via equation (4.8)[76]

$$\Delta G = \Delta H - T\Delta S \quad \textbf{(4. 8)}$$

where ΔG is the Gibbs free energy of formation, ΔH is the formation enthalpy, T is the temperature (K) and ΔS is the entropy change. The entropy is associated with the transformation of hydrogen from a disordered gas to an ordered solid. The Gibbs free energy of formation at room temperature (G_{298K}) was determined by using the measured formation enthalpy (ΔH) and an entropy change(ΔS). Experimental measurement (by using calorimetry) determined the values of the formation enthalpy of AlH_3 by assuming the magnitude of the decomposition enthalpy is equivalent to the formation enthalpy with the only difference being a sign change[160]. The thermodynamic properties are summarized in Table 4-2.

Table 4- 2:Thermodynamic properties of AlH_3 phases summarized from various experimental and theoretical results.

Polymorph	ΔH $(kJ/mol\ AlH_3)$	ΔS $(J/molK)$	ΔG_{298K} $(kJ/mol\ AlH_3)$	Equilibrium pressure at 298K (GPa)
$\propto -AlH_3$	-9.9 ± 0.6[160]	130.7[160]	48.5 ± 0.6[160]	50[160] (fugacity)
	-11.4 ± 0.8[102]	-	46.5[102]	-
	-6.95[167]	-	-	-
	-12.35[168]	-	-	-
	-	-	-	10[169]
	-	-	-	0.1 - 1.0[170]
	-	-	-	~2[95]
$\beta - AlH_3$	-8.0 ± 1.0[160]	130.7[160]	50.5 ± 1.0[160]	-
$\delta - AlH_3$	-7.1 ± 1.0[160]	130.7[160]	51.4 ± 1.0[160]	-

Thermodynamics properties are expected to alter using nanoparticles compared with bulk materials[50,52,171,172]. This is because the energies (on molar basis) of both materials change in going from bulk materials to nanoparticles. For AlH_3, if the particle size decreases, the formation energy decreases (more negative) as shown in Fig. 4-7[50]. This theoretical study was performed using all electron density-functional total energy calculations. A significant decrease in the formation energy is predicted when the size is below 1 nm (critical particle size for AlH_3). This result suggests that the AlH_3 system becomes more thermodynamically stable when the particle size becomes smaller. Above this critical size, the formation energy is almost constant and similar to that of the bulk materials. This is because when the particles size is increased above the critical size, these nanoparticles contain core AlH_3 structural units which make them behave like a bulk material[50]. Another theoretical study using the Wulff construction[52] reported that if the AlH_3 particle size decreases, the transition temperature increases as shown in Fig. 4-8. It would be useful to increase the transition temperature (or equivalently, the heat of reaction) because at equilibrium, AlH_3 decomposes at temperature that is too low for practical applications. However this effect is extremely small, increasing T_{eq} by only 13 K for the extreme case of a metal nanoparticle 1 nm in radius.

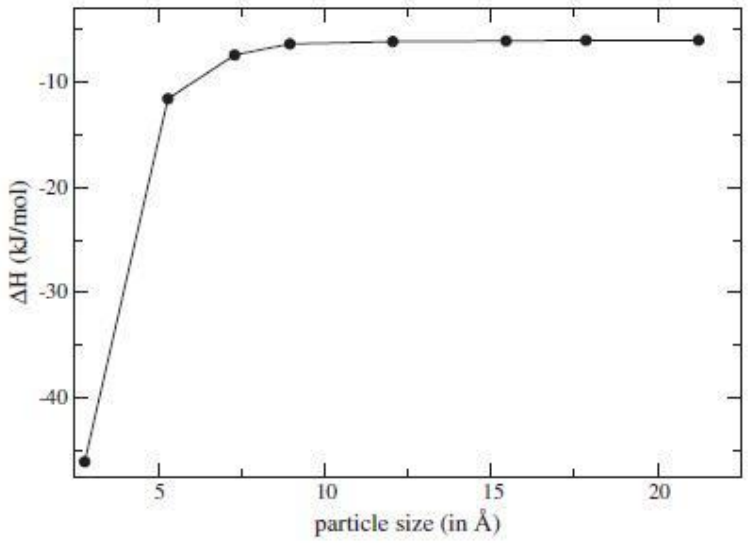

Figure 4- 7.Calculated formation energy as a function of particle size for the AlH_3 nanoparticles[50].

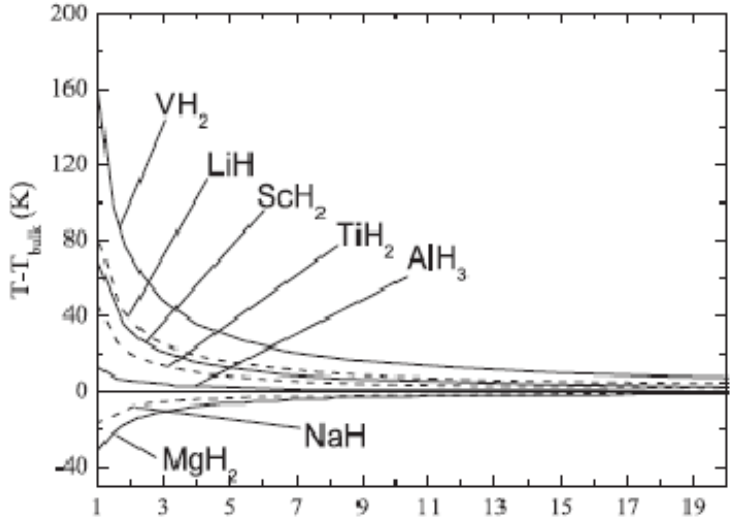

Figure 4- 8.The variation in the metal/metal hydride transition temperature relative to the result for a bulk material[52].

4.4 High pressure studies

Synthesis of α-AlH_3 from the elements is possible under high pressures according to equation (4.9)

$$\mathbf{AlH_3(s) \leftrightarrow Al(s) + \frac{3}{2}H_2(g)} \qquad \textbf{(4. 9)}$$

The pressure, temperature-state diagram of the AlH_3 system are constructed using results from inelastic neutron scattering (INS) experiments[93] and then the calculated equilibrium values are compared with various experimental values[95,170,173,174] as shown in Fig. 4-9. The calculated equilibrium line predicts consistently lower temperatures then the early experimental results[95,170,173]. This is due to an oxide layer at the AlH_3 surface which is virtually impermeable to hydrogen. On the other hand, the experimental result using non-oxidised Al particles showed points corresponding to the formation of α-AlH_3, which are closest to the calculated line[174]. For this experiment, the minimum hydrogen pressure necessary for the formation of α-AlH_3 is about 20 kbar at temperatures 50 - 100°C.

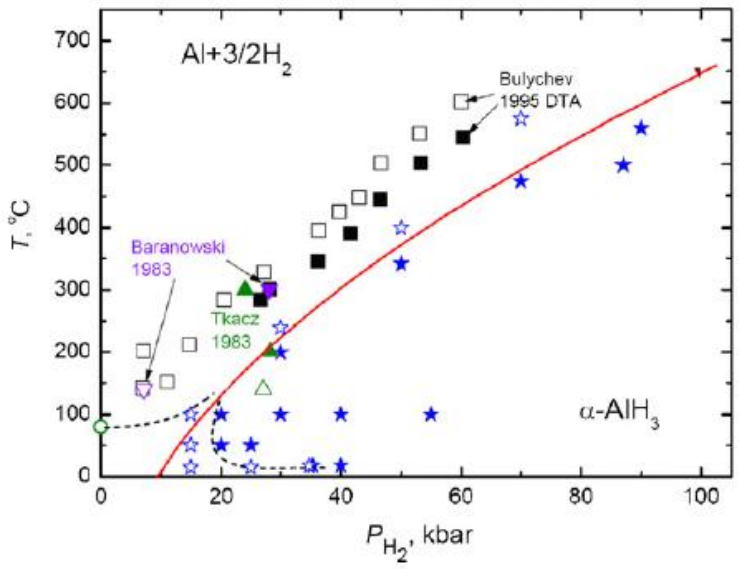

Figure 4- 9.Calculated equilibrium line for $AlH_3(s) \leftrightarrow Al(s)\frac{3}{2}H_2(g)$ (red line) are compared with the results from various experimental studies on the formation and decomposition of $\alpha - AlH_3$ under high hydrogen pressure[93]. The markers indicate the presence (filled) or absence (unfilled) of α-AlH_3 in the samples. Decomposition points from Tkacz et al. (triangles)[173], Baranowski (upside down triangles)[170] and Bulychev (squares)[95] are for AlH_3 powders stabilised by a surface oxide layer. Results from Sakharov (stars)[174] were obtained using non-oxidized Al powder as the starting material.

A recent theoretical study showed that hydrogen absorption into bulk Al may be thermodynamically favourable at low temperatures where very low hydrogen equilibrium pressures are expected (50 bar at 77 K)[175]. Another theoretical study represented a pressure-temperature calculated plot of the Al-H system as shown in Fig. 4-10. From this figure it is seen that Al should be able to hydride under ~3 kbar at 0°C [176]. However at this range of temperatures both the absorption kinetics and hydrogen dissociation ability will be hindered. This means that low temperature H_2 absorption into pure Al is extremely slow and near undetectable[91].

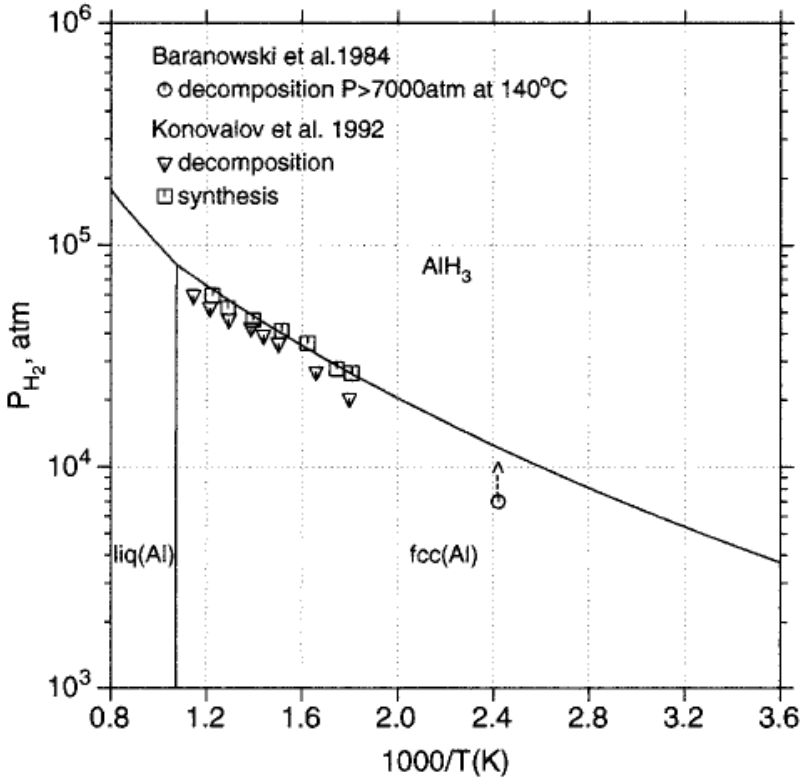

Figure 4- 10.Plot pressure-temperature diagram of the Al-H system where the phase boundary between AlH_3 and fcc (Al) represents the dissociation pressure of AlH_3 in comparison with experimental data (symbol - O).

4.5 Results and discussions

The mechanochemical reactions of the $3LiAlH_4 + AlCl_3 \rightarrow 4AlH_3 + 3LiCl$ proceeded to completion through the reduction of $LiAlH_4$ with $AlCl_3$ to formed AlH_3 nanoparticles as the reaction products. These AlH_3 nanoparticles were embedded within a buffer (LiCl) matrix. The LiCl was not removed through washing with a nitromethane/$AlCl_3$ solution because they reacted with AlH_3 nanoparticles and the reaction caused a ~50% reduction in the H_2 content of the sample[143]. In order to understand the effect of buffer quantity on the particle size distribution and agglomeration, AlH_3 samples were synthesized via milling conditions as outlined in Table 4-3. It was expected that larger AlH_3 particles

would be formed using low levels of buffer and smaller AlH_3 particles would be formed in samples with high buffer.

Table 4- 3:Overview of AlH_3 samples synthesis at 77 K details.

Sample	Rod to powder ratio	Milling time (min)	LiCl buffer (g)	Product volume ratio (LiCl:AlH_3)
A	32:1	30	0	0.76:1
B	32:1	30	0.46	2:1
C	32:1	30	0.74	5:1
D	32:1	30	0.86	10:1
E	32:1	60	0.46	2:1

In order to understand the cryogenic synthesis, samples were first milled for 30 minutes (sample B) and 60 minutes (sample E) by using LiCl buffer (2:1 LiCl:AlH_3 volume ratio) respectively. Fig. 4-11 shows the XRD patterns of the synthesized AlH_3 before desorption reactions. Both samples consist of peaks related to α-AlH_3, α'-AlH_3 and LiCl. Sample B contains α-AlH_3 and α'-AlH_3phases in a similar ratio. A decrease in α'-AlH_3 content and a new peak related to Al were observed in the pattern of sample E. This shows that decomposition of AlH_3 to Al and H_2 has occurred during the milling process when the milling time was increased from 30 to 60 minutes.

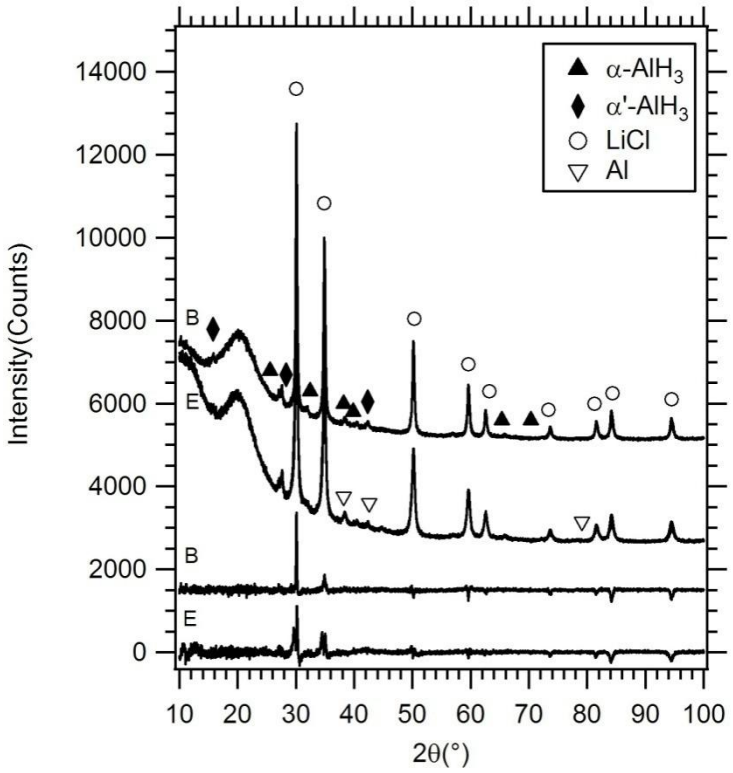

Figure 4- 11.XRD patterns of synthesized AlH_3 milled for 30 minutes (sample B) and 60 minutes (sample E) by using 2:1 LiCl:AlH_3 volume ratio respectively before the desorption process.

Mechanochemical reactions of the $3LiAlH_4 + AlCl_3 \rightarrow 4AlH_3 + 3LiCl$ are moderately exothermic (ΔH=-213 kJ/mol), it provides more than enough energy for AlH_3 to decompose to Al and H_2 due to the low amount of energy required for decomposition (ΔH=+11.4 kJ/mol)[39]. At the same time, the milling process provides collision energy due to collision between reactant particles and balls inside the mill[57]. Therefore the overall energy is generated from both the mechanochemical reaction and from the milling process itself. The addition of LiCl as a buffer, decreases the overall energy generation and lowers the reaction rate during mechanochemical reaction[57,60]. This is because during the mechanochemical reaction, the transferred energy into the reactant particles is reduced due to the presence of the buffer phase which absorbs some of the collision energy and heat energy[57]. As a result, no decomposition of AlH_3 to Al and H_2 is observed when the sample was milled for 30 minutes using LiCl buffer (2:1 LiCl:AlH_3 volume ratio).

However when the milling time was increased to 60 minutes, the total number of impacts will increase (produce high energy milling), which enables the AlH_3 phase transformation into α'-AlH_3 and enables AlH_3 decomposition into Al and H_2.

The AlH_3 and LiCl crystallite sizes were reduced when milling times increased from 30 minutes to 60 minutes (Table 4-5). During milling, deformation, fracture and welding of reactant particles occur repeatedly[58,131]. Plastic deformation of the reactant particles initially occurs by reactant particles decomposing into sub-grains[58,131]. After further milling, the sub-grains size decreases and nanometer size sub-grains are produced within each reactant particle[58,131]. So the reaction product will inherit the nanoscale microstructure of the reactant particles[58,63,131]. Upon increasing milling time, the total number of impacts will increase. Hence the reactant particles are subjected to higher mechanical induced energy, which results in particles decomposing into smaller sizes.

Based on these results in order to produce nanoparticles of AlH_3 30 minutes milling time is preferred as a milling parameter for further investigation to limit the Al content of the samples but also allow for complete AlH_3 formation from reactants. Samples were cryogenically milled for 30 minutes with different LiCl:AlH_3 volume ratios of 2:1 (Sample B), 5:1 (Sample C) and 10:1 (Sample D) respectively. The addition of LiCl as a buffer restricts AlH_3 decomposition, prevents high Al yields and promotes AlH_3 nanoparticle formation.

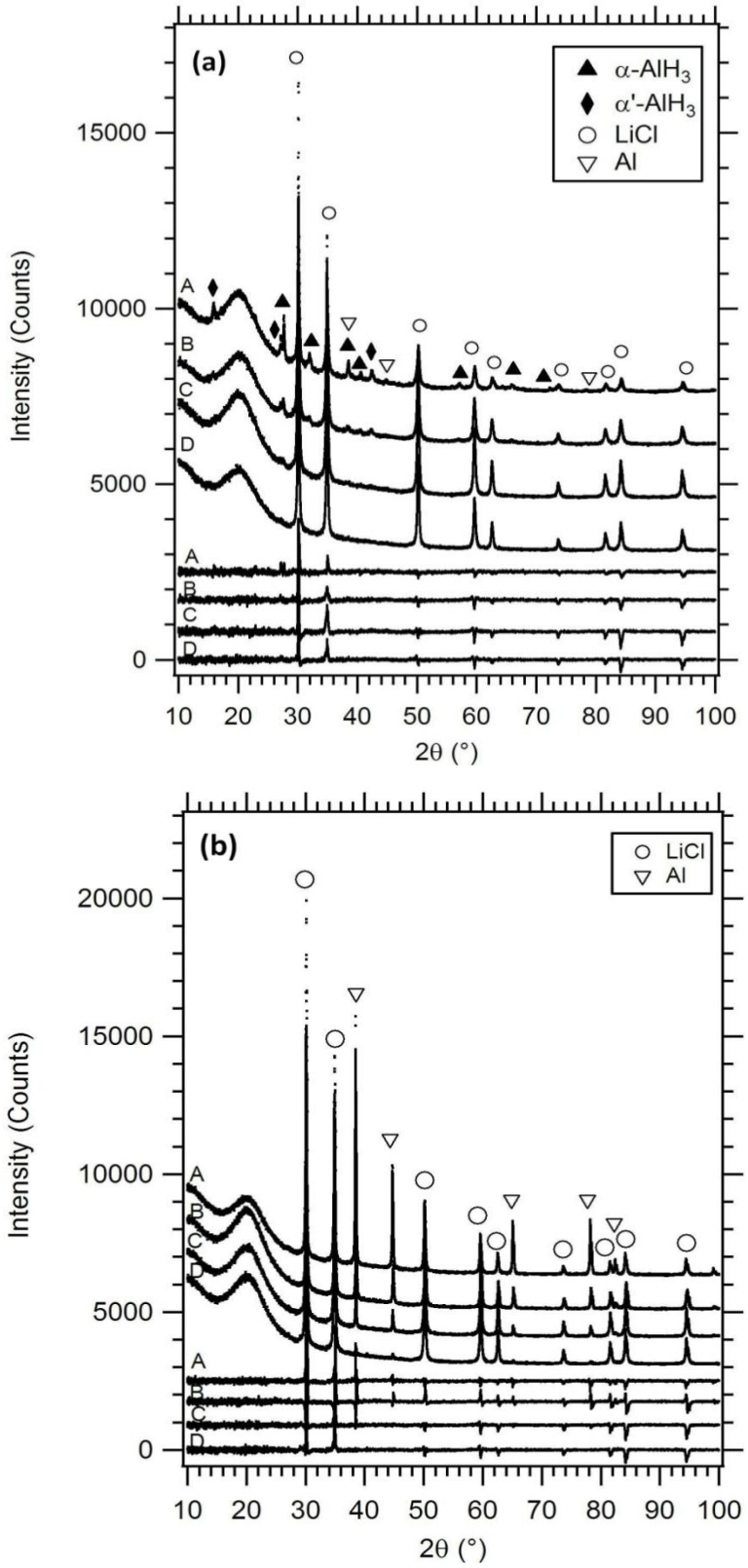

Figure 4- 12.XRD patterns of synthesized AlH_3 (a)before and (b)after the desorption process.

Fig. 4-12 shows the XRD patterns of the synthesized AlH_3 before and after desorption reactions. Before desorption, Al peaks were not detected in all samples with buffer (Fig. 4-12a samples B, C and D). The α'-AlH_3 peaks were not detected in sample C (Fig. 4-12a) and both α-AlH_3 and α'-AlH_3 peaks were not detected in sample D (Fig. 4-12a). After desorption (Fig. 4-12b), only Al and LiCl peaks were detected in all samples. No other peaks are evident in the samples before and after desorption, which suggest that the reaction was completed.

Based on quantitative phase analysis (QPA) provided in Table 4-5, the crystalline wt.% of LiCl from Rietveld analysis before and after desorption are different from those calculated from expected yields. Rietveld analysis calculated wt.% values by assuming a sample content is 100% crystalline. For these AlH_3 samples, expected LiCl yields before desorption should result in 51.4 wt.%, 73.5wt.%, 87.4 wt.% and 93.2 wt.% LiCl for sample A, B, C and D. However Rietveld results show crystalline LiCl consists of 60.1 ± 0.5 wt.%, 84.9 ± 0.6 wt.%, 96.5 ± 0.6 wt.% and 100 wt.% respectively. Due to the fact that the crystalline LiCl content is larger from Rietveld analysis than the expected yields, an amorphous or poorly crystalline AlH_3/Al phases may be formed during the mechanochemical reaction. After heating the samples from room temperature to 150°C during desorption process, the appearance of diffraction peaks corresponding to Al were observed. This explains why AlH_3/Al peaks were not evident in sample C and D before the desorption process. They could also just be really broad due to their nanocrystalline nature and unobservable due to the low wt.% in the sample. This result is also consistent with a previous study of the synthesis of Y_2O_3 using the mechanochemical method, where no peaks corresponding to any yttrium phases were evident in the as-milled sample[146]. Heating of the washed sample resulted in the appearance of broadened diffraction peaks corresponding to Y_2O_3.

Table 4- 4:Rietveld results for phase composition calculated from XRD patterns in Figure 4-12. Mathematical fitting uncertainties are provided (2 standard deviations).

Sample	Phase composition before desorption (wt.%)				Phase composition after (wt.%)	
	α-AlH_3	α'-AlH_3	Al	LiCl	Al	LiCl
A	15.7 ±0.4	20.8 ±0.4	3.3 ± 0.2	60.1 ± 0.5	45.7 ± 0.1	54.2 ± 0.1
B	7.4 ± 0.4	7.6 ± 0.5	-	84.9 ± 0.6	24.4 ± 0.3	75.5 ± 0.3
C	3.4 ± 0.6	-	-	96.5 ± 0.6	8.8 ± 0.1	91.1 ± 0.1
D	-	-	-	100	1.9 ± 0.1	98.0 ± 0.1
E	7.2 ± 0.4	3.6 ± 0.4	3.3 ± 0.3	85.7 ± 0.6	24.4 ± 0.3	75.5 ± 0.3

AlH_3 crystallite sizes decreased from 24.4 ± 1.3 nm (sample A), 15.0 ± 1.4 nm (sample B) and 8.7 ± 2.3 nm (sample C), for samples synthesised without using buffer and samples using LiCl:AlH_3 volume ratios of 2:1, 5:1 and 10:1 respectively (Table 4-5). However LiCl and Al crystallite sizes increase after the desorption process.

The addition of LiCl buffer led to a reduction of the synthesized AlH_3 crystallite size. In lower buffer content, the specific surface area of smaller particles are higher which provides higher driving force for particle coalescing and decreases their surface energy [57,60]. On the other hand, because the volume fraction of the buffer phase is low, it cannot restrain the particle growth and agglomeration of the crystallites[57,60]. However in higher buffer content, the volume fraction of the buffer phase is sufficient to prevent particle agglomeration during the mechanochemical reaction by physical separation of the nanoparticles and therefore controls the particle size distribution[57,60].

During desorption, all samples were heated from room temperature to 150°C. As a result, the crystallites grow (due to both intra-particle crystallite growth and inter-particle agglomeration), and this growth increases rapidly with increasing temperature. The present result is similar to results reported elsewhere. Kobayashi et. *al.* indicated that the SnO crystallite size increased by heating at 450°C to 500°C[177]. Huaming et. *al.* reported that the SnO particle size increased from 25 to 40 nm when heating from 450°C to 800°C[178]. Weiqin et *al.* showed that the crystal size increased from 18 to 36 nm when the heat-treatment temperature increased from 400°C to 800°C for zinc oxide material[179].

Table 4- 5:Rietveld results for crystallite size calculated from XRD patterns in Figure 4-12. Mathematical fitting uncertainties are provided (2 standard deviations).

Sample	Crystallite size before desorption (nm)				Crystallite size after desorption (nm)	
	α-AlH_3	α'-AlH_3	Al	LiCl	Al	LiCl
A	24.4 ± 1.3	19.9 ± 1.2	26.3 ± 3.9	18.2 ± 0.2	61.0 ±0.7	35.2 ± 0.3
B	15.0 ± 1.4	14.3 ± 2.2	-	21.1 ± 0.1	41.5 ±1.5	35.9 ± 0.5
C	8.72 ± 2.3	-	-	25.6 ± 0.2	54.8 ± 2.8	34.9 ± 0.3
D	-	-	-	27.2 ± 0.2	71.0 ± 4.8	32.3 ± 0.2
E	14.9 ± 1.4	18.1 ± 5.1	7.5 ± 1.0	12.3 ± 0.1	31.9 ± 1.1	26.1 ± 0.4

XRD has provided good information about the average crystallite size but TEM was performed to determine the real particle size. Fig. 4-13 shows TEM images of synthesized AlH_3 before (a, c, e, g) and after (b, d, f, h) the desorption process. The TEM images show that the sample primarily consisted of smaller AlH_3/Al particles embedded within larger aggregates of LiCl buffer. Synthesized AlH_3 without using buffer (sample A)

comprised of 5 - 64 nm particle size range. This size ranges tend to decrease when using LiCl:AlH_3 volume ratios of 2:1 (sample B) to 10:1 (sample D). The particle size range for sample B, C and D are 6 - 26 nm, 15 - 37 nm and 11 - 29 nm respectively (Table 4-6). It should be noted that there is a slight discrepancy between particle size and crystallite size determined by TEM and XRD which suggest moderate particle agglomeration occurs within the samples. It becomes difficult to observe AlH_3/Al particles in the samples when the LiCl:AlH_3 volume ratio was increased from 2:1 to 10:1. This is because LiCl is a major volume fraction of these samples (~ 90%) so it is difficult to identify particles of the minor product phases (AlH_3 and Al).

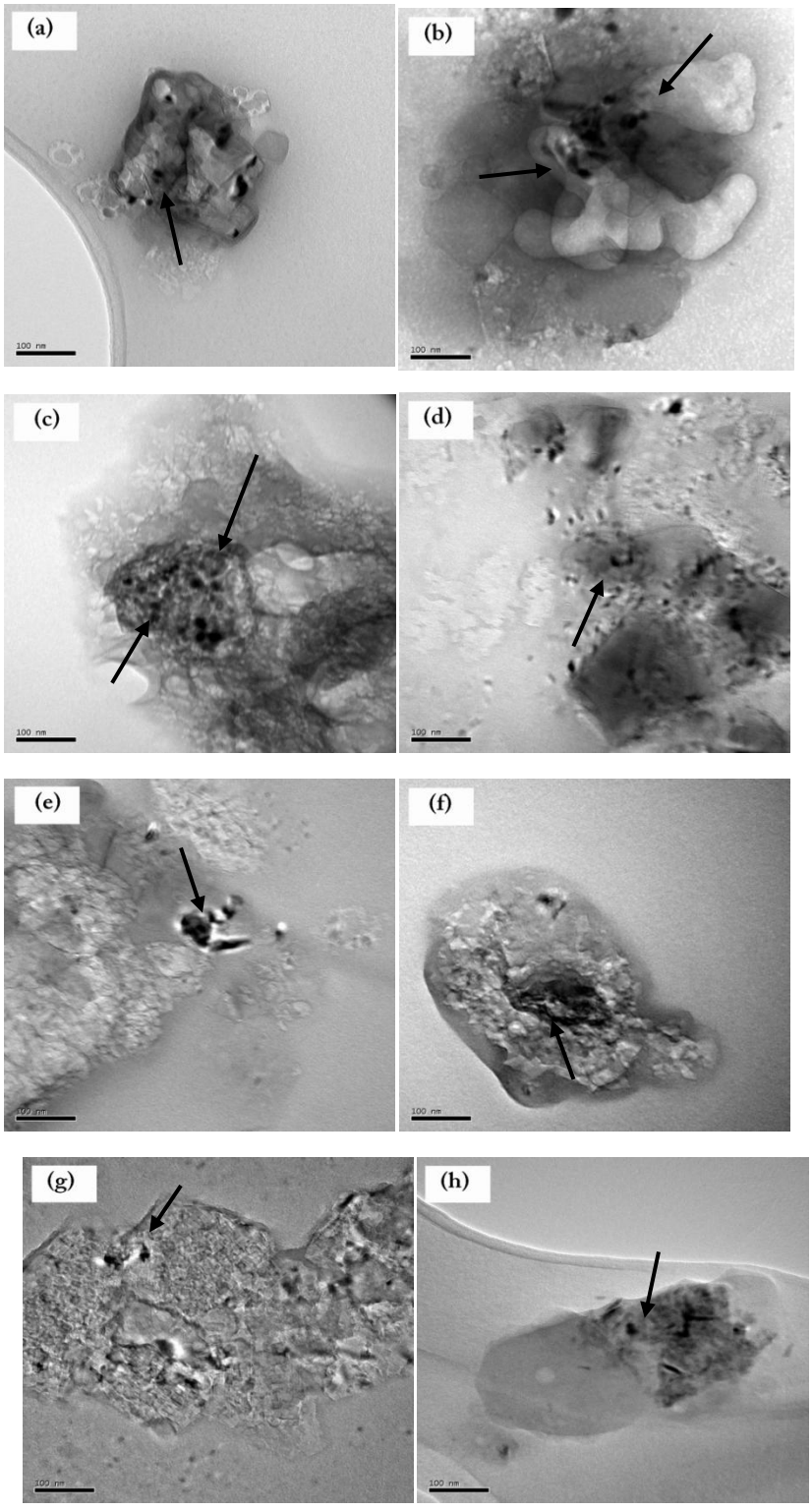

Figure 4- 13.TEM images of sample before desorption: (a) sample A, (c) sample B, (e) sample C and (g) sample D and after desorption: (b) sample A, (d) sample B and (f) sample C and (h) sample D. (AlH_3 nanoparticles embedded within a LiCl buffer shown by the black arrow)

Table 4- 6:Particle size of synthesized AlH_3/Al before and after desorption process from TEM measurements.

Sample	Particle size (nm)	
	Before desorption	After desorption
A	5 - 64	19 - 71
B	6 - 26	10 - 41
C	15 - 37	21 - 50
D	11 - 29	15 - 78

EDS data as provided in Fig. 4-14 verifies the presence of high quantities of Al and low quantities of Cl in all samples. However Hydrogen cannot be detected using EDS therefore AlH_3 and Al cannot be differentiated. Lithium also cannot be detected using EDS. EDS showed the existence of O for all samples, a result of TEM sample air exposure. Si and C come from TEM grid.

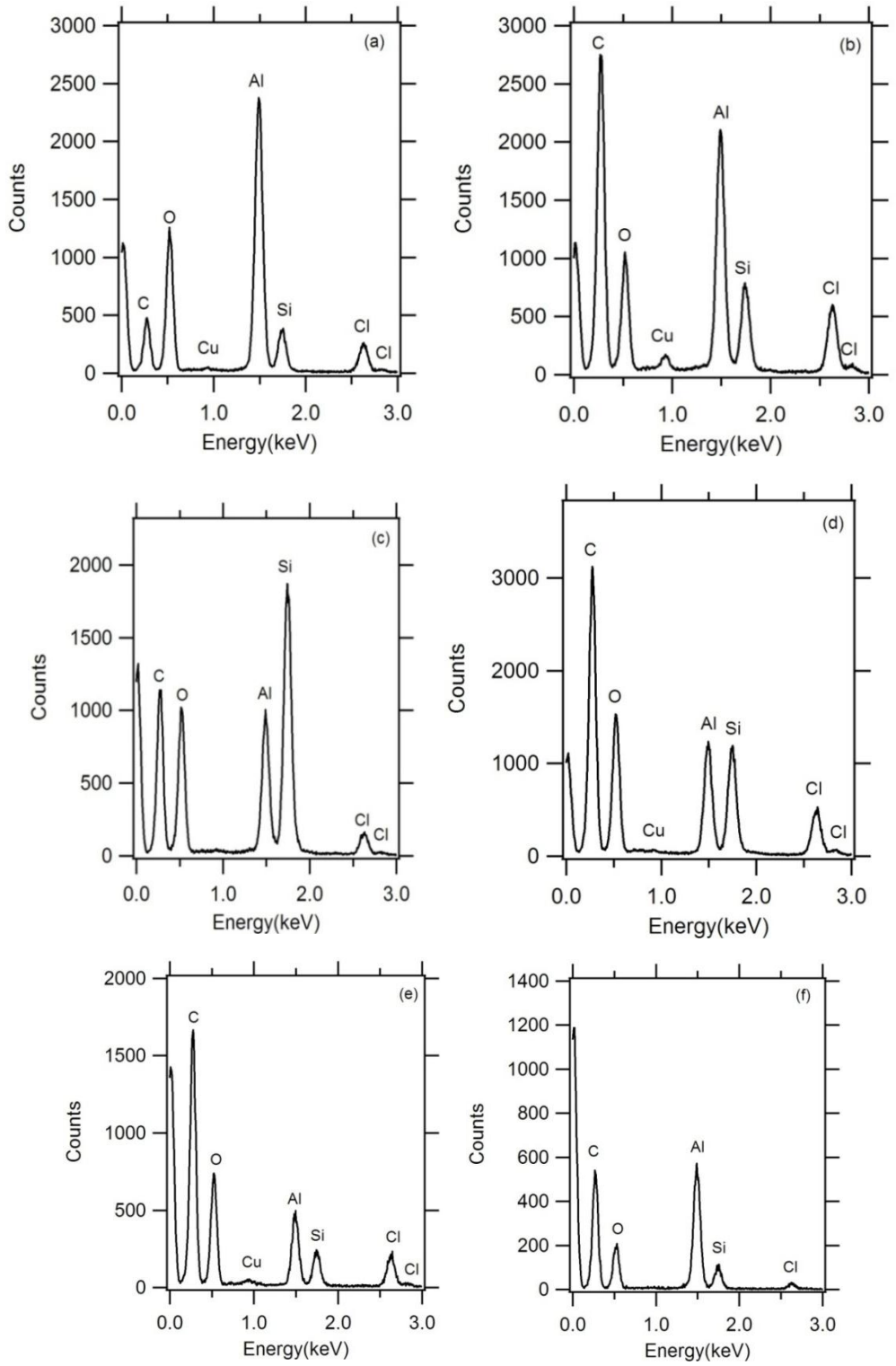

Figure 4- 14.EDS spectra from TEM investigations of sample before desorption: (a) sample B, (c) sample C, (e) sample D and after desorption: (b) sample B, (d) sample C and (f) sample D.

Hydrogen desorption measurements were undertaken within 1 week of sample synthesis to ensure room temperature AlH_3 decomposition was minimised except for sample A where the experiment was undertaken after 2 weeks of sample synthesis. Fig. 4-15 shows the effects of without using LiCl buffer (sample A) and using LiCl:AlH_3 volume ratios of 2:1 (sample B), 5:1 (sample C) and 10:1 (sample D) on the AlH_3hydrogen desorption curves. The AlH_3 desorption curves display the wt.% of hydrogen as a function time in the calculated non-salt portions of the synthesized samples. The percentage of AlH_3 portions calculated in the samples when sample A, B, C and D were 48.5%, 26.4%, 12.5% and 6.7% respectively. Despite the XRD pattern showing only a very minor AlH_3 crystalline phase, the desorption results indicate that H_2 did evolve from these samples. Therefore AlH_3 may form as an amorphous or poorly crystalline phase within the synthesized samples.

Sample B and C desorbs 2.65 wt.% and 2.48 wt.% H_2 (from the Al portion of the sample) over 24 hours at 50°C. This H_2 desorbed wt.% decrease to 1.5 wt.% and 0.42 wt.% for sample A and D. It is clear that particle size reduction when ball milling using buffer does effectively increase the H desorption rate compare to bulk[180,181]. Another study also shown that α-AlH_3 of 50 μm crystallites exhibit H_2 evolution rate more than two orders of magnitude slower than α-AlH_3 with fine crystallites (0.1 μm)[175]. A reduction in AlH_3 particle size gives an increase in the kinetics of desorption[54]. Smaller particles produced from ball milling will have higher surface areas. These high surface areas enhance the accessibility of the particle to penetrate and release the hydrogen. Milling also creates a specific state of the surface possibly with special surface defects and imperfections [181,182]. Additionally, the combination of these smaller particle sizes and defects results in a decrease of the thermal stability of AlH_3 kinetic decomposition[141]. All these factors promote hydrogen desorption, which is consistent with previous research[41,182-184]. However slow kinetics desorption were detected when using 10:1 LiCl:AlH_3 volume ratio (sample D). Upon increasing the quantity of buffer, the AlH_3 particles are surrounded by

a higher amount of LiCl. This LiCl tends to cover the surface of AlH_3 particles and hinder hydrogen accessibility leading to a decrease in the rate of hydrogen desorption.

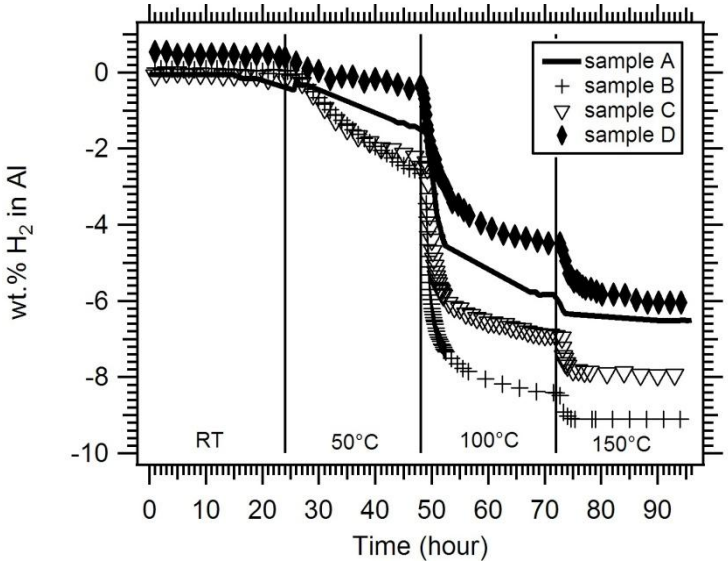

Figure 4- 15.Hydrogen desorption data from AlH_3 samples. The H_2 wt.% is given as a percentage of the calculated non-salt portion of the samples.

Rapid desorption was observed when the desorption temperature increased to 100°C and further increasing the temperature to 150°C results in complete hydrogen desorption. The maximum H_2 wt.% for sample A, B, C and D were 6.5 wt.%, 9.09 wt.%, 7.97 wt.% and 5.97 wt.% respectively.

The reason for the different maximum H_2 wt.% is not fully understood. It is possible that an incomplete AlH_3 synthesis reaction occurs in samples with higher buffer content. Upon increasing the buffer content, the buffer phase tends to cover the surface of the reactant particles and hinder further reaction, reducing the reaction volume among the reactant particles, leading to a decrease in the rate of reaction[57]. An incomplete reaction would result in $LiAlH_4$ phase within the sample which has been shown to decompose at temperatures greater than 100°C and when milled with $AlCl_3$ and/or $TiCl_3$ additives has been shown to decompose at room temperature[185]. However the XRD result provided in

Fig. 4-12 does not show any evidence of this starting reagent. In addition, no $LiAlH_4$ decomposition products (Li_3AlH_6, LiH or LiAlH) exist in the XRD pattern or any other that has been performed before and after desorption process at 25°C, 50°C, 100°C and 150°C.

In order to confirm this, a new sample using high LiCl:AlH_3 volume ratio of 10:1 (sample F) was milled for 60 minutes. Results from XRD (Fig. 4-16) and hydrogen desorption measurements (Fig. 4-17) were compared between sample milled for 30 minutes (sample D) and 60 minutes (sample F). Increasing the milling time to 60 minutes results only a tiny peak related to AlH_3 in the as-milled sample. After the desorption measurement, only peaks related to Al and LiCl were observed. No starting reagents and no $LiAlH_4$ decomposition products were detected in the XRD pattern of sample milled for 60 minutes before and after desorption process at 25°C, 50°C, 100°C and 150°C. This result is consistent with sample milled for 30 minutes. Despite the XRD pattern showing only a minor AlH_3 crystalline phase 5.97 wt.% and 6.8 wt.% H_2 were desorbed from the non-salt portion of both samples. These H_2 wt.% were higher than H_2 wt.% reported for $LiAlH_4$. Only 4 wt.% H_2 was released from $LiAlH_4$ at 148°C[186]. Based on these results, it is likely that an amorphous or poorly crystalline phase of AlH_3 was formed within the synthesized samples rather than incomplete AlH_3 reaction in sample with high buffer content.

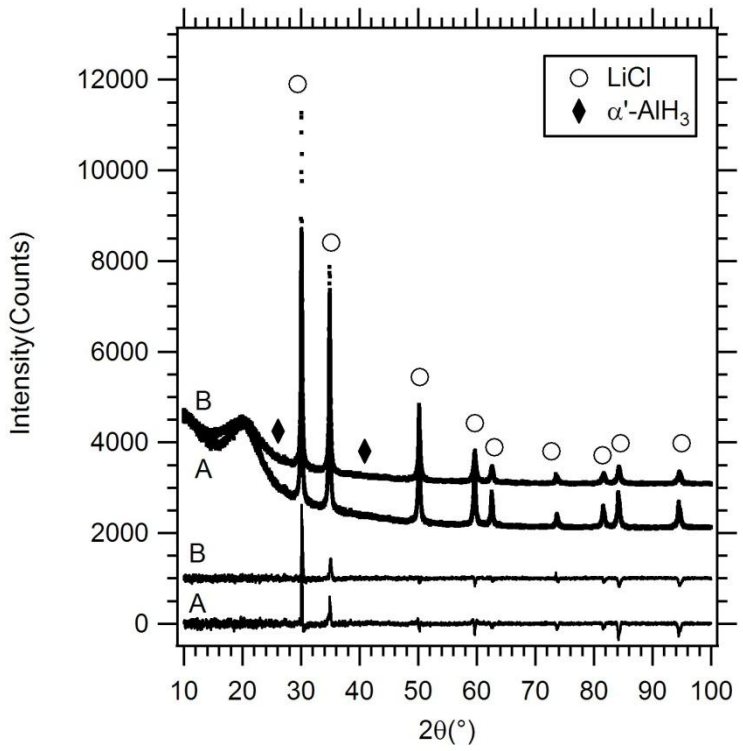

Figure 4- 16.XRD patterns of synthesized AlH_3 using 10:1 LiCl:AlH_3 volume ratio milling for A (30 minutes) and B (1 hour).

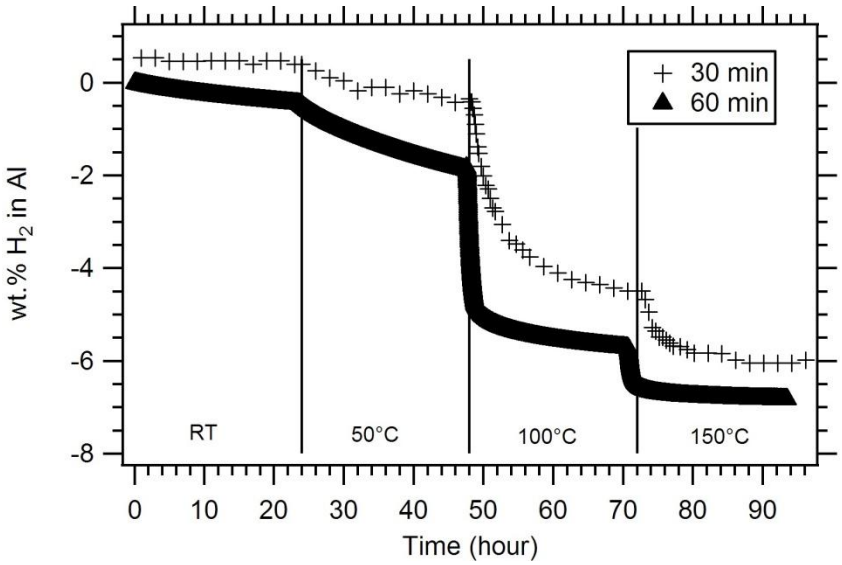

Figure 4- 17.Hydrogen desorption data from synthesized AlH_3 using 10:1 LiCl:AlH_3 volume ratio. The H_2 wt.% is given as a percentage of the calculated non-salt portion of the samples.

Another study showed that the reduction in maximum H_2 wt.% is due to a portion of the hydrogen remaining trapped inside the particles when the diffusion of hydrogen through the particles or nucleation of aluminium sites is slow during AlH_3 decomposition process[161]. A study using proton NMR spectrum of AlH_3 showed a sharp NMR line, from temperatures 423 K to below 11 K. This proved that H_2 either as isolated molecules or very small nano-cluster must be physically trapped in the material, possibly in cavity surfaces that were formed during the slow AlH_3 decomposition process[187].

Hydrogen absorption measurements were performed on the Al product formed from the fully decomposition of AlH_3 by heating at 150°C for 24 hours. By forming Al via AlH_3 decomposition, the subsequent hydrogenation was performed on oxide-free Al particles. Samples underwent hydrogen pressures of 280 bar at -196°C, 1420 bar at 25°C, 1532 bar at 50°C, 1734 bar at 100°C and 1967 bar at 150°C with no measureable hydrogen absorption.

The thermodynamics of hydrogen absorption and desorption are reported to be altered when using nanoparticles instead of bulk materials[50,52,171,172]. For the AlH_3 system, significant thermodynamic changes are theoretically predicted for AlH_3 nanoparticles smaller than its critical particle size (1 nm) [50,52]. The formation enthalpy (ΔH) value for 1 nm size is reported to be -5.8 kJ/mol, which is similar to that in the bulk AlH_3 system (-5.99 kJ/mol). These nanoparticles have core AlH_3 structural units which make them behave like a bulk AlH_3 system (the system is thermodynamically unstable). Below this critical particle size, the AlH_3system becomes thermodynamically stable. Changes in ΔS with particles size also has a big impact on ΔG, therefore this should be taken into account. However, these changes in ΔS are not usually considered in the theoretical studies. Therefore changes in either the reaction ΔH and ΔS due to particle size may actually shows a larger effect on the thermodynamics properties. This has been pointed out in experimental studies on MgH_2 nanoparticles[53]. Based on the thermodynamics of the 1 nm Al-AlH_3 system, hydrogen absorption into nano Al requires lowers pressure and

temperature. However, recent theoretical investigations indicate that hydrogen absorption into bulk Al may be thermodynamically favourable at cryogenic temperatures where very low equilibrium pressures are predicted (50 bar at -196°C)[175]. If the predicted pressure of 50 bar at a temperature -196°C is correct and compared to the hydrogen absorption measurement attempt herein (280 bar at -196°C), then other factors must be favourable for hydrogen absorption in bulk Al (in this case 10 - 30 nm) at the pressure and temperature studied, given no hydrogen absorption were detected during this measurement. This result is also consistent with the previous study using 1875 bar at -196°C, with no hydrogen absorption measurement, even for 30 - 50 nm particle size[96].

4.6 Conclusions

Synthesis of AlH_3 by using mechanochemical reactions of the $3LiAlH_4 + AlCl_3$ with different LiCl:AlH_3 volume ratios at 77 K has been studied. The addition of LiCl as a buffer leads to the reduction of the synthesized AlH_3 crystallite size, restricting AlH_3 decomposition and preventing high Al yields. Quantitative Rietveld results coupled with hydrogen desorption measurements suggest the presence of an amorphous AlH_3 phase in mechanochemically synthesized samples, which deserves further study to identify its structural properties. TEM results show that the synthesized AlH_3 comprised of 10 - 30 nm particle size range. For the hydrogen desorption measurements, it is clear that AlH_3 particle size reduction when ball milling using buffer does effectively increase the H desorption rate compared to the case without using buffer. For hydrogen absorption measurements, decomposed AlH_3 nanoparticles with 10 - 30 nm in size underwent pressures of 280 bar at -196°C, 1420 bar at 25°C, 1532 bar at 50°C, 1734 bar at 100°C and 1967 bar at 150°C with no measurable hydrogen absorption.

4.7 Future work

AlH_3 nanoparticles must be synthesised < 10 nm in order to allow hydrogen sorption reversibility at pressures significantly lower than for bulk AlH_3. Results herein suggest the formation of an amorphous AlH_3 phase upon milling under certain conditions. The analysis and properties of this amorphous AlH_3 phase is important in order to understand the bonding relationship between hydrogen and Al. It is possible that different thermodynamics exist for an amorphous Al-H system that would result in an altered sorption pressure relationship. Amorphous AlH_3 has not been reported in the literature to date, hence the need to analyze its structure, bonding, and thermodynamic properties.

CHAPTER 5: Titanium manganese alloy

5.1 Introduction

Much research has been undertaken to investigate the hydrogen storage properties of various types of metal hydride families such as Mg-based systems, BCC alloys and intermetallic systems (AB, AB_2 (Laves phase), AB_3 and AB_5)[9,10,34]. Intermetallic systems often consist of a stable hydride forming element with an element forming a nonstable hydride.

For AB_2, the systems are based on two Laves phases' crystal structures. The crystal structures can be hexagonal, C14 ($MgZn_2$ type) or cubic, C15 ($MgCu_2$ type) [9,34]. In these systems the A elements are usually Ti, Zr, Hf, Th or a lanthanide, whilst the B elements can be a variety of transition and non-transition metals.

5.1.1 Properties

Among the intermetallic systems for hydrogen storage, $TiMn_2$ based Laves phase alloys have attracted attention due to their easy activation, modest hydrogen sorption temperature, rapid kinetics and low cost[188,189]. The hydrogen storage capacity of $TiMn_2$ alloys is reasonably modest compared to other metal hydrides but is higher than 1.0 H/M (hydrogen per metal formula unit)[190,191] making it suitable for many static hydrogen storage applications. If weight is not an issue, then there are two main factors to consider, the cost of the hydride, and its long term stability (cycling properties). The $Ti_{0.97}Zr_{0.019}V_{0.439}Fe_{0.097}Cr_{0.045}Al_{0.026}Mn_{1.5}$ alloy contains relatively inexpensive elements, with the exception of vanadium, however ferro-vanadium (V with Fe impurity) is an order of magnitude less expensive than pure vanadium. Thus, having a hydrogen storage alloy with V and Fe components allows for a reduced system cost[10,34]. The addition of

elemental additives to the $TiMn_2$ system is required to enhance its hydrogenation and dehydrogenation cycling properties for long term use[192]. There are other problems with Ti-Mn alloys including their comparatively high equilibrium plateau pressure (between 0.8 MPa and 1.2 MPa) under near ambient temperatures and the fact that these alloys possess a large sorption pressure hysteresis effect [190,193] during hydrogen cycling. In order to reduce these disadvantages, research has been undertaken on altering $TiMn_2$ alloys by partial substitution of Ti or/and Mn with other elements [193-196], by using different $TiMn_2$ composition/stoichiometries[190,197] or through catalysed $TiMn_2$ alloys [198,199].

5.1.1.1 Different $TiMn_2$alloy compositions/stoichiometries.

Ti-Mn binary alloys whose Ti contents were less than 36 at.% absorbed almost no hydrogen ($P \leq 4.5$ MPa), but the alloys containing more Ti react easily and rapidly with hydrogen at room temperature without any activation treatment and complete the hydriding reaction in a short time[190]. The $TiMn_{1.5}$ hydride shows the most desirable properties of all the Ti-Mn binary alloy hydrides as shown in Fig. 5-1[190]. The dissociation plateau pressure is reported to be 0.7 MPa, the maximum amount of absorbed hydrogen is 228 mlg^{-1}, the maximum amount of released hydrogen is 190 mlg^{-1} at 20°C and ΔH=-28.7 $kJ(mol\ H_2)^{-1}$.

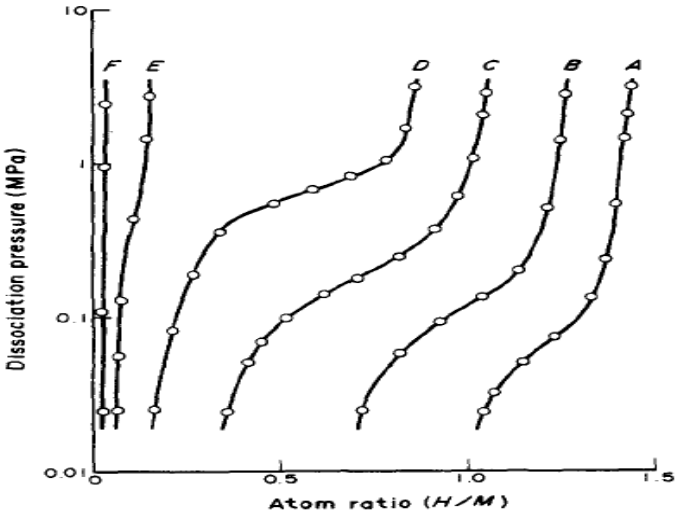

Figure 5- 1.Pressure-composition desorption isotherms of various Ti-Mn compositions: (A) $TiMn_{0.75}$; (B) $TiMn_{1.0}$; (C) $TiMn_{1.25}$; (D) $TiMn_{1.5}$; (E) $TiMn_{1.75}$; (F) $TiMn_{2.0}$[190].

The synthesis of $TiMn_{1.5}$ by using r.f. induction furnace in an argon atmosphere has shown a maximum hydrogen storage capacity of 1.5 wt.% with a low plateau region as shown in Fig. 5-2[200]. Electron micrographs of the hydrogenated sample at successive stages had shown dendritic rupturing of the as-synthesised $TiMn_{1.5}$.

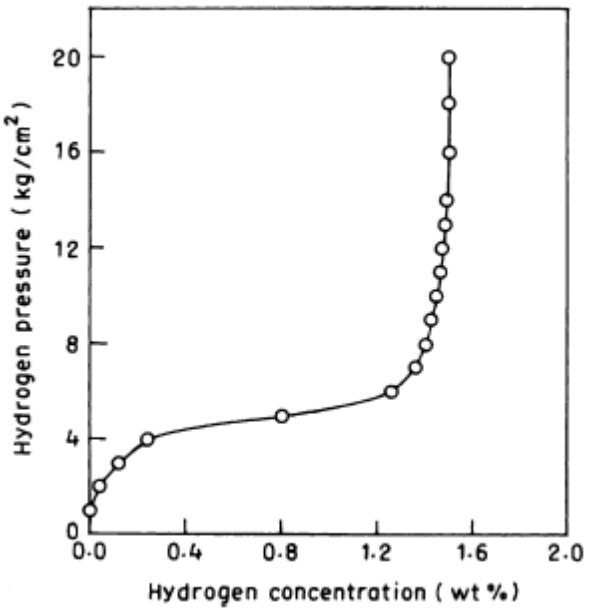

Figure 5- 2.PCT curve of $TiMn_{1.5}$ alloy[200].

$TiMn_2$ alloy (Ti-60 and 61 at.% Mn) were also prepared by an argon arc melting to study the degradation of the hydrogen absorbing capacity in cyclically hydrogenated $TiMn_2$ [44,197]. It was concluded that the introduction of retained hydrogen caused heterogenous strain and/or nano-sized region were the factors that degraded the hydrogen absorption capacity when the number of hydrogenation increased[44,197] as shown in Fig. 5-3.

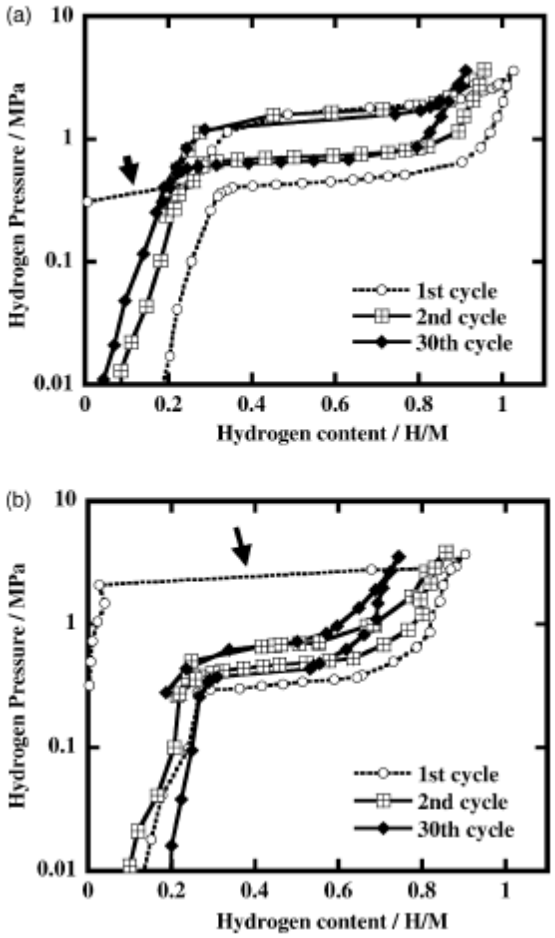

Figure 5- 3.Hydrogen content in (a) Ti-60Mn and (b) Ti-61Mn as a function of hydrogenation cycle[197].

$TiMn_2$has been hydrided using high-pressure techniques[201]. It was found that significant hydriding of $TiMn_2$ started only at a hydrogen pressure above 50 atm as shown in Fig. 5-4. In the pressure range 50 to 80 atm, the hydrogen absorption led to the formation of an α-solid solution with the composition $TiMn_2H_{0.3}$. However this part could not be

considered as representing equilibrium (since it was not reproduced at following cycles) and it characterized only the activation process. The $\alpha \rightarrow \beta$ transition proceeded at considerably higher pressures 700 - 800 atm during the first cycle. In the second cycle P_{abs} decreased to 400 atm and after third cycle the isotherms retained their shape (the activation could be regarded as being completed).

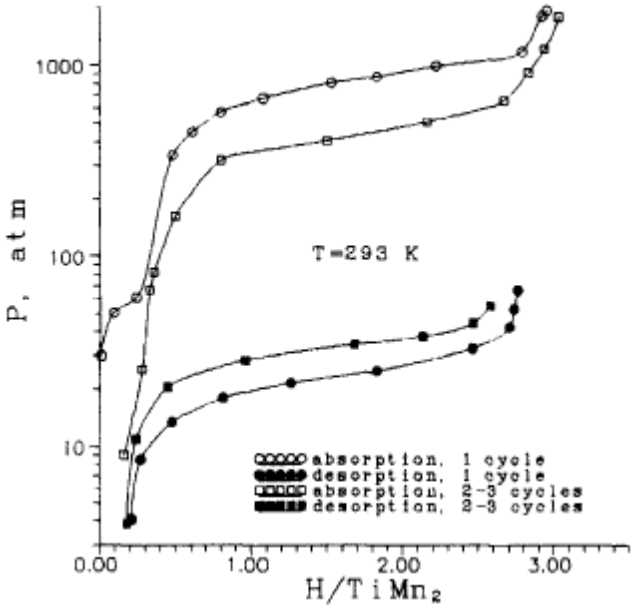

Figure 5- 4.PCT isotherms during activation cycling for the $TiMn_2$ system[201].

5.1.1.2 Partial substitution of Ti or/and Mn with other elements.

In order to improve sorption properties, the AB_2 laves phases are alloyed by partial substitution of either A or B or both by other elements. The largest numbers of investigations are devoted to the study of hydrogen storage alloys based on Ti-Mn_α. The experimentally studied formulae compositions of the investigated Ti-Mn_α based alloys are given below.

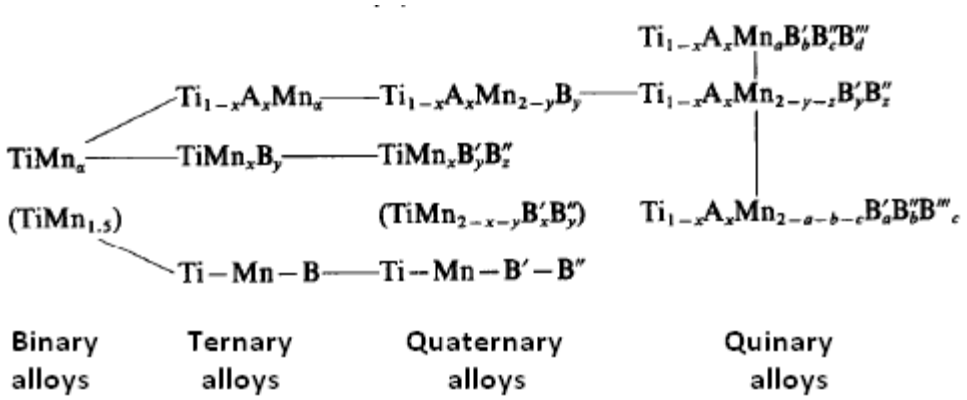

Where A and B', B'', B''' elements substitute the Ti and Mn respectively. The partial substitution of Ti and / or Mn with other elements in the $TiMn_{1.5}$ system has been studied in multiple variations such as Ti-Mn ternary ($Ti_{1-x}Zr_xMn$), quaternary ($Ti_{1-x}Zr_xMn_{2-y}B_y$) and quinary ($Ti_{1-x}Zr_xMn_{2-y-z}B_yC_z$) systems[194,202,203].

For the $Ti_{1-x}Zr_xMn$ system, partial substitution of Ti by Zr results in an increase in crystal lattice constants and a decrease in equilibrium pressure[193]. These are due to the metal-hydrogen interactions which control the stability of metal hydride[204]. The plateau pressure of Zr hydride is lower than that of Ti hydride. The increase in Zr value also results in a decrease of the release hydrogen in spite of increasing the desorbed hydrogen. The reasons for increased hydrogen absorption are due to the radius of the Zr atom is larger than that of the Ti atom and Zr has a stronger affinity with hydrogen than Ti[205].

Partial substitution of Mn by another element yielded a wider range of plateau pressure without loss of hydrogen capacity (except for Al) as shown in Fig. 5-5[190,195].

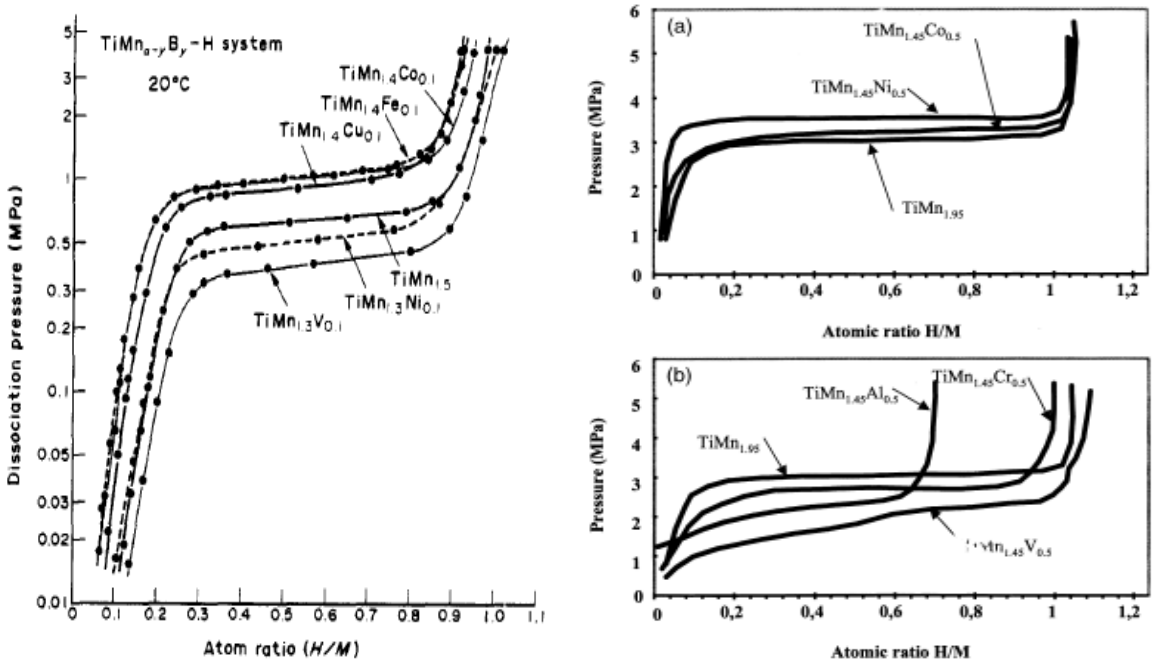

Figure 5- 5.PCT isotherms for the $TiMn_xB_y$ system[190,195].

Ni substitution led to an increase of the plateau pressure. The radius of the Ni (0.1246 nm) atom is smaller than that of the Mn (0.1304 nm) atom. Thus, the unit cell volume decreases, the interstitial sites for hydrogen become smaller and the insertion of hydrogen is harder so that the plateau pressure increases[194,195]. The plateau also becomes less steep. This is due to the annealing process that led to the disappearing (almost) of the minor phase, so that the phase became more and more homogenous and the plateau became flatter[190,194,195].

The Co (0.1252 nm) atom has a smaller radius than that of the Mn atom. However, its substitution did not lead to major change on hydrogen storage properties even if the lattice parameters were changed [194,195].

The Cr (0.13 nm) atom has almost the same radius as Mn atom. Its substitution led to a small decrease of the absorption plateau pressure in spite of almost not affected

desorption plateau pressure. This improvement hysteresis property could be explained by the different hysteresis behavior reported for $TiMn_2$ hydride and $TiCr_2$ hydride[193-195,206].

The V (0.134 nm) atom is larger than that of a Mn atom. Thus, the unit cell volume increases, the interstitial sites for hydrogen become larger and the insertion of hydrogen is easier so that the plateau pressure decreases and also increasing hydrogen content [190,194,195,206,207]. The slope of the plateau also increases. For the hexagonal AB_2 Laves phase, hydrogen atoms mainly occupy two kinds of interstitial site: $[A_2B_2]$ and $[AB_3]$. After V substitution, there are two kinds of B atom: Mn and V. In the alloy there will exist various interstitial sites, for example $[A_2MnV]$,$[A_2Mn_2]$,$[A_2V_2]$, which have different local environments and so different hydrogen affinities. Interstitial sites such as $[AV_3]$ or $[A_2V_2]$ have a strong affinity to hydrogen resulting in a sloping plateau[194,195,206].

The Al (0.143) atom is larger than that of Mn atom. This led to a decrease of the plateau pressure. The hydrogen sorption capacity was also decreases. According to the local environmental model (Ivey 1981), after Al substitution, two kinds of interstitial site (A_2B_2 and AB_3) changed from $[Ti_2Mn_2]$ or $[TiMn_3]$ to $[Ti_2MnAl]$ or $[TiMn_2Al]$ or $[TiMnAl_2]$ or $[Ti_2Al_2]$ or $[TiAl_3]$. As Al did not have a strong affinity to hydrogen, these last two sites should not contain hydrogen resulting in a decrease in hydrogen capacity[194,195,208].

For the $Ti_{1-x}Zr_xMn_{2-y}B_y$ system, where B is any element, as x (Zr content) increases or y (substituted element content) decreases, the dissociation pressure decreases due to a larger lattice constant and provides an increased hydrogen absorption capacity. As for the $Ti_{1-x}Zr_xMn_{2-y-z}B_yC_z$ systems, where B and C are different elements, these compositions have been studied to further improve the properties of $Ti_{1-x}Zr_xMn_{2-y}B_y$ systems, where the type of elements used (C) can further alter the properties of the Ti-Mn system to optimize the properties of the hydrogen storage material[202,203].

5.1.1.3 Catalyzed of $TiMn_2$alloys.

Laves phase ($Ti_{0.9}Zr_{0.2}V_{0.3}Cr_{0.3}Mn_{1.5}$) alloys have been ball milled with *x* wt.% rare-earth-based alloy ($La_{0.7}Mg_{0.25}Zr_{0.05}Ni_{2.975}Co_{0.525}$) as a surface modifier[198]. The hydrogen sorption properties of the composite revealed that the pressure plateau and the hysteresis decreased with the increasing *x*, which were much lower than those of the $Ti_{0.9}Zr_{0.2}V_{0.3}Cr_{0.3}Mn_{1.5}$ alloy (Fig. 5-6). It took only 200 and 2500 s to reach the constant pressure for the hydrogen absorption and desorption reaction. The La-Mg-based alloy particles on the surface facilitate the dissociation of hydrogen molecules into hydrogen atoms during the hydrogen absorption process and the recombination of hydrogen atoms during hydrogen desorption process.

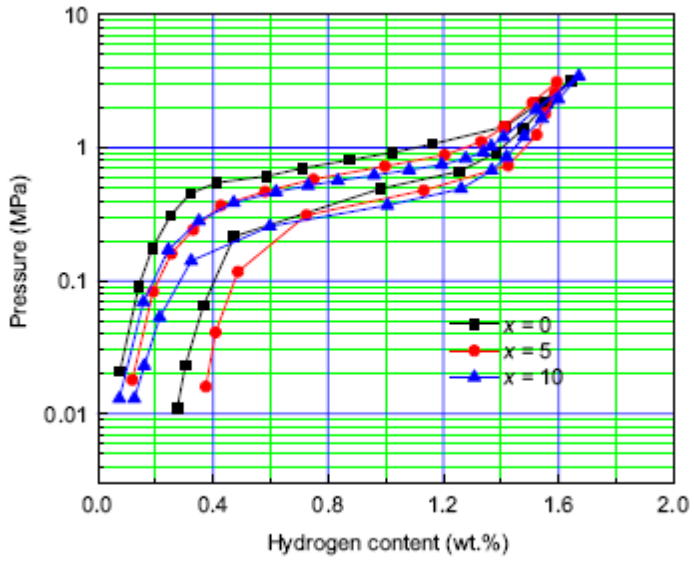

Figure 5- 6.PCT curves of the AB_2 – *x* wt.% $AB_{3.5}$ composite alloys[198].

5.2 Applications

Research on AB_2 intermetallic compounds for hydrogen storage has been ongoing for approximately 40 years. However, at the present time they do not satisfy the requirements for mobile storage due to low gravimetric storage capacities (< 2 wt.%) and often high material cost. The storage capacity limitation is less important for stationary storage applications including thermodynamic devices (refrigerator and air conditioner)[9], fuel cell applications[207,209-212] and energy storage units in remote regions[9,34]. In addition, there are no weight problems in using heavy hydrogen storage tanks if hydrogen is used as a future fuel or fuel additive for sea transportation (because the extra weight can be used to provide ballast to keep the ship stable)[11]. An inexpensive intermetallic system with the requisite sorption pressure at a desired temperature with adequate kinetics has the potential to be a hydrogen storage material for these markets.

5.3 Results and discussions

5.3.1 TiMn commercial

This section has been published in International Journal of Hydrogen Energy[213]. The commercial $Ti_{0.97}Zr_{0.019}V_{0.439}Fe_{0.097}Cr_{0.045}Al_{0.026}Mn_{1.5}$ alloy is a benchmark system for the Ti-Mn mechanical alloying samples. Therefore in this study, the $Ti_{0.97}Zr_{0.019}V_{0.439}Fe_{0.097}Cr_{0.045}Al_{0.026}Mn_{1.5}$ alloy was characterized with respect to its structure, morphology and hydriding properties in order to understand the effect of substituting Zr for the Ti site and V, Fe, Cr and Al for the Mn site within Ti-Mn alloy. Based on these commercial alloy properties, different Ti-Mn alloy compositions were synthesised using a mechanical alloying technique.

5.3.1.1 X-Ray Diffraction (XRD) analysis

X-ray diffraction (XRD) data was collected on the$Ti_{0.97}Zr_{0.019}V_{0.439}Fe_{0.097}Cr_{0.045}Al_{0.026}Mn_{1.5}$ alloy before and after hydrogen sorption measurements were undertaken as shown in Fig. 5-7(a) and (b). The alloy was indexed as a hexagonal C14 Laves phase (P63 / mmc space group) as shown in Fig. 5-7. A single peak in the alloy sample pattern at 2θ = 42.0° was indexed to MnAl phase. The diffraction data was further analysed using the Rietveld method to determine the lattice parameters before and after hydrogenation and dehydrogenation as listed in Table 5-1.

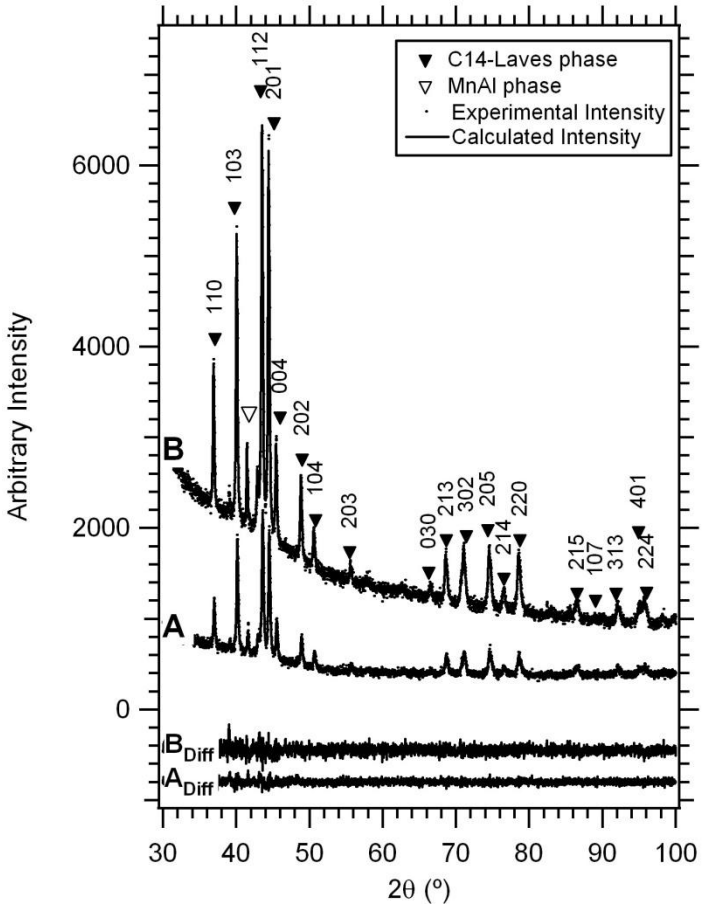

Figure 5- 7.X-Ray Diffraction (XRD) of $Ti_{0.97}Zr_{0.019}V_{0.439}Fe_{0.097}Cr_{0.045}Al_{0.026}Mn_{1.5}$: (a) as received and (b) after absorption and desorption at 25, 40 and 60 °C. Rietveld fits to the data are also displayed along with difference plots.

Table 5- 1:Unit cell parameters of $Ti_{0.97}Zr_{0.019}V_{0.439}Fe_{0.097}Cr_{0.045}Al_{0.026}Mn_{1.5}$ alloy.

	a **(nm)**	***c*** **(nm)**	***V*** **(nm^3)**
Unhydrided	0.4861 ± 0.0001	0.7966 ± 0.0002	0.1630 ± 0.0001
After multiple hydrogenation and dehydrogenation cycles	0.4869 ± 0.0001	0.7981 ± 0.0001	0.1639 ± 0.0001
$TiMn_2$ C14 Laves phase PDF No. 07-0133)	0.4825	0.7917	0.1596

Hydrogen atoms are stored at interstitial sites in the host metal lattice during the absorption process. This causes the lattice to expand and lose some of its symmetry. The co-existence of the non-expanded solid solution phase and anisotropically expanded hydride phase, gives rise to lattice defects and internal strain, ultimately causing the decrepitation of the brittle host metals. For $Ti_{0.97}Zr_{0.019}V_{0.439}Fe_{0.097}Cr_{0.045}Al_{0.026}Mn_{1.5}$ the calculated crystallite size is found to slightly increase from 33 ± 1 nm to 39 ± 1 nm after multiple cycles of hydrogenation and dehydrogenation however the particle size was found to significantly decrease as discussed in the following section. The stored hydrogen atoms within the absorbed sample are later released during the desorption process[44,45], and for$Ti_{0.97}Zr_{0.019}V_{0.439}Fe_{0.097}Cr_{0.045}Al_{0.026}Mn_{1.5}$ the hydrogen is desorbed from the material under ambient pressure and temperature. Therefore lattice expansions cannot be detected using ex-situ XRD as the sample cannot be analysed in the hydride state. It should be noted that it is possible to perform ex-situ XRD on hydrided alloys but they need to be kinetically stable so that they don't desorb hydrogen, often requiring them to be first oxidised[214].

From the XRD results provided in Fig. 5-7 and Table 5-1 it is apparent that there is no structural change after hydrogenation and dehydrogenation cycling. However, an expansion of the crystal lattice for $Ti_{0.97}Zr_{0.019}V_{0.439}Fe_{0.097}Cr_{0.045}Al_{0.026}Mn_{1.5}$ is found to be

larger than for pure $TiMn_2$ due to the incorporation of substituted elements as shown in Table 5-1.

5.3.1.2 Microstructure

The microstructure of the $Ti_{0.97}Zr_{0.019}V_{0.439}Fe_{0.097}Cr_{0.045}Al_{0.026}Mn_{1.5}$ alloy was investigated using scanning electron microscopy (SEM) before and after hydrogenation and dehydrogenation cycling. SEM micrographs are showed in Fig. 5-8 (a) for the as-received alloy and Fig. 5-8 (b) and (c) for particles after hydrogenation and dehydrogenation cycling. The average particle size before hydrogen sorption is 50 - 200 µm. After the sample is cycled multiple times with hydrogen the particle size decreases to generally less than 20 µm and the fractured particle surfaces appear to consist of smooth crystallographic facets. According to previous studies, Ti-Mn alloys are rapidly pulverized into fine powder only by the first hydrogenation cycle and the subsequent hydrogenation cycles result in a slow pulverization process[44,190]. During the first hydrogenation cycle, hydrogen introduces strain into the alloy surface and when the strain reaches a critical value for cracking, spalling occurs at the surface. The freshly created surfaces provide larger surface area and shorter distances for H to diffuse. These factors bring about rapid hydrogen sorption kinetics. This decrepitating process occurs to some degree with each hydrogenation cycle and can lead to internal cleavage fractures in the particles as seen in Fig. 5-8 (c). During the SEM investigations energy dispersive spectroscopy (EDS) was undertaken to verify the elemental composition of the alloy. The EDS results (Fig. 5-9) are compared to inductively coupled plasma (ICP) results reported by Sigma-Aldrich in Table 5-2. It is evident that the composition of the alloy is consistent between analysis techniques and as such the elemental composition $Ti_{0.97}Zr_{0.019}V_{0.439}Fe_{0.097}Cr_{0.045}Al_{0.026}Mn_{1.5}$ is accurate.

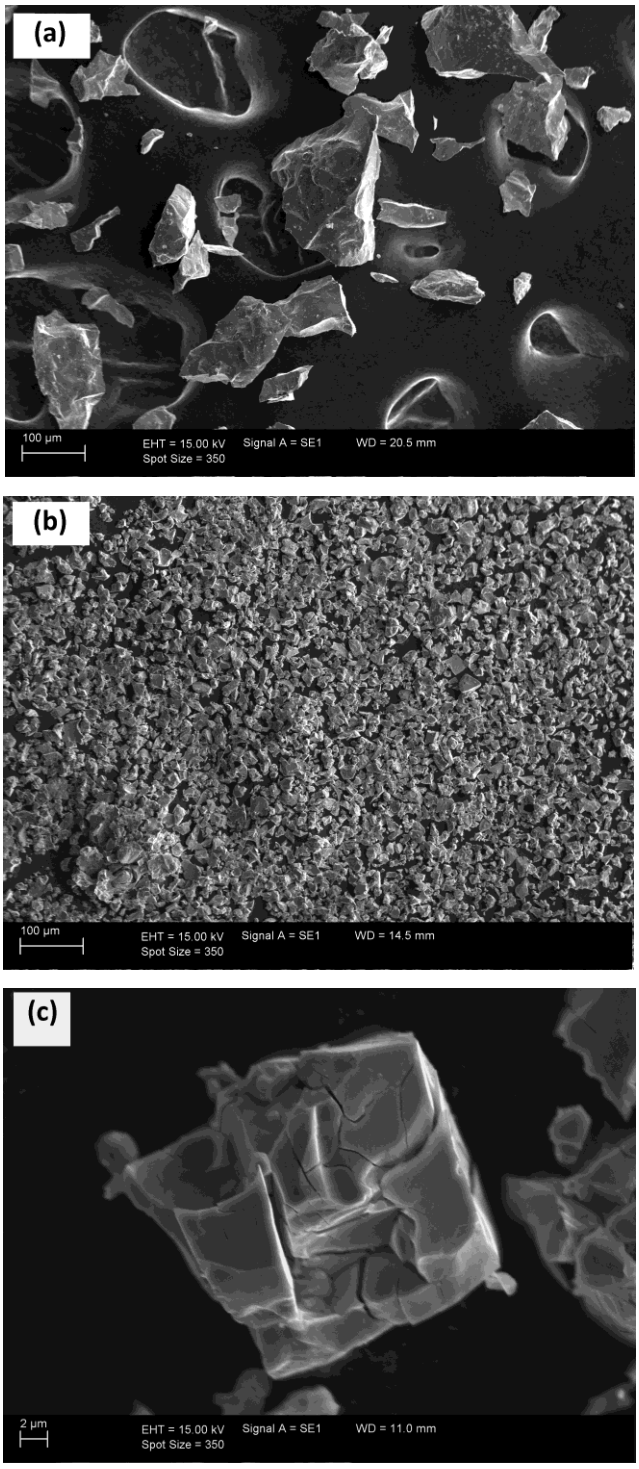

Figure 5- 8.(a) SEM of the as-received $Ti_{0.97}Zr_{0.019}V_{0.439}Fe_{0.097}Cr_{0.045}Al_{0.026}Mn_{1.5}$ alloy and (b & c) after hydrogenation cycling.

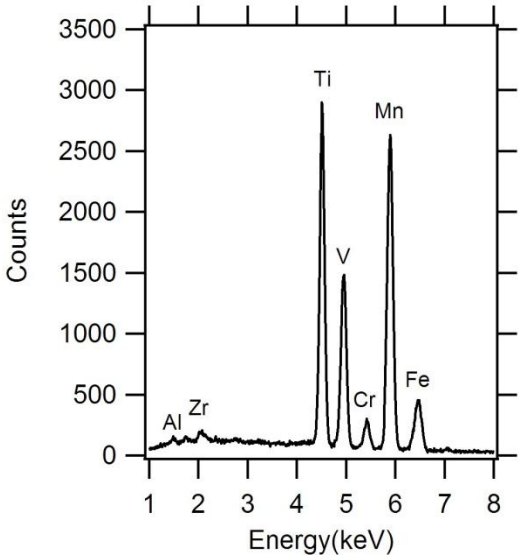

Figure 5- 9.EDS spectra of $Ti_{0.97}Zr_{0.019}V_{0.439}Fe_{0.097}Cr_{0.045}Al_{0.026}Mn_{1.5}$ alloy.

Table 5- 2: Elemental composition of alloy

Element	ICP (Sigma-Aldrich) wt.%	EDS (SEM) wt.%
Mn	50.9	50.2 ± 0.33
Ti	28.7	29.3 ± 0.26
V	13.8	13.6 ± 0.22
Fe	3.35	3.51 ± 0.21
Cr	1.45	1.45 ± 0.15
Zr	1.10	1.36 ± 0.22
Al	0.43	0.45± 0.07

5.3.1.3 Hydrogen Sorption

Hydrogen sorption pressure-composition isotherms (PCI's) at 25, 40 and 60°C are shown in Fig. 5-10. Each data point is the result of a kinetic sorption measurement until hydrogen equilibrium is achieved. The size of the plateau region decreases as a function

of temperature. With increasing sorption temperature from 25°C, 40°C to 60°C, the amount of absorbed hydrogen decreases from 1.71 ± 0.01 wt.%, 1.56 ± 0.01 wt.% and 1.43 ± 0.01 wt.% respectively. The maximum hydrogen storage capacity at room temperature (1.71 wt.%) is lower than for the pure $TiMn_{1.5}$ system (1.86 wt.%) [190]. This is likely due to the presence of a MnAl impurity phase within the$Ti_{0.97}Zr_{0.019}V_{0.439}Fe_{0.097}Cr_{0.045}Al_{0.026}Mn_{1.5}$ commercial alloy that does not react sufficiently with hydrogen. The hysteresis factor, defined as $\ln P_{abs}/P_{des}$, for $Ti_{0.97}Zr_{0.019}V_{0.439}Fe_{0.097}Cr_{0.045}Al_{0.026}Mn_{1.5}$ was also found to be a function of temperature as shown in Table 5-3. Both the absorption and desorption plateaus increased with increasing temperature and this feature along with the hydrogen capacity and hysteresis result conform to the classic behaviour of metal-hydride systems[193,215].

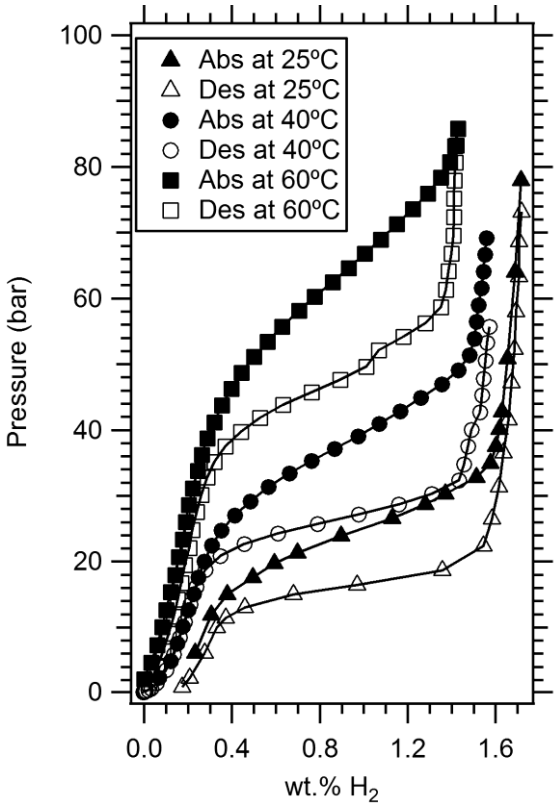

Figure 5- 10.PCI curves of the $Ti_{0.97}Zr_{0.019}V_{0.439}Fe_{0.097}Cr_{0.045}Al_{0.026}Mn_{1.5}$ alloy for hydrogen absorption and desorption at 25, 40 and 60°C.

Table 5- 3:Hydrogen sorption properties of $Ti_{0.97}Zr_{0.019}V_{0.439}Fe_{0.097}Cr_{0.045}Al_{0.026}Mn_{1.5}$.

Temperature (°C)	Maximum Capacity (wt.% H_2)	Plateau Pressure		
		P_{Abs}(bar)	P_{Des}(bar)	Hysteresis $\ln P_{abs}/P_{des}$
25	1.71 ± 0.01 at 78 bar	25.20 ± 0.03	16.15 ± 0.02	0.445 ± 0.002
40	1.56 ± 0.01 at 69 bar	39.01 ± 0.03	27.05 ± 0.04	0.366 ± 0.002
60	1.43 ± 0.01 at 86 bar	62.70 ± 0.04	47.06 ± 0.09	0.287 ± 0.003

The kinetics of hydrogen absorption and desorption were measured by recording pressure data at the different temperatures at which PCIs were collected. Fig. 5-11(a) and (b) show the kinetic curves for absorption and desorption, respectively, at the midpoint of the plateau. The sorption kinetics shows that the alloy reaches a hydrogen sorption equilibrium within 15 minutes.

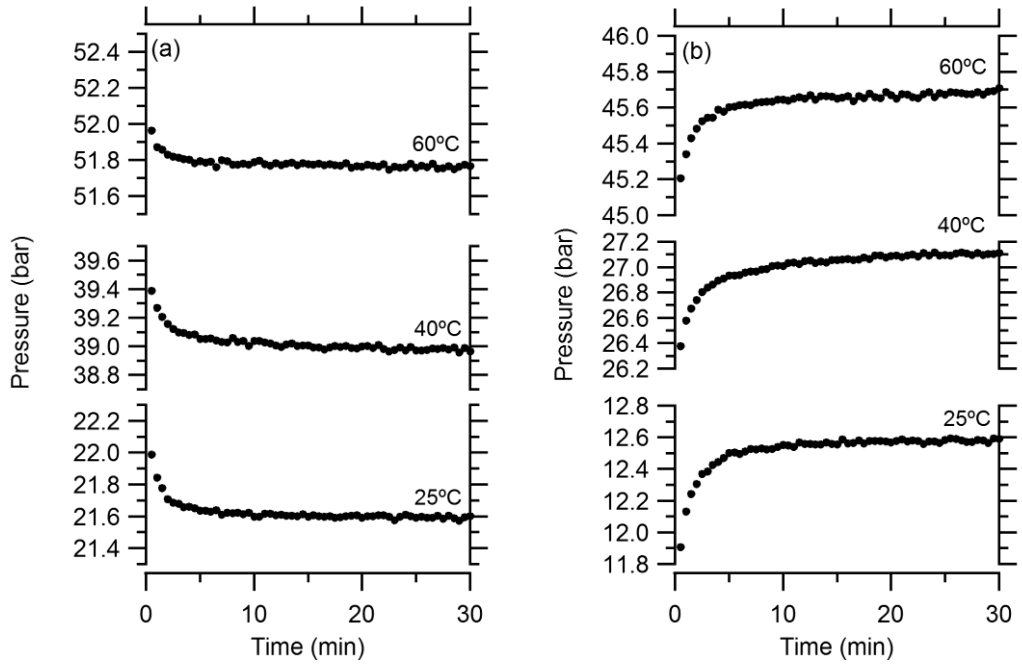

Figure 5- 11.Hydrogenation kinetics on (a) absorption and (b) desorption at different temperatures in $Ti_{0.97}Zr_{0.019}V_{0.439}Fe_{0.097}Cr_{0.045}Al_{0.026}Mn_{1.5}$.

The enthalpy (*ΔH*) and entropy (*ΔS*) of hydrogen desorption can be calculated from the van't Hoff equation:

$$\ln\left(\frac{f_{H2}}{f_0}\right) = \frac{\Delta H}{RT} - \frac{\Delta S}{R}$$

where fH_2 is the hydrogen fugacity corresponding to the absorption or desorption plateau pressures (see elsewhere for more information[53]).The van't Hoff plot provided in Fig. 5-12 was constructed from the absorption/desorption pressure of the PCI curves (Fig. 5-10) at a wt.% of 0.9 - 1.0 according to van't Hoff equation. This allows for the hydride formation (absorption) and decomposition (desorption) thermodynamics (*ΔH* and *ΔS*) to be determined using a weighted least-squares method from the fit in the van't Hoff plot (ln *f* versus 1/*T*). The calculated ΔH and ΔS values are provided in Table 5-4 in comparison to other similar Ti-Mn systems in the literature.

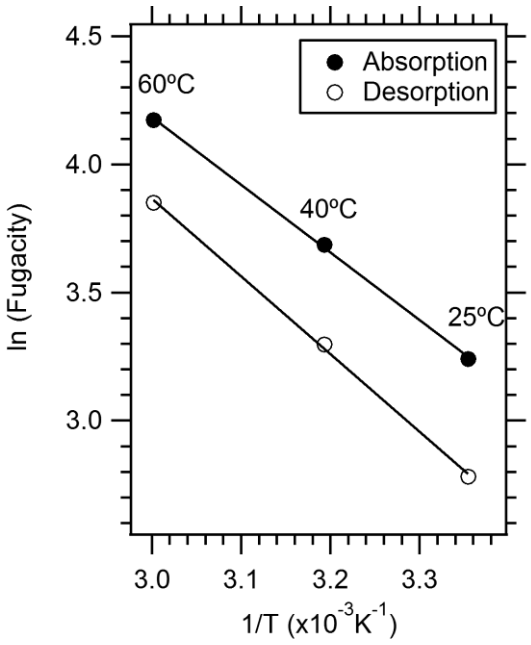

Figure 5- 12.van't Hoff plot for the $Ti_{0.97}Zr_{0.019}V_{0.439}Fe_{0.097}Cr_{0.045}Al_{0.026}Mn_{1.5}$ alloy.

As the Ti content increases within a Ti-Mn alloy, the amount of absorbed H increases uniformly. At a Ti content of 37 at.%, there is a sudden increase of the amount of absorbed H indicating that there is a minimum lattice constant required to absorb a large amount of H within the Laves phase structure[190]. The amount of desorbed H also increases until the Ti content reaches about 40 at.% ($TiMn_{1.5}$) at this concentration the amount of desorbed H decreases[190]. This may be due to the β-Ti phase existing within high Ti-content alloys, forming a very stable hydride where most of absorbed H is trapped within titanium. Therefore $TiMn_{1.5}$ shows the most desirable properties as hydrogen storage material. The maximum absorbed hydrogen reported for the pure $TiMn_{1.5}$ system is 1.86 wt.% H_2 and the maximum desorbed hydrogen is 1.53 wt.% H_2[190]. This data demonstrates that the $TiMn_{1.5}$ system contains hydrogen even after desorption at 20°C. The partial substitution of Ti and/or Mn with other elements in the $TiMn_{1.5}$ system has been studied in multiple variations such as Ti-Mn ternary ($Ti_{1-x}Zr_xMn$), quaternary ($Ti_{1-x}Zr_xMn_{2-y}B_y$) and quinary ($Ti_{1-x}Zr_xMn_{2-y-z}B_yC_z$) systems [194,202,203]. With increasing substitution, the lattice constant increases which leads to a decrease of both the plateau pressure and the hysteresis in conjunction with an increased hydrogen capacity [190,195].

For the $Ti_{1-x}Zr_xMn$ system, the increase in x (Zr content) results in a decrease of the quantity of desorbed hydrogen despite an increase in the absorbed hydrogen[190,205]. Both the absorption and desorption plateau pressure decrease with the increase of Zr in the system. The reason for the increase in the quantity of absorbed hydrogen is that Zr has a stronger affinity for hydrogen and larger metallic radius than Ti whilst the decrease in desorbed hydrogen is related to the stability of titanium hydride[204]. The plateau pressure of Zr hydride is lower than Ti hydride. Therefore Zr hydride is more stable than Ti hydride. As a result, a high Zr content result in difficulties in hydrogen desorption from the Ti-Mn system. For the $Ti_{1-x}Zr_xMn_{2-y}B_y$ system, where B is any element, as x (Zr content) increases or y (substituted element content) decreases, the dissociation

pressure decreases showing larger lattice constant and a larger hydrogen absorption capacity. The influence of the substitution for Mn by other elements was correlated with the metallic radius and the affinity with H of the substitution elements[193,194]. In the case of Al and V substitution, the metallic radius was larger than that of Mn, so the lattice constant increased and the plateau pressure was reduced. In the case of Fe, the metallic radius is smaller than Mn, therefore the lattice constant decreased and the plateau pressure increased. However in the case of Cr, the lattice constant increases slightly albeit the metallic radius is almost the same as that of Mn. The residual hydrogen is also less of a problem in this system compared to $TiMn_{1.5}$ and $TiMn_{2-y}B_y$ systems[190]. As for the $Ti_{1-x}Zr_xMn_{2-y-z}B_yC_z$ systems, where B and C are different elements, these compositions have been studied to further improve the properties of $Ti_{1-x}Zr_xMn_{2-y}B_y$ systems, where the type of elements used (C) can further alter the properties of the Ti-Mn system to optimise the properties of the hydrogen storage material[202,203].

Table 5- 4:Comparison of *ΔH* and *ΔS* values of several Ti-Mn alloy systems .

System	Absorption		Desorption			
	ΔH (kJ/ mol H_2)	*ΔS* (J/mol H_2/K)	*ΔH* (kJ/mol H_2)	*ΔS* (J/mol H_2/K)	1 bar desorption equilibrium temperature (°C)	Calculated P_{Des} at 20°C (bar)
A: $Ti_{0.97}Zr_{0.019}V_{0.439}Fe_{0.097}Cr_{0.045}Al_{0.026}Mn_{1.5}$[213]	-21.7 ± 0.1	-99.8 ± 0.2	25.4 ± 0.1	108.5 ± 0.2	-39.0 ± 0.5	13.9 ± 0.3
B: $Ti_{0.98}Zr_{0.02}V_{0.43}Fe_{0.09}Cr_{0.05}Mn_{1.5}$[216]	-	-	27.4	112.0	-28.5	9.29
C: $Ti_{0.98}Zr_{0.02}V_{0.41}Fe_{0.08}Cr_{0.05}Mn_{1.46}$[215]	-	-	29.2	121.2	-32.2	13.42
D: $Ti_{0.95}Zr_{0.05}V_{0.43}Fe_{0.08}Al_{0.01}Mn_{1.48}$[215]	-25.6	-	29.4	106.5	2.9	2.11
E: $Ti_{0.955}Zr_{0.045}V_{0.43}Fe_{0.12}Al_{0.03}Mn_{1.52}$[215]	-	-	28.7	116.9	-27.6	9.82

*Experimental P_{Des} reported for system C ($Ti_{0.98}Zr_{0.02}V_{0.41}Fe_{0.08}Cr_{0.05}Mn_{1.46}$) and D ($Ti_{0.95}Zr_{0.05}V_{0.43}Fe_{0.08}Al_{0.01}Mn_{1.48}$) are 6.5 bar and 3.4 bar respectively.

From Table 5-4, it shown that the increase in Zr content results in a decrease in equilibrium pressure and the introduction of V, Cr and Al leads to further reduction in the hydrogen equilibrium pressure of these alloy systems. The plateau pressure of system A ($Ti_{0.97}Zr_{0.019}V_{0.439}Fe_{0.097}Cr_{0.045}Al_{0.026}Mn_{1.5}$), B ($Ti_{0.98}Zr_{0.02}V_{0.43}Fe_{0.09}Cr_{0.05}Mn_{1.5}$) and E ($Ti_{0.955}Zr_{0.045}V_{0.43}Fe_{0.12}Al_{0.03}Mn_{1.52}$) is 13.9 ± 0.3, 9.29 and 9.82 bar respectively at 20°C. For both system C ($Ti_{0.98}Zr_{0.02}V_{0.41}Fe_{0.08}Cr_{0.05}Mn_{1.46}$) and D ($Ti_{0.95}Zr_{0.05}V_{0.43}Fe_{0.08}Al_{0.01}Mn_{1.48}$) the experimental equilibrium pressures do not match the pressures calculated from the thermodynamic properties. The discrepancy between the calculated and measured equilibrium pressures indicates that the reported thermodynamic data is not appropriate for these systems. The differences in composition between the alloys in Table 5-4 obviously lead to changes in the hydrogen sorption behaviour.

5.3.2 TiMn synthesized by mechanical alloying technique.

Based on the commercial $Ti_{0.97}Zr_{0.019}V_{0.439}Fe_{0.097}Cr_{0.045}Al_{0.026}Mn_{1.5}$ alloy properties, Ti-Mn alloy compounds with compositions $TiMn_2$, $Ti_{0.97}Zr_{0.019}Mn_{1.5}Cr_{0.57}$ and $Ti_{0.7875}Zr_{0.2625}Mn_{0.8}Cr_{1.2}$ were synthesised using a mechanical alloying technique. The synthesised alloys were characterized based on their structure, morphology and hydriding properties.

5.3.2.1 X-Ray Diffraction (XRD)

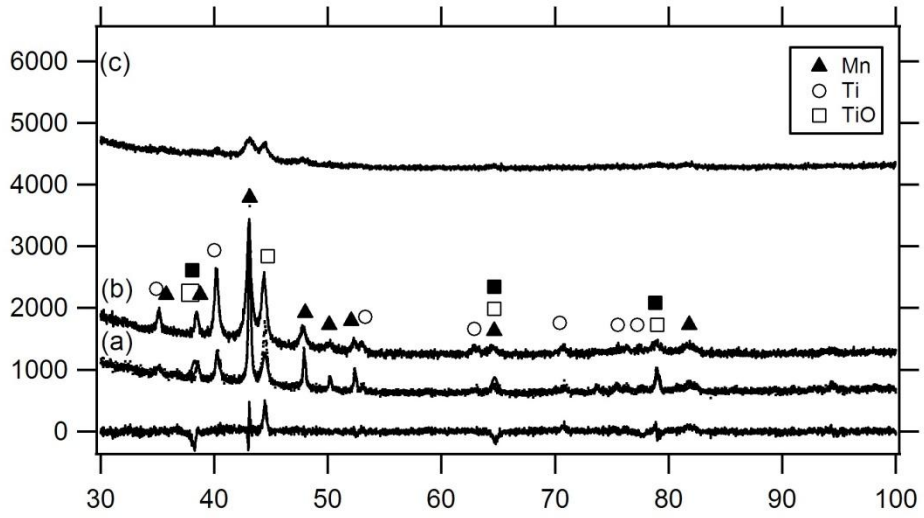

Figure 5- 13.XRD pattern of as-milled $TiMn_2$ powders using BPR of 12:1 at (a) 2 h, (b) 12 h and (c) 40 h milling times.

Fig. 5-13 shows the XRD patterns of the as-milled $TiMn_2$ powders subjected to increased times of milling using a ball to powder mass ratio (BPR) of 12:1. 3 drops of toluene as a process control agent (PCA) was added to the starting reagents (5 grams) during milling. After 12 h of milling, both Ti and Mn peaks were still present. The diffraction peaks are slightly broader compare to those after milling for 2 h. TiC peaks were observed in the XRD pattern due to addition of toluene during milling process. TiC and TiO phases have similar major XRD peaks, so those denoted in Fig. 5-13 most likely represent the presence of a combination of both TiC and TiO in the sample. After 40 h milling, the sample became quite nanocrystalline. All peaks except the strongest peak of Mn become nearly invisible. The position of the remaining peak of Mn was shifted to a lower angle.

The as-milled $TiMn_2$ sample was then annealed at 800°C under vacuum for 3 hours. The XRD pattern shown in Fig. 5-14 consists of peaks related to $TiMn_2$, TiC, TiO and Mn. The $TiMn_2$ phase was easily indexed on the basis of the hexagonal C14-Laves phases (*$P6_3$ / mmc* space group). The calculated lattice parameters determined by Rietveld analysis are listed in Table 5-5. This result showed that the crystalline phase of Ti-Mn could be achieved through annealing of its milled powder. This is consistent with previous study of synthesising crystalline $Ti_{50}Mn_{50}$ alloy by milling for 40 h and annealing at 700 - 900°C [65].Annealing was also reported to increase the homogeneity of the crystal structure of the sample[190].

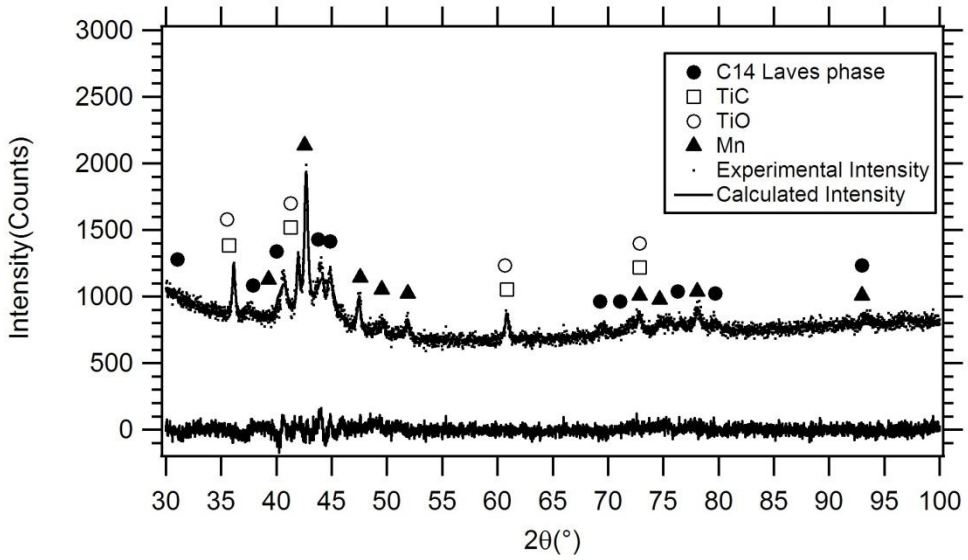

Figure 5- 14.XRD pattern of annealed $TiMn_2$ using BPR of 12:1.

During mechanical alloying, powder particles are subjected to high-energy collision, which causes the powder particles to be cold-welded together and fractured. The essential condition for a successful mechanical alloying process is the balance between cold-welding and fracturing. However, this balance may not be obtained by the milling process itself, especially when soft materials are used. For such cases, cold welding among powder particles and between powder particles and milling tools becomes a

serious problem. In order to obtain the balance between the welding and fracturing, a PCA is added in the milling process. The PCA adsorbs on the surface of the powder particles and minimizes the cold welding effect[56,59]. It is known that Mn is much softer and is more easily to be cold welded to the milling tools compare to Ti. Brinell hardness reported for Ti and Mn are 716 MNm^{-2} and 196 MNm^{-2} respectively. To avoid this, toluene was used as a PCA. However, the addition of toluene resulted in the formation of TiC in the sample. Hydrocarbon PCAs have been reported to introduce carbon and/or oxygen into the powder particles, resulting in the formation of carbides and oxides which are uniformly dispersed in the matrix[56].

An XRD pattern of the starting Ti powder (Fig. 5-15) also revealed that a minor oxide phase already present in the purchased product. Ti powder is known to be more reactive with oxygen when in extremely small particle size (in this case -100 mesh powder)[56,64]. The strongest peak in the starting Ti powder at 36.6° could not be indexed to any known pure Ti element or oxide and is an unknown component. This indicates that there could be an impurity in the Ti starting powder. As a result of these impurity, carbide and oxide phases, the level of Ti available to form $TiMn_2$ alloy was reduced and a high level of Mn was left in the sample. Based on Rietveld analysis in Table 5-5, only 37.24 wt.% $TiMn_2$ phase was formed in the sample.

Table 5- 5:Rietveld analysis for phase composition and lattice parameter calculated from XRD patterns in Fig. 5-13, 5-14, 5-17 and 5-19. Mathematical fitting uncertainties are provided (2 standard deviations).

Alloys	Annealed (wt.%)		Lattice parameters		
			a(nm)	c(nm)	V(nm^3)
$TiMn_2$ (BPR 12:1)	C14 TiO/TiC Mn	37.24±0.5 22.16±0.5 40.59±0.5	0.4821	0.7856	0.1581
$TiMn_2$ (BPR 20:1)	TiO/TiC Mn	25.22±0.3 74.77±0.3	-	-	-
$Ti_{0.97}Zr_{0.019}Mn_{1.5}Cr_{0.57}$	C14 TiO/TiC Mn	31.5±1.2 10.31±0.8 58.19±1.6	0.4837	0.7892	0.1600
$Ti_{0.7875}Zr_{0.2625}Mn_{0.8}Cr_{1.2}$	C14 TiO/TiC Cr Zr	32.81±0.5 16.41±0.7 39.98±0.5 10.79±0.5	0.4859	0.7940	0.1623
$TiMn_2$ C14 Laves phase PDF No. 07-0133	-	-	0.4825	0.7917	0.1596

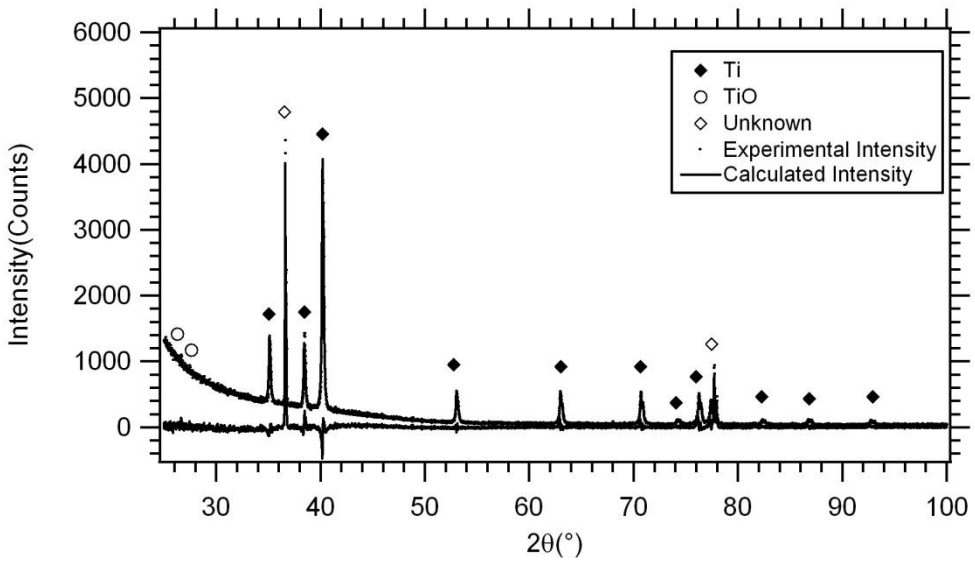

Figure 5- 15.XRD pattern of starting powder Ti.

Figure 5- 16.BF image and the corresponding EDS elemental mapping of $TiMn_2$ using BPR of 12:1. (bright region is shown by the black arrow)

Fig. 5-16 shows the bright field (BF) image of the sample$TiMn_2$ using BPR of 12:1 after 40 hours milled and annealed at 800°C and the corresponding EDS elemental mapping. The BF image shows no sign of a lamellae structure. At the beginning of mechanical alloying, different elemental powder particles are partially mixed and large blocks containing coarse layers have formed[217]. Formation of a coarse lamellae structure of initial powders may be due to low plastic deformation. Continuous cold welding and fracturing result coarse layers to be fractured and flattened and subsequently fresh metal surfaces welded together[217]. This results in formation of fine layered structure and inter-diffusion of elements across layers[217]. With further milling up to 40 h, the layers became hardly detectable. The elemental mapping of the sample shows the characteristic energies of Ti and Mn. Both elements are distributed homogeneously throughout the sample except the bright region. The brighter region contains more Mn and less Ti than the darker region. This observation indicates that there may not be enough Ti content to diffuse in the (Ti, Mn) matrix forming different contrast in the sample.

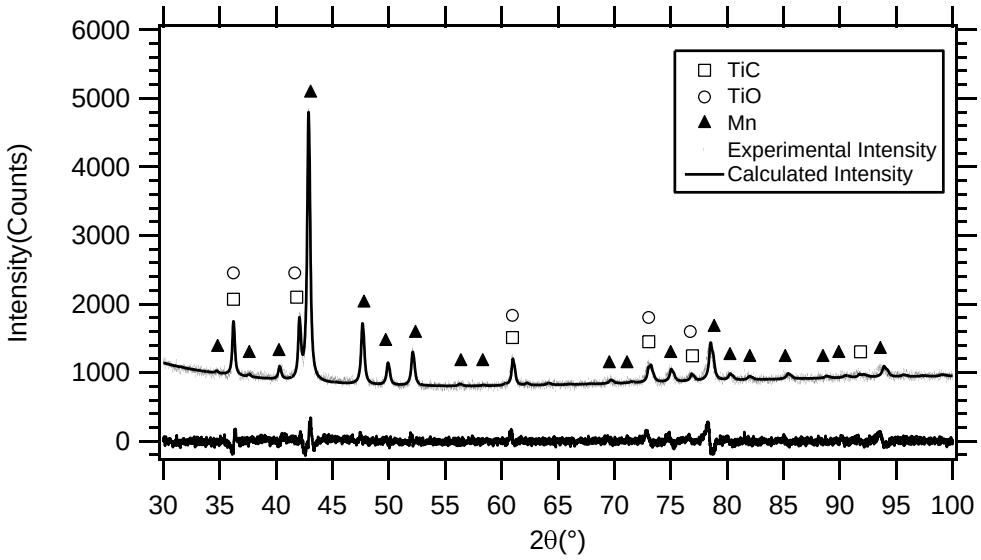

Figure 5- 17.XRD pattern of $TiMn_2$ using BPR of 20:1.

Fig. 5-17 shows the XRD pattern of $TiMn_2$ sample prepared by mechanical alloying the starting reagents using a BPR of 20:1 for 40 hours. 3 drops of toluene were added to the starting reagents during milling. Then the as-milled sample was annealed at 800°C under vacuum for 3 hours. The XRD pattern consists of peaks related to TiC, TiO and Mn. $TiMn_2$ Laves phases were not detected in the sample. At a high ball to powder ratio, the number of collisions per unit times increases. Due to a small amount of the toluene used, only a limited surface area of the Mn particles could be covered by it. As a result, excessive cold welding occurred; more Mn particles get stuck to the milling tools. Therefore due to low level of Ti and Mn, alloying reaction to form $TiMn_2$ could not take place in this sample.

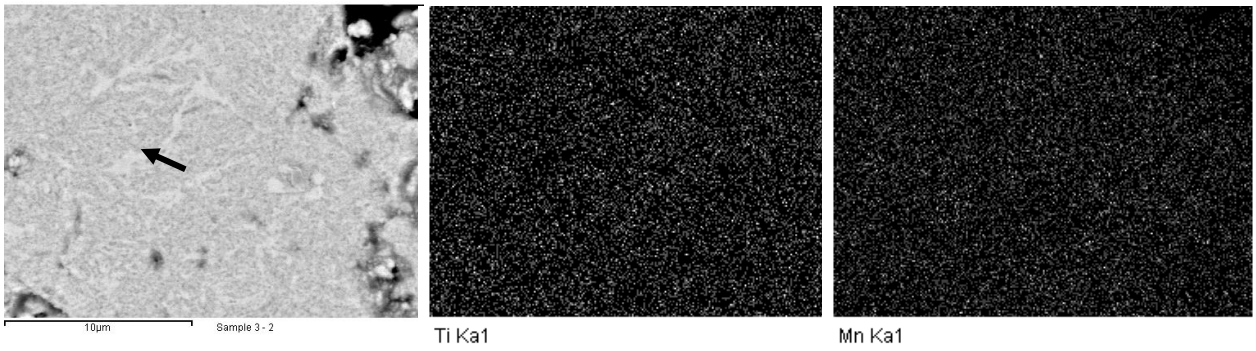

Figure 5- 18.BF image and the corresponding EDS elemental mapping of $TiMn_2$ using BPR of 20:1. (bright region is shown by the black arrow)

Fig. 5-19 and Fig. 5-20 show the XRD patterns of $Ti_{0.97}Zr_{0.019}Mn_{1.5}Cr_{0.57}$ and $Ti_{0.7875}Zr_{0.2625}Mn_{0.8}Cr_{1.2}$ samples respectively prepared by mechanical alloying the starting reagents using a BPR of 12:1 for 40 hours. 3 drops of toluene was added to the starting reagents during milling. Then the as-milled samples were annealed at 800°C under vacuum for 3 hours. Both XRD patterns consist of peaks related to $TiMn_2$, TiC, TiO and Mn. As a result of impurity, carbide and oxide phases' presence in these samples, the level of Ti available to form $TiMn_2$ alloy were reduced. Based on Rietveld analysis in Table 5, only 31.5 wt.% and 32.81 wt.% $TiMn_2$ phase was formed in $Ti_{0.97}Zr_{0.019}Mn_{1.5}Cr_{0.57}$ and $Ti_{0.7875}Zr_{0.2625}Mn_{0.8}Cr_{1.2}$ respectively. For $Ti_{0.7875}Zr_{0.2625}Mn_{0.8}Cr_{1.2}$, due to its low wt.% $TiMn_2$ phase formed and the high level of substitute elements used (Zr and Cr), only limited levels of partially substitution could take place in the sample. As a result, peaks related to Cr and Zr phases were still detected in this sample as shown in Fig. 20. The effects of partial substitution of Zr for Ti and Cr for Mn are shown in Table 5 - 5. With increasing Zr and Cr content, the lattice parameter of the C14- Laves phases were also increased. This is due to the atom radius of Zr and Cr are bigger than that of Mn.

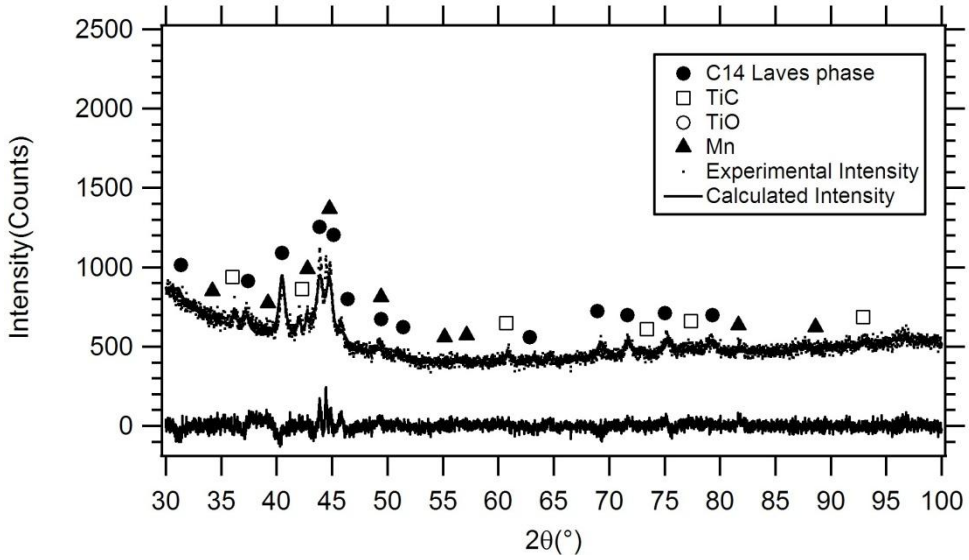

Figure 5- 19.XRD pattern of $Ti_{0.97}Zr_{0.019}Mn_{1.5}Cr_{0.57}$.

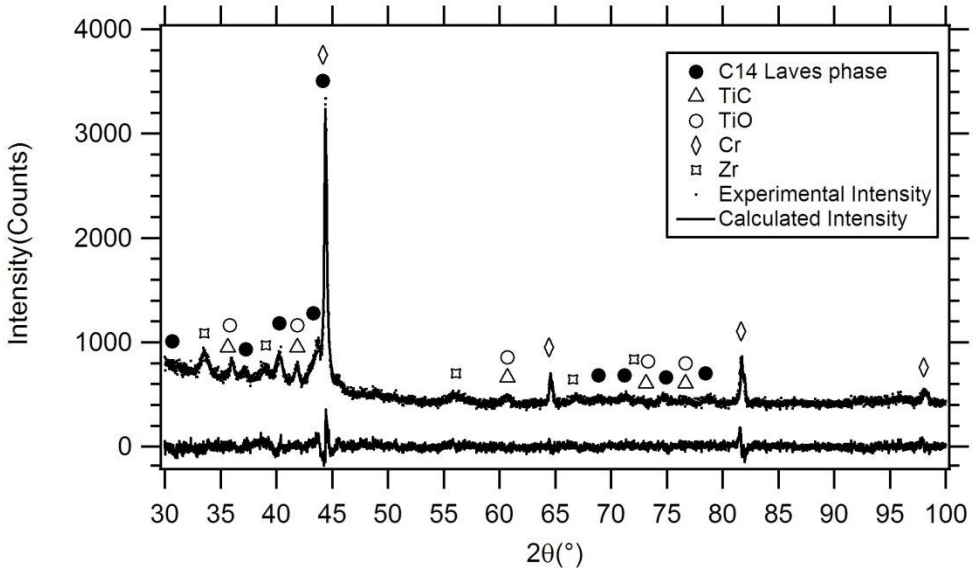

Figure 5- 20.XRD pattern of $Ti_{0.7875}Zr_{0.2625}Mn_{0.8}Cr_{1.2}$.

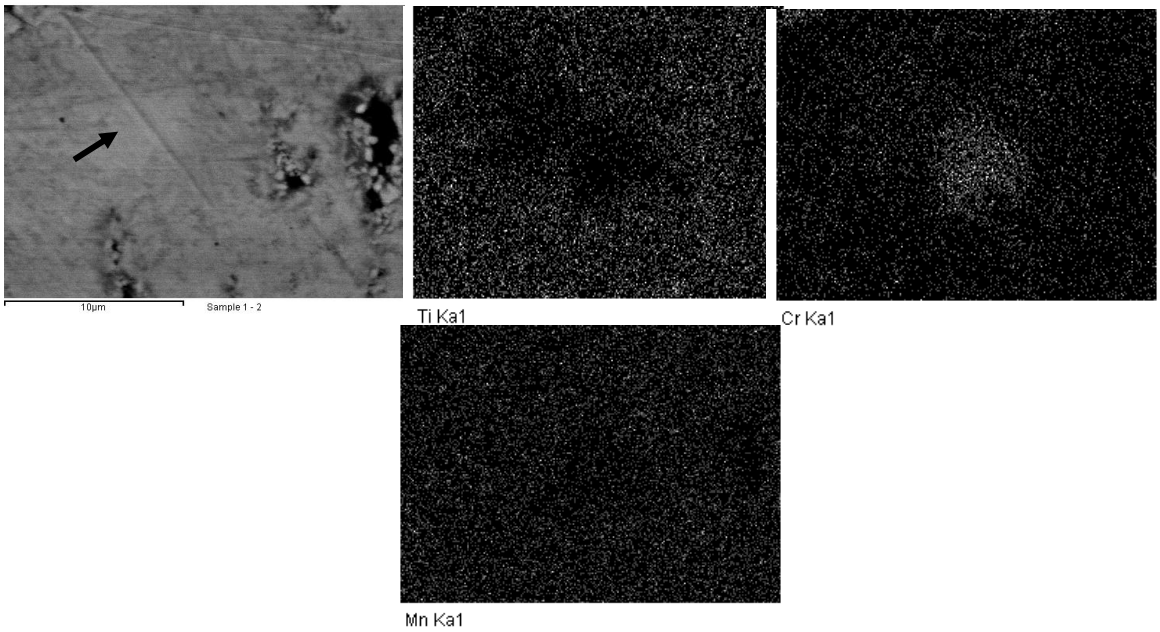

Figure 5- 21.BF image and the corresponding EDS elemental mapping of $Ti_{0.97}Zr_{0.019}Mn_{1.5}Cr_{0.57}$ (bright region is shown by the black arrow).

Fig. 5-21 shows the BF image of the sample$Ti_{0.97}Zr_{0.019}Mn_{1.5}Cr_{0.57}$ and its corresponding EDS elemental mapping. All elements are distributed homogeneously throughout the sample except the bright region. The brighter region contains more Cr, Mn and less Ti than the darker region. This indicates that the alloy was composed of the C14 Laves phase (dark region) and some impurity phase of Mn and Cr (bright region). This result is also similar with sample $Ti_{0.7875}Zr_{0.2625}Mn_{0.8}Cr_{1.2}$ as shown in Fig. 5-22. However Zr element was also detected in this sample due to high level of Zr in sample $Ti_{0.7875}Zr_{0.2625}Mn_{0.8}Cr_{1.2}$ compare to $Ti_{0.97}Zr_{0.019}Mn_{1.5}Cr_{0.57}$.

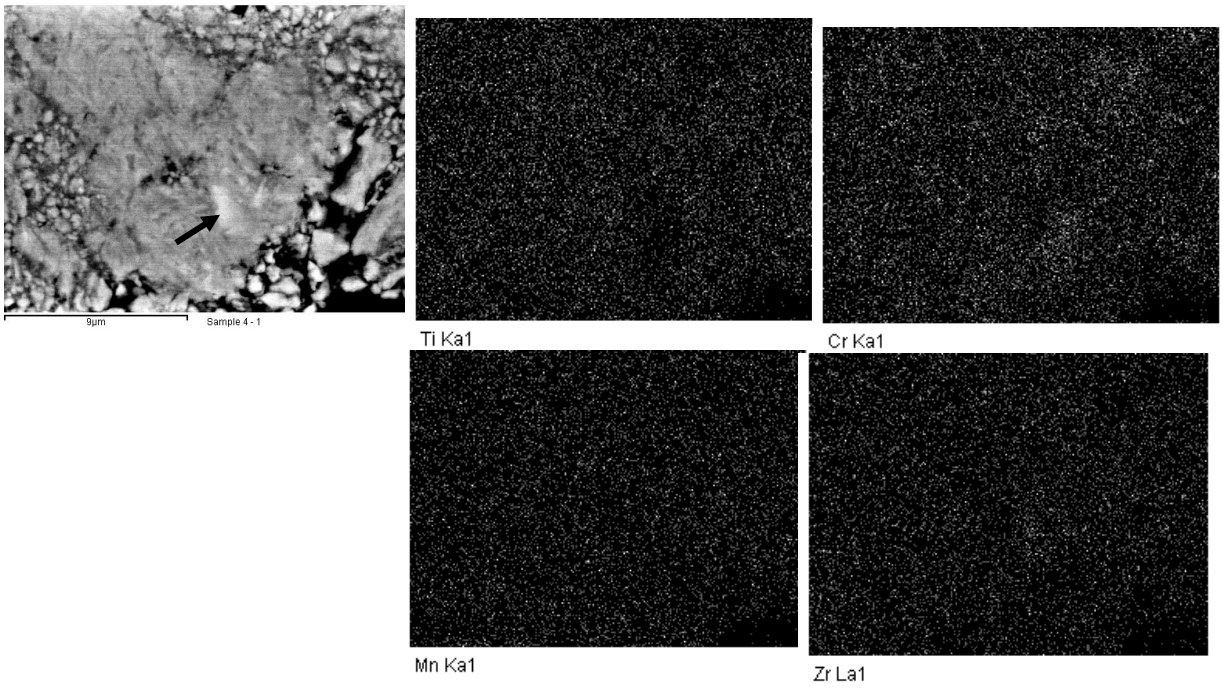

Figure 5- 22.BF image and the corresponding EDS elemental mapping of $Ti_{0.7875}Zr_{0.2625}Mn_{0.8}Cr_{1.2}$(bright region is shown by the black arrow).

EDS data verifies the presence of high quantities of Ti and Mn in all samples (Fig. 5-23a, b, c and d). EDS also showed the existence of Fe, Cr and Ni for all samples (Fig. 23a, b, c and d), as a result of an excessive wear of the milling tools (Fig. 5-23e). Zr and Cr are the results of partial substitution of Ti and Mn in sample $Ti_{0.97}Zr_{0.019}Mn_{1.5}Cr_{0.57}$ (Fig. 5-23c) and $Ti_{0.7875}Zr_{0.2625}Mn_{0.8}Cr_{1.2}$ (Fig. 5-23d).Cr contents are higher in Fig. 23d due to high level of Cr in sample $Ti_{0.7875}Zr_{0.2625}Mn_{0.8}Cr_{1.2}$ compare to sample $Ti_{0.97}Zr_{0.019}Mn_{1.5}Cr_{0.57}$. C comes from using toluene as a PCA.

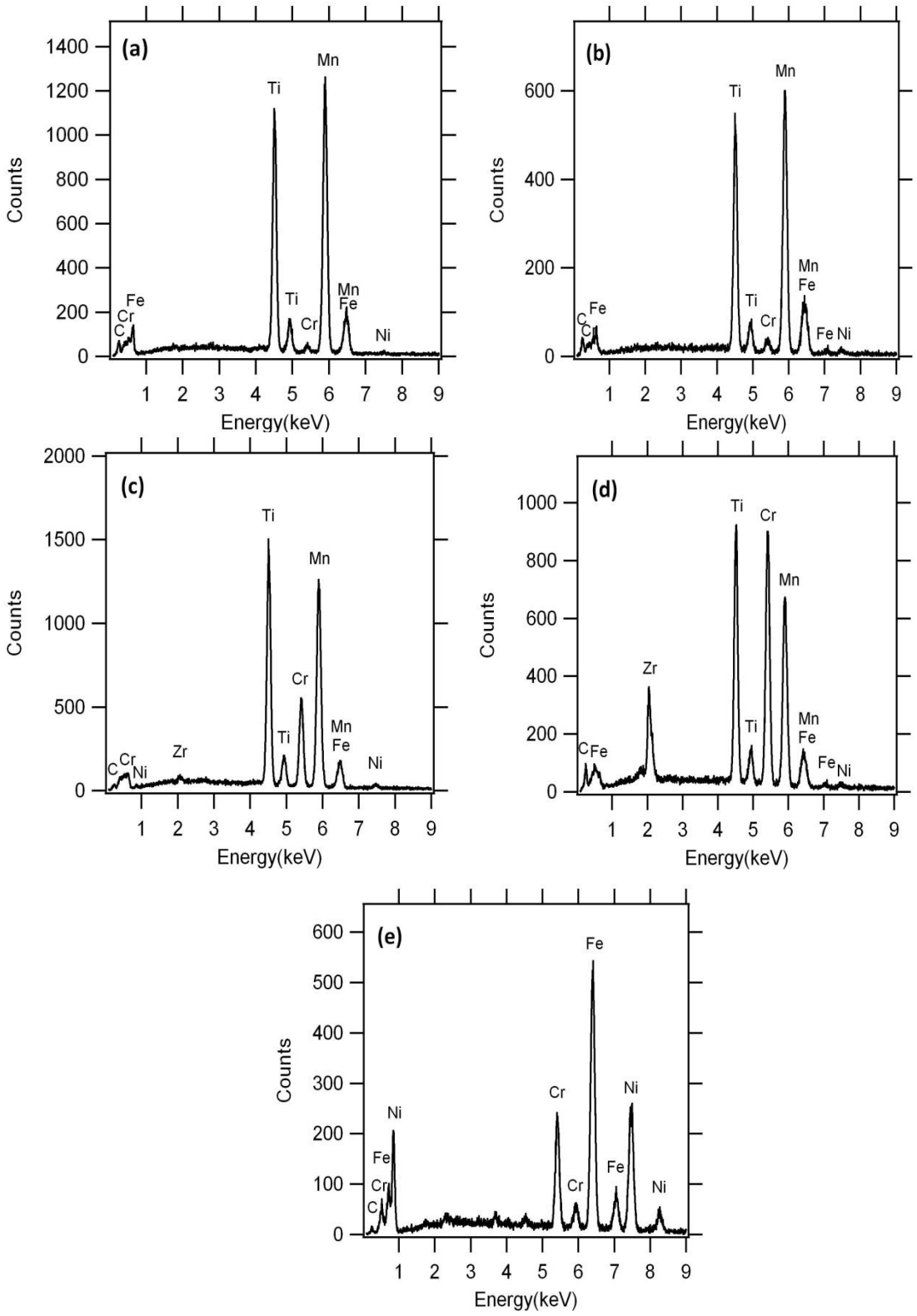

Figure 5- 23.EDS spectra of (a) $TiMn_2$ with BPR 12:1 (b) $TiMn_2$ with BPR 20:1 (c) $Ti_{0.97}Zr_{0.019}Mn_{1.5}Cr_{0.57}$, (d) $Ti_{0.7875}Zr_{0.2625}Mn_{0.8}Cr_{1.2}$ and (e) milling tools.

Table 5-6, 5-7 and 5-8 show the maximum hydrogen wt.% of sample $TiMn_2$, $Ti_{0.97}Zr_{0.019}Mn_{1.5}Cr_{0.57}$ and $Ti_{0.7875}Zr_{0.2625}Mn_{0.8}Cr_{1.2}$ respectively. Before any measurements were undertaken the sample was first evacuated for 1 h at 25°C to remove any adsorbed gas. Activation of the alloy was then undertaken by first introducing 90 - 96 bar of hydrogen into the sample chamber at room temperature for 1 h, followed by an evacuation step. This hydrogen absorption/desorption activation cycle was undertaken 3 times. After completion of the activation process, the residual hydrogen within the sample was removed via evacuation at room temperature for 24 h. Maximum hydrogen absorbed in $TiMn_2$, $Ti_{0.7875}Zr_{0.2625}Mn_{0.8}Cr_{1.2}$and $Ti_{0.97}Zr_{0.019}Mn_{1.5}Cr_{0.57}$ sample were only 0.15 wt.%, 0.19 wt.% and 0.34 wt.% respectively due to impurities phases. It was clear that theoretical value of 1.9 hydrogen wt.% would not be reached by these samples. High energy milling and longer milling time lead to heavy deformation of samples and high oxidisation of sample[56]. It is believed that these crystal deformities and together with impurity phases (oxides, carbides, MnCrZr) both contribute to the low hydrogen weight capacity achieved in these samples.

Table 5- 6:Hydrogen contents in $TiMn_2$ sample using BPR of 20:1.

Cycle	Hydrogen Absorption	Maximum hydrogen wt.%
1	Initial pressure of 96.30 bar was applied at RT for 1 h and the final pressure was 47.98 bar.	0.15
2	Initial pressure of 94.35 bar was applied at RT for 1 h and the final pressure was 47.10 bar.	0.15
3	Initial pressure of 94.68 bar was applied at RT for 1 h and the final pressure was 47.18 bar.	0.12

Table 5- 7:Hydrogen contents in $Ti_{0.97}Zr_{0.019}Mn_{1.5}Cr_{0.57}$ sample.

Cycle	Hydrogen Absorption	Maximum hydrogen wt.%
1	Initial pressure of 96.19 bar was applied at RT for 1 h and the final pressure was 49.29 bar.	0.19
2	Initial pressure of 96.74 bar was applied at RT for 1 h and the final pressure was 49.53 bar.	0.17
3	Initial pressure of 96.88 bar was applied at RT for 1 h and the final pressure was 49.52 bar.	0.18

Table 5- 8:Hydrogen contents in $Ti_{0.7875}Zr_{0.2625}Mn_{0.8}Cr_{1.2}$ sample.

Cycle	Hydrogen Absorption	Maximum hydrogen wt.%
1	Initial pressure of 90.81 bar was applied at RT for 1 h and the final pressure was 42.25 bar.	0.32
2	Initial pressure of 90.65 bar was applied at RT for 1 h and the final pressure was 42.29 bar.	0.34
3	Initial pressure of 90.54 bar was applied at RT for 1 h and the final pressure was 42.12 bar.	0.28

From the hydrogen absorption measurement, the kinetics of the samples (Fig. 5-24) was determined. The kinetics of hydrogen absorption was measured by recording wt.% data at room temperature. It was found that the sample had very fast kinetics, with alloys reaching hydrogen absorption equilibrium within 30 minutes.

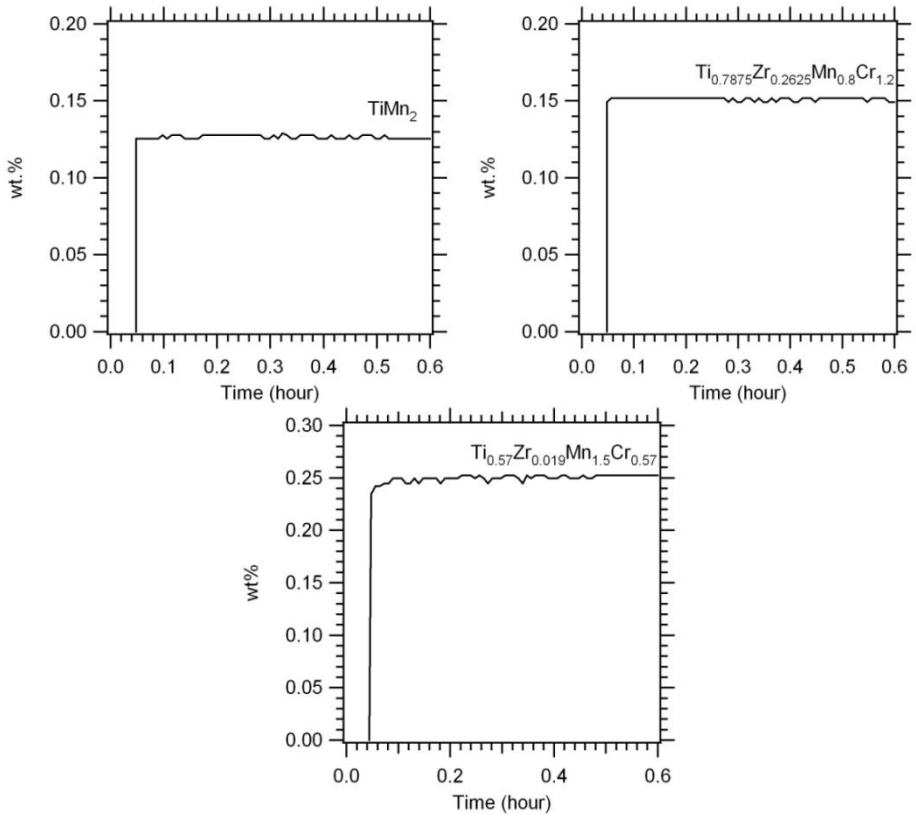

Figure 5- 24.Hydrogenation kinetics on absorption at room temperature for $TiMn_2$, $Ti_{0.7875}Zr_{0.2625}Mn_{0.8}Cr_{1.2}$ and $Ti_{0.97}Zr_{0.019}Mn_{1.5}Cr_{0.57}$ samples after 3 activation cycles.

5.4 Conclusions

5.4.1 TiMn commercial

$TiMn_{1.5}$ type alloy ($Ti_{0.97}Zr_{0.019}V_{0.439}Fe_{0.097}Cr_{0.045}Al_{0.026}Mn_{1.5}$) has been studied. The enthalpy (ΔH) and entropy (ΔS) of hydrogen absorption and desorption have been calculated from a van't Hoff plot as -21.7 ± 0.1 kJ/mol H_2 and -99.8 ± 0.2 J/mol H_2/K for absorption and 25.4 ± 0.1 kJ/mol H_2 and 108.5 ± 0.2 J/mol H_2/K for desorption. The investigation herein provides a detailed analysis of the thermodynamics of one $TiMn_{1.5}$ type alloy in contrast to other studies that often do not provide complete thermodynamic information. SEM results were also provided to demonstrate the microstructural evolution of the $TiMn_{1.5}$ alloy upon hydrogenation cycling to provide insight into the kinetic benefit of hydrogen activation of these alloys.

Typically the $TiMn_{1.5}$ alloy systems present very fast kinetics and adequate equilibrium pressures for room temperature service, and this is also true for the $Ti_{0.97}Zr_{0.019}V_{0.439}Fe_{0.097}Cr_{0.045}Al_{0.026}Mn_{1.5}$ system. The major drawback to the $TiMn_{1.5}$ type alloys is the modest gravimetric hydrogen storage capacity along with the incorporation of a high quantity of high-cost vanadium. However the incorporation of iron in addition to vanadium allows for ferro-vanadium to be used as a starting reagent, dropping the vanadium cost by an order of magnitude.

5.4.2 TiMn mechanical alloying

Ti-Mn alloy compounds with the composition $TiMn_2$, $Ti_{0.97}Zr_{0.019}Mn_{1.5}Cr_{0.57}$ and$Ti_{0.7875}Zr_{0.2625}Mn_{0.8}Cr_{1.2}$ have been synthesised. A nanocrystalline Ti-Mn alloy was formed when the starting reagents were mechanical alloying for 40 h. Then the corresponding crystalline phase TiMn was formed when the amorphous alloy was annealed at 800°C. The addition of PCA leads to the formation of carbide phase (TiC) in the samples. The presence of impurity, carbide (TiC) and oxide (TiO) phases resulted a

decrease in C14 laves phase wt.% in the synthesised samples. Only 37.24, 31.5 and 32.81 wt.% C14 phase was formed in $TiMn_2$, $Ti_{0.97}Zr_{0.019}Mn_{1.5}Cr_{0.57}$ and $Ti_{0.7875}Zr_{0.2625}Mn_{0.8}Cr_{1.2}$ respectively. The result also showed that the theoretical value of 1.9 hydrogen wt.% could not be reached by these samples.

5.5 Future Work

Samples with an oxygen scavenger and an effective PCA that will not react with the starting reagents should be studied. $TiMn_{1.5}$ alloy has been produced by mechanical alloying with the addition of 5 wt.% MgH_2 as a PCA and then annealed at 900°C[218]. This alloy reached 1.67 hydrogen wt.%[218]. MgH_2 produced a high yield of powder after milling process, has a strong affinity to oxygen and does not form any intermetallic compounds with Ti or Mn[218]. The synthesis of this alloy compound by using induction melting should also be considered as less lattice defects are introduced into the Ti-Mn alloy crystal structure and possible less oxygen[66,218].

References

(1) Alternatives, C. o.; Production, S. f. F. H.; Use; Council, N. R.; Engineering, N. A. o. *The Hydrogen Economy: Opportunities, Costs, Barriers, and R&D Needs*; The National Academies Press, 2004.

(2) Andreas Zuttel; Andreas Borgschulte; Schlapbach, L. *Hydrogen as a future energy carrier*; Wiley-vch, 2008.

(3) Larsen, H.; Feidenhans'l, R.; Sonderberg, L. *Hydrogen and its competitors*, RISO Energy Report 3, 2004.

(4) Andrews, J.; Shabani, B. *International Journal of Hydrogen Energy* **2012**, *37*, 1184.

(5) McWhorter, S.; Read, C.; Ordaz, G.; Stetson, N. *Current Opinion in Solid State and Materials Science* **2011**, *15*, 29.

(6) Mahadevan K, J. K., Stone H, Zewatsky J, Thomas A, Mahy H, et al.Identification and Characterization of near-term direct hydrogen proton exchange membrane fuel cell markets. Battelle; 2007. p. 405. <http:// www1.eere.energy.gov/hydrogenandfuelcells/pdfs/pemfc_econ_2006_report_final_0407.pdf> .

(7) Gaines LL, E. A., Wang MQ. Full fuel-cycle comparison of forklift propulsion systems. October 2008. p. 28<http://www1.eere.energy.gov/hydrogenandfuelcells/pdfs/forklift_anl_esd.pdf>.

(8) Vincent B, G. J., Delmont E. 2008 Fuel cell technologies market report. In:Program USDFCT, editor. Washington (DC): US DOE EERE fuel cell technologies program; 2010:<http://www1.eere.energy.gov/hydrogenandfuelcells/pdfs/48219.pdf>.

(9) Dantzer, P. *Materials Science and Engineering A* **2002**, *329-331*, 313.

(10) Sakintuna, B.; Lamari-Darkrim, F.; Hirscher, M. *International Journal of Hydrogen Energy* **2007**, *32*, 1121.

(11) Güther, V.; Otto, A. *Journal of Alloys and Compounds* **1999**, *293*, 889.

(12) Wang, Y.; Chen, K. S.; Mishler, J.; Cho, S. C.; Adroher, X. C. *Applied Energy* **2011**, *88*, 981.

(13) Førde, T.; Eriksen, J.; Pettersen, A. G.; Vie, P. J. S.; Ulleberg, Ø. *International Journal of Hydrogen Energy* **2009**, *34*, 6730.

(14) Hagström, M. T.; Lund, P. D.; Vanhanen, J. P. *International Journal of Hydrogen Energy* **1995**, *20*, 897.

(15) Marangio, F.; Pagani, M.; Santarelli, M.; Calì, M. *International Journal of Hydrogen Energy* **2011**, *36*, 7807.

(16) Santarelli, M.; Medina, P.; Calì, M. *International Journal of Hydrogen Energy* **2009**, *34*, 2519.

(17) Pérez-Herranz, V.; Pérez-Page, M.; Beneito, R. *International Journal of Hydrogen Energy* **2010**, *35*, 912.

(18) Vanhanen, J. P.; Lund, P. D.; Tolonen, J. S. *International Journal of Hydrogen Energy* **1998**, *23*, 267.

(19) Paul, B.; Andrews, J. *International Journal of Hydrogen Energy* **2008**, *33*, 490.

(20) Gray, E. M.; Webb, C. J.; Andrews, J.; Shabani, B.; Tsai, P. J.; Chan, S. L. I. *International Journal of Hydrogen Energy* **2011**, *36*, 654.

(21) http://hhocarfuelcell.blogspot.com.au/2009/04/hydrogen-electrolysis-units.html.

(22) http://www.itpower.co.uk/investire/pdfs/electrolyser.pdf.

(23) http://ec.europa.eu/research/energy/pdf/efchp_hydrogen1.pdf.

(24) http://www.nrel.gov/docs/fy04osti/36705.pdf.

(25) http://en.wikipedia.org/wiki/File:PEM_fuel_cell.svg.

(26) *Fuel Cell System*; Leo J.M.J. Blomen; Mugerwa, M. N., Eds.; Plenum Press: New York, 1993.
(27) Appleby A.J., Y. E. B. *Energy* **1986**, *11* 137.
(28) Corbo, P.; Migliardini, F.; Veneri, O. *Energy Conversion and Management* **2007**, *48*, 2365.
(29) Adamson K-A *Fuel Cell Today* **2009**, *11-2*.
(30) Butler, J. *Fuel Cell Today* **2009**.
(31) Jerram, L. C. *Fuel Cell Today* **2008**.
(32) Jerram, L. C. *Fuel Cell Today* **2009**.
(33) Jain, I. P. *International Journal of Hydrogen Energy* **2009**, *34*, 7368.
(34) Sandrock, G. *Journal of Alloys and Compounds* **1999**, *293*, 877.
(35) David, E. *Journal of Materials Processing Technology* **2005**, *162-163*, 169.
(36) Züttel, A. *Materials Today* **2003**, *6*, 24.
(37) Principi, G.; Agresti, F.; Maddalena, A.; Lo Russo, S. *Energy* **2009**, *34*, 2087.
(38) Klose, W.; Stuke, V. *International Journal of Hydrogen Energy* **1995**, *20*, 309.
(39) M.Paskevicius, Curtin University, 2009.
(40) *Hydrogen in Intermetallic Compounds II, Topics in Applied Physics*; Sandrock, G., S. Suda, L. Schlapbach, Ed.; Springer-Verlag: New York, 1992.
(41) Zaluski, L.; Zaluska, A.; Ström-Olsen, J. O. *Journal of Alloys and Compounds* **1997**, *253-254*, 70.
(42) Hong, C.; Han, D.; Lin, Q. *Journal of The Less-Common Metals* **1991**, *174*, 1044.
(43) Bernauer, O.; Halene, C. *Journal of the Less Common Metals* **1987**, *131*, 213.
(44) Semboshi, S.; Masahashi, N.; Hanada, S. *Acta Materialia* **2001**, *49*, 927.
(45) Semboshi, S.; Masahashi, N.; Hanada, S. *Journal of Alloys and Compounds* **2003**, *352*, 210.
(46) http://www.lme.com/aluminium.asp.
(47) http://www.metalprices.com.
(48) Tjong, S. C.; Chen, H. *Materials Science and Engineering R: Reports* **2004**, *45*.
(49) Pitt, M. P.; Vullum, P. E.; Sørby, M. H.; Blanchard, D.; Sulic, M. P.; Emerich, H.; Paskevicius, M.; Buckley, C. E.; Walmsley, J.; Holmestad, R.; Hauback, B. C. *Journal of Alloys and Compounds* **2012**, *513*, 597.
(50) Vajeeston, P.; Ravindran, P.; Fjellvg, H. *Journal of Alloys and Compounds* **2011**, *509*, S662.
(51) Kelsall, R. W., Hamley, I.W., Geoghegan, M.; John Wiley & Sons, Ltd: West Sussex, 2005.
(52) Kim, K. C.; Dai, B.; Karl Johnson, J.; Sholl, D. S. *Nanotechnology* **2009**, *20*.
(53) Paskevicius, M.; Sheppard, D. A.; Buckley, C. E. *Journal of the American Chemical Society* **2010**, *132*, 5077.
(54) Sandrock, G.; Reilly, J.; Graetz, J.; Zhou, W. M.; Johnson, J.; Wegrzyn, J. *Applied Physics A: Materials Science and Processing* **2005**, *80*, 687.
(55) Tsuzuki, T.; McCormick, P. G. *Journal of Materials Science* **2004**, *39*, 5143.
(56) Suryanarayana, C. *Progress in Materials Science* **2001**, *46*, 1.
(57) Salari, M.; Rezaee, M.; Marashi, S. P. H.; Aboutalebi, S. H. *Powder Technology* **2009**, *192*, 54.
(58) McCormick, P. G.; Tsuzuki, T.; Robinson, J. S.; Ding, J. *Advanced Materials* **2001**, *13*, 1008.
(59) El-Eskandarany, M. S.; William Andrew Publishing/Noyes: 2001.
(60) Achimovičová, M.; Godočíková, E.; Baláž, P.; Kováčč, J.; Šatka, A. *Reviews on Advanced Materials Science* **2008**, *18*, 216.

(61) Lavernia, E. J.; Han, B. Q.; Schoenung, J. M. *Materials Science and Engineering A* **2008**, *493*, 207.
(62) Koch, C. C.; Whittenberger, J. D. *Intermetallics* **1996**, *4*, 339.
(63) Tsuzuki, T.; Ding, J.; McCormick, P. G. *Physica B: Condensed Matter* **1997**, *239*, 378.
(64) Cingi, M. M., O. Guleryuz, H. Baydogan, M. Cimenoglu, H. Kayali, E.S. *MATERIALS SCIENCE FORUM* **2007**, *561/565*, 2179.
(65) Chen, C. C.; Chin, Z. H.; Perng, T. P. *Materials Science and Engineering: A* **1993**, *173*, 381.
(66) Villeroy, B.; Cuevas, F.; Bettembourg, J.; Olier, P.; Latroche, M. *Journal of Physics and Chemistry of Solids* **2006**, *67*, 1281.
(67) Coelho, A. A., Topas User Manual, 3.0 ed. Bruker AXS GmbH, Karlsruhe, Germany, 2003.
(68) Beaucage, G. *Journal of Applied Crystallography* **1995**, *28* 717.
(69) Beaucage, G. *Journal of Applied Crystallography* **1996**, *29*, 134.
(70) Beaucage, G.; Schaefer, D. W. *Journal of Non-Crystalline Solids* **1994**, *172-174*, 797.
(71) Ilavsky, J.; Jemian, P. R. *Journal of Applied Crystallography* **2009**, *42*, 347.
(72) Spalla, O.; Lyonnard, S.; Testard, F. *Journal of Applied Crystallography* **2003**, *36*, 338.
(73) E. Poirer, R. C., A. Tessier, T. K. Bose, Review of Scientific Instruments, 76, 055101 (2005).
(74) Checchetto, R., Trettel, G., and Miotello, A. *Measurement Science and Technology* **2004**, *15* 127.
(75) Sheppard, D. A., Curtin University of Technology, 2008.
(76) *Atkins' Physical Chemistry*; Atkins, P. P., J.d., Ed.; Oxford University Press: Seventh ed. New York, 2002.
(77) http://en.wikipedia.org/wiki/Aluminium.
(78) Li, Q.; Jensen, J. O.; Bjerrum, N. J. In *Encyclopedia of Electrochemical Power Sources*; Editor-in-Chief: Jürgen, G., Ed.; Elsevier: Amsterdam, 2009, p 695.
(79) Suess, H. U., Harold. *Reviews of Modern Physics* **1956**, *28: 53*.
(80) Hetherington, L. E. e. a.; Survey, B. G., Ed. Keyworth, Nottigham, 2007.
(81) Yu, X. In *Bloomberg News* 2009.
(82) http://www.lme.com/aluminium.asp.
(83) http://www.world-aluminium.org/Home.
(84) Lumley, R. *Fundamentals of aluminium metallurgy; production, processing and applications*; Woodhead Publishing Portland, 2011; Vol. 26.
(85) Subiela, J.; García-Jareño, J. J.; Gregori, J.; Agrisuelas, J.; Martí, J. M.; Vicente, F. *Progress in Organic Coatings* **2006**, *57*, 110.
(86) Brousseau, P.; Anderson, C. J. *Propellants, Explosives, Pyrotechnics* **2002**, *27*, 300.
(87) Watson, K. W.; Pantoya, M. L.; Levitas, V. I. *Combustion and Flame* **2008**, *155*, 619.
(88) Chowdhury, M. H.; Ray, K.; Gray, S. K.; Pond, J.; Lakowicz, J. R. *Analytical Chemistry* **2009**, *81*, 1397.
(89) Ray, K.; Chowdhury, M. H.; Lakowicz, J. R. *Analytical Chemistry* **2007**, *79*, 6480.
(90) Medasani, B.; Vasiliev, I. *Surface Science* **2009**, *603*, 2042.
(91) Paskevicius, M.; Webb, J.; Pitt, M. P.; Blach, T. P.; Hauback, B. C.; Gray, E. M.; Buckley, C. E. *Journal of Alloys and Compounds* **2009**, *481*, 595.
(92) Birnbaum, H. K.; Buckley, C.; Zeides, F.; Sirois, E.; Rozenak, P.; Spooner, S.; Lin, J. S. *Journal of Alloys and Compounds* **1997**, *253-254*, 260.
(93) Graetz, J.; Reilly, J. J.; Yartys, V. A.; Maehlen, J. P.; Bulychev, B. M.; Antonov, V. E.; Tarasov, B. P.; Gabis, I. E. *Journal of Alloys and Compounds* **2011**, *509*, S517.
(94) Paskevicius, M.; Sheppard, D. A.; Buckley, C. E. *Journal of Alloys and Compounds* **2009**, *487*, 370.

(95) Konovalov, S. K.; Bulychev, B. M. *Inorganic Chemistry* **1995**, *34*, 172.
(96) Paskevicius, M.; Webb, J.; Pitt, M. P.; Blach, T. P.; Hauback, B. C.; Gray, E. M.; Buckley, C. E. *Journal of Alloys and Compounds* **2009**, *481*, 595.
(97) Jensen, C. M.; McGrady, S.; Program, U. S. D. O. E. H., Ed. 2008.
(98) McGrady, G. S.; HSM System, Inc., Fredericton: 2008.
(99) Chaudhuri, S.; Muckerman, J. T. *Journal of Physical Chemistry B* **2005**, *109*, 6952.
(100) Zhukov, V.; Ferstl, A.; Winkler, A.; Rendulic, K. D. *Chemical Physics Letters* **1994**, *222*, 481.
(101) Yarovsky, I.; Goldberg, A. *Molecular Simulation* **2005**, *31*, 475.
(102) Sinke, G. C.; Walker, L. C.; Oetting, F. L.; Stull, D. R. *The Journal of Chemical Physics* **1967**, *47*, 2759.
(103) Baldé, C. P.; Hereijgers, B. P. C.; Bitter, J. H.; de Jong, K. P. *Angewandte Chemie International Edition* **2006**, *45*, 3501.
(104) Zheng, S.; Fang, F.; Zhou, G.; Chen, G.; Ouyang, L.; Zhu, M.; Sun, D. *Chemistry of Materials* **2008**, *20*, 3954.
(105) Haber, J. A.; Buhro, W. E. *Journal of the American Chemical Society* **1998**, *120*, 10847.
(106) Eckert, J.; Holzer, J. C.; Ahn, C. C.; Fu, Z.; Johnson, W. L. *Nanostructured Materials* **1993**, *2*, 407.
(107) McCarty, R. D.; Standards, U. S. D. O. C. N. B. o., Ed. 1981.
(108) Wai, C. M.; Hunt, F.; Ji, M.; Chen, X. *Journal of Chemical Education* **1998**, *75*, 1641.
(109) Lüdemann, H. D.; Chen, L. *Journal of Physics Condensed Matter* **2002**, *14*, 11453.
(110) Lee, H. M.; Choi, S. Y.; Yun, J. Y. *Advanced Powder Technology* **2011**, *22*, 608.
(111) Baladi, A.; Sarraf Mamoory, R. *Applied Surface Science* **2010**, *256*, 7559.
(112) Kuzmin, P. G.; Shafeev, G. A.; Viau, G.; Warot-Fonrose, B.; Barberoglou, M.; Stratakis, E.; Fotakis, C. *Applied Surface Science* **2011**.
(113) Shiyou Zheng, F. F., Guangyou Zhou, Guorong Chen, Liuzhang Ouyang, Min Zhu and Dalin Sun *Chemical Society Reviews* **2008**, *20*, 3954.
(114) Dodd, A. C.; McCormick, P. G. *Journal of the European Ceramic Society* **2002**, *22*, 1823.
(115) McCormick, P. G.; Tsuzuki, T. 2002; Vol. 386-388, p 377.
(116) Hos, J. P.; McCormick, P. G. *Scripta Materialia* **2003**, *48*, 85.
(117) Li, Y. X.; Chen, W. F.; Zhou, X. Z.; Gu, Z. Y.; Chen, C. M. *Materials Letters* **2005**, *59*, 48.
(118) Eckert, C. A.; Knutson, B. L.; Debenedetti, P. G. *Nature* **1996**, *383*, 313.
(119) Darr, J. A.; Poliakoff, M. *Chemical Reviews* **1999**, *99*, 495.
(120) McHugh, M. A., Krukonis, V. J. *Supercritical Fluid Extraction: Principles & Practice*; Butterworth-Heinemann: Boston, 1994.
(121) Seki, T.; Grunwaldt, J. D.; Baiker, A. *Industrial and Engineering Chemistry Research* **2008**, *47*, 4561.
(122) Rankine, L., Curtin University of Technology, 2009.
(123) Rayner, C. M.; Oakes, R. S.; Sakakura, T.; Yasuda, H. In *Green Reaction Media in Organic Synthesis*; Blackwell Publishing Ltd: 2007, p 125.
(124) M.A. Jacobs, Eindhoven University of Techynology, 2005.
(125) Jessop, P. G.; Ikariya, T.; Noyori, R. *Chemical Reviews* **1999**, *99*, 475.
(126) http://en.wikipedia.org/wiki/Supercritical_carbon_dioxide.
(127) Wang, Q.; Cheng, H.; Liu, R.; Hao, J.; Yu, Y.; Zhao, F. *Catalysis Today* **2009**, *148*, 368.
(128) Zhao, F.; Fujita, S. I.; Sun, J.; Ikushima, Y.; Arai, M. *Catalysis Today* **2004**, *98*, 523.
(129) Zhao, F.; Ikushima, Y.; Chatterjee, M.; Sato, O.; Arai, M. *Journal of Supercritical Fluids* **2003**, *27*, 65.

(130) Sheppard, D. A.; Paskevicius, M.; Buckley, C. E. *Journal of Alloys and Compounds* **2010**, *492*, L72.
(131) Tsuzuki, T.; McCormick, P. G. *Nanostructured Materials* **1999**, *12*, 75.
(132) Maienschein, J. L.; Musket, R. G.; McMurphy, F. E.; Brown, D. W. *Applied Physics Letters* **1987**, *50*, 940.
(133) Yamada-Takamura, Y.; Koch, F.; Maier, H.; Bolt, H. *Surface and Coatings Technology* **2002**, *153*, 114.
(134) Yu, X.; Wu, Z.; Huang, T.; Cheng, J.; Xia, B.; Xu, N. *International Journal of Hydrogen Energy* **2004**, *29*, 81.
(135) Wang, Y.; Pálsson, G. K.; Raanaei, H.; Hjörvarsson, B. *Journal of Alloys and Compounds* **2008**, *464*, L13.
(136) DeLuca, L. T.; Galfetti, L.; Severini, F.; Rossettini, L.; Meda, L.; Marra, G.; D'Andrea, B.; Weiser, V.; Calabro, M.; Vorozhtsov, A. B.; Glazunov, A. A.; Pavlovets, G. J. *Aerospace Science and Technology* **2007**, *11*, 18.
(137) Hua, T. Q.; Ahluwalia, R. K. *International Journal of Hydrogen Energy* **2011**, *36*, 15259.
(138) O. Stecher, E. W. *Ber. Dtsch. Chem. Ges.* **1942**, *75B*, 2003.
(139) Finholt, A. E.; Bond Jr, A. C.; Schlesinger, H. I. *Journal of the American Chemical Society* **1947**, *69*, 1199.
(140) Chizinsky, G.; Evans, G. G.; Gibb Jr, T. R. P.; Rice Jr, M. J. *Journal of the American Chemical Society* **1955**, *77*, 3164.
(141) Brower, F. M.; Matzek, N. E.; Reigler, P. F.; Rinn, H. W.; Roberts, C. B.; Schmidt, D. L.; Snover, J. A.; Terada, K. *Journal of the American Chemical Society* **1976**, *98*, 2450.
(142) Brinks, H. W.; Istad-Lem, A.; Hauback, B. C. *Journal of Physical Chemistry B* **2006**, *110*, 25833.
(143) Paskevicius, M.; Sheppard, D. A.; Buckley, C. E. *Journal of Alloys and Compounds* **2009**, *487*, 370.
(144) Sartori, S.; Istad-Lem, A.; Brinks, H. W.; Hauback, B. C. *International Journal of Hydrogen Energy* **2009**, *34*, 6350.
(145) Sartori, S.; Opalka, S. M.; Løvvik, O. M.; Guzik, M. N.; Tang, X.; Hauback, B. C. *Journal of Materials Chemistry* **2008**, *18*, 2361.
(146) Dodd, A. C.; Tsuzuki, T.; McCormick, P. G. *Materials Science and Engineering A* **2001**, *301*, 54.
(147) Yartys, V. A.; Denys, R. V.; Maehlen, J. P.; Frommen, C.; Fichtner, M.; Bulychev, B. M.; Emerich, H. *Inorganic Chemistry* **2007**, *46*, 1051.
(148) Brinks, H. W.; Langley, W.; Jensen, C. M.; Graetz, J.; Reilly, J. J.; Hauback, B. C. *Journal of Alloys and Compounds* **2007**, *433*, 180.
(149) Brinks, H. W.; Brown, C.; Jensen, C. M.; Graetz, J.; Reilly, J. J.; Hauback, B. C. *Journal of Alloys and Compounds* **2007**, *441*, 364.
(150) Herley, P. J.; Christofferson, O. *Journal of Physical Chemistry* **1981**, *85*, 1887.
(151) Herley, P. J.; Christofferson, O. *Journal of Physical Chemistry* **1981**, *85*, 1882.
(152) Herley, P. J.; Christofferson, O.; Irwin, R. *Journal of Physical Chemistry* **1981**, *85*, 1874.
(153) Herley, P. J.; Christofferson, O.; Todd, J. A. *Journal of Solid State Chemistry* **1980**, *35*, 391.
(154) Herley, P. J.; Irwin, R. H. *Journal of Physics and Chemistry of Solids* **1978**, *39*, 1013.
(155) Sandrock, G.; Reilly, J.; Graetz, J.; Zhou, W. M.; Johnson, J.; Wegrzyn, J. *Journal of Alloys and Compounds* **2006**, *421*, 185.
(156) Graetz, J.; Reilly, J. J. *Journal of Physical Chemistry B* **2005**, *109*, 22181.

(157) Gabis, I.; Dobrotvorskiy, M.; Evard, E.; Voyt, A. *Journal of Alloys and Compounds* **2011**, *509*, S671.
(158) Graetz, J.; Reilly, J. J.; Kulleck, J. G.; Bowman, R. C. *Journal of Alloys and Compounds* **2007**, *446-447*, 271.
(159) Maehlen, J. P.; Yartys, V. A.; Denys, R. V.; Fichtner, M.; Frommen, C.; Bulychev, B. M.; Pattison, P.; Emerich, H.; Filinchuk, Y. E.; Chernyshov, D. *Journal of Alloys and Compounds* **2007**, *446-447*, 280.
(160) Graetz, J.; Reilly, J. J. *Journal of Alloys and Compounds* **2006**, *424*, 262.
(161) Ismail, I. M. K.; Hawkins, T. *Thermochimica Acta* **2005**, *439*, 32.
(162) Turley, J. W.; Rinn, H. W. *Inorganic Chemistry* **1969**, *8*, 18.
(163) *Aluminium: Properties and Physical Metallurgy*; Hatch, J. E., Ed.; American Society for Metals: Metals Park, Ohio, 1984.
(164) Yartys, V. A. **2008**.
(165) Tarasov, V. P.; Muravlev, Y. B.; Bakum, S. I.; Novikov, A. V. *Doklady Physical Chemistry* **2003**, *393*, 353.
(166) B.M. Bulychev, P. A. S., V.N. Fokin *Rus. Chem. Bull. Inter. Ed.* **2009**, *58*.
(167) Wolverton, C.; Ozoliņš, V.; Asta, M. *Physical Review B - Condensed Matter and Materials Physics* **2004**, *69*, 144109.
(168) Ke, X.; Kuwabara, A.; Tanaka, I. *Physical Review B - Condensed Matter and Materials Physics* **2005**, *71*.
(169) Claudy, P.; Bonnetot, B.; Letoffe, J. M. *Journal of Thermal Analysis* **1979**, *15*, 129.
(170) B. Baranowski, M. T. *Zeitschrift fur Physikalische Chemie* **1983**, *135*, 27.
(171) Pundt, A. *Advanced Engineering Materials* **2004**, *6*, 11.
(172) Pundt, A.; Kirchheim, R. 2006; Vol. 36, p 555.
(173) M. Tkacz, S. F., B. Baranowski *Pol. J. Chem.* **1983**, *57*.
(174) M.K. Sakharov, V. E. A., Y.E. Markushkin, A.I. Kolesnikov, I. Natkaniec In *Abtracts of AIRAPT-21* Catania, Italy, 2007, p 202.
(175) Graetz, J. *Chemical Society Reviews* **2009**, *38*, 73.
(176) Qiu, C.; Olson, G. B.; Opalka, S. M.; Anton, D. L. *Journal of Phase Equilibria and Diffusion* **2004**, *25*, 520.
(177) Kobayashi, T.; Kimura, Y.; Suzuki, H.; Sato, T.; Tanigaki, T.; Saito, Y.; Kaito, C. *Journal of Crystal Growth* **2002**, *243*, 143.
(178) Yang, H.; Hu, Y.; Tang, A.; Jin, S.; Qiu, G. *Journal of Alloys and Compounds* **2004**, *363*, 271.
(179) Ao, W.; Li, J.; Yang, H.; Zeng, X.; Ma, X. *Powder Technology* **2006**, *168*, 148.
(180) Sandrock, G.; Reilly, J.; Graetz, J.; Zhou, W. M.; Johnson, J.; Wegrzyn, J. *Applied Physics A: Materials Science & Processing* **2005**, *80*, 687.
(181) Zaluski, L.; Zaluska, A.; Ström-Olsen, J. O. *Journal of Alloys and Compounds* **1997**, *253-254*, 70.
(182) Lü, M. Q.; Zhang, H. F.; Wang, Y. L.; Wei, W. D. *Journal of Alloys and Compounds* **1993**, *191*, 319.
(183) Tarasov, V. P., Muravlev, Y. B., Bakum, S. I., and Novikov, A. V. *Doklady Physical Chemistry* **2003**, *393*, 353.
(184) Stepanov, A.; Ivanov, E.; Konstanchuk, I.; Boldyrev, V. *Journal of The Less-Common Metals* **1987**, *131*, 89.
(185) Easton, D. S.; Schneibel, J. H.; Speakman, S. A. *Journal of Alloys and Compounds* **2005**, *398*, 245.
(186) Xueping, Z.; Shenglin, L. *Journal of Alloys and Compounds* **2009**, *481*, 761.

(187) Senadheera, L.; Carl, E. M.; Ivancic, T. M.; Conradi, M. S.; Bowman Jr, R. C.; Hwang, S. J.; Udovic, T. J. *Journal of Alloys and Compounds* **2008**, *463*, 1.
(188) Bououdina, M.; Grant, D.; Walker, G. *International Journal of Hydrogen Energy* **2006**, *31*, 177.
(189) Hagström, M. T.; Klyamkin, S. N.; Lund, P. D. *Journal of Alloys and Compounds* **1999**, *293*, 67.
(190) Gamo, T.; Moriwaki, Y.; Yanagihara, N.; Yamashita, T.; Iwaki, T. *International Journal of Hydrogen Energy* **1985**, *10*, 39.
(191) Shoemaker, D. P.; Shoemaker, C. B. *Journal of The Less-Common Metals* **1979**, *68*, 43.
(192) Gamo, T.; Moriwaki, Y.; Yanagihara, N.; Iwaki, T. *Journal of The Less-Common Metals* **1982**, *89*, 495.
(193) Moriwaki, Y.; Gamo, T.; Iwaki, T. *Journal of The Less-Common Metals* **1991**, *172-174*, 1028.
(194) Bobet, J. L.; Chevalier, B.; Darriet, B. *Intermetallics* **2000**, *8*, 359.
(195) Bobet, J. L.; Darriet, B. *International Journal of Hydrogen Energy* **2000**, *25*, 767.
(196) Huang, T.; Wu, Z.; Sun, G.; Xu, N. *Intermetallics* **2007**, *15*, 593.
(197) Semboshi, S.; Masahashi, N.; Konno, T. J.; Sakurai, M.; Hanada, S. *Journal of Alloys and Compounds* **2004**, *379*, 290.
(198) Chu, H.; Zhang, Y.; Sun, L.; Qiu, S.; Xu, F.; Yuan, H.; Wang, Q.; Chuang, D. *International Journal of Hydrogen Energy* **2007**, *32*, 3363.
(199) Yu, X. B.; Guo, Y. H.; Yang, Z. X.; Guo, Z. P.; Liu, H. K.; Dou, S. X. *Scripta Materialia* **2009**, *61*, 469.
(200) Singh, B. K.; Singh, A. K.; Imam, A. M.; Srivastava, O. N. *International Journal of Hydrogen Energy* **2001**, *26*, 817.
(201) Klyamkin, S. N.; Verbetsky, V. N.; Demidov, V. A. *Journal of Alloys and Compounds* **1994**, *205*, L1.
(202) Bernauer, O.; Töpler, J.; Noréus, D.; Hempelmann, R.; Richter, D. *International Journal of Hydrogen Energy* **1989**, *14*, 187.
(203) Skripnyuk, V. M.; Ron, M. *International Journal of Hydrogen Energy* **2003**, *28*, 303.
(204) Yukawa, H.; Matsumura, T.; Morinaga, M. *Journal of Alloys and Compounds* **1999**, *293*, 227.
(205) Taizhong, H.; Zhu, W.; Xuebin, Y.; Jinzhou, C.; Baojia, X.; Tiesheng, H.; Naixin, X. *Intermetallics* **2004**, *12*, 91.
(206) Liu, B. H.; Kim, D. M.; Lee, K. Y.; Lee, J. Y. *Journal of Alloys and Compounds* **1996**, *240*, 214.
(207) Yu, X.; Xia, B.; Wu, Z.; Xu, N. *Materials Science and Engineering A* **2004**, *373*, 303.
(208) Au, M.; Pourarian, F.; Sankar, S. G.; Wallace, W. E.; Zhang, L. *Materials Science and Engineering B* **1995**, *33*, 53.
(209) Fang, F.; Li, Y.; Zhang, Q.; Sun, L.; Shao, Z.; Sun, D. *Journal of Power Sources* **2010**, *195*, 8215.
(210) MacDonald, B. D.; Rowe, A. M. *Journal of Power Sources* **2006**, *161*, 346.
(211) Shibuya, M.; Nakamura, J.; Akiba, E. *Journal of Alloys and Compounds* **2008**, *466*, 558.
(212) Xu, Y. H.; Chen, C. P.; Geng, W. X.; Wang, Q. D. *International Journal of Hydrogen Energy* **2001**, *26*, 593.
(213) Murshidi, J. A.; Paskevicius, M.; Sheppard, D. A.; Buckley, C. E. *International Journal of Hydrogen Energy* **2011**, *36*, 7587.
(214) J. J. Reilly, R. H. W. *Inorg. Chem.* **1974**, *13*, 218.
(215) Klyamkin, S. N.; Zakharkina, N. S. *Journal of Alloys and Compounds* **2003**, *361*, 200.

(216) Hagström, M. T.; Vanhanen, J. P.; Lund, P. D. *Journal of Alloys and Compounds* **1998**, *269*, 288.
(217) A. Mahboubi Soufiani ⇑, F. K., M.H. Enayati *Materials and Design* **2012**, *37*, 152.
(218) J. Smith, Curtin University, 2011.

"Every reasonable effort has been made to acknowledge the owners of copyright material. I would be pleased to hear from any copyright owner who has been omitted or incorrectly acknowledged."

Julie Andrianny Murshidi

Signature:

Date: 27st September 2012

APPENDIX A:PUBLISHED PAPER

INTERNATIONAL JOURNAL OF HYDROGEN ENERGY 36 (2011) 7587–7593

Available at www.sciencedirect.com

ScienceDirect

journal homepage: www.elsevier.com/locate/he

Structure, morphology and hydrogen storage properties of a $Ti_{0.97}Zr_{0.019}V_{0.439}Fe_{0.097}Cr_{0.045}Al_{0.026}Mn_{1.5}$ alloy

*J.A. Murshidi, M. Paskevicius, D.A. Sheppard, C.E. Buckley**

Department of Imaging and Applied Physics, Curtin University, GPO Box U 1987, Perth, WA, Australia

ARTICLE INFO

Article history:
Received 9 December 2010
Received in revised form
23 March 2011
Accepted 24 March 2011
Available online 23 April 2011

Keywords:
Hydrogen storage
Laves phase
Thermodynamics
Alloys

ABSTRACT

The $Ti_{0.97}Zr_{0.019}V_{0.439}Fe_{0.097}Cr_{0.045}Al_{0.026}Mn_{1.5}$ alloy is a hexagonal C14 Laves phase material that reversibly stores hydrogen under ambient temperatures. Structural changes are studied by XRD and SEM with regard to hydrogenation and dehydrogenation cycling at 25, 40 and 60 °C. The average particle size is reduced after hydrogenation and dehydrogenation cycling through decrepitation. The maximum hydrogen capacity at 25 °C is 1.71 ± 0.01 wt. % under 78 bar H_2, however the hydrogen sorption capacity decreases and the plateau pressure increases at higher temperatures. The enthalpy (ΔH) and entropy (ΔS) of hydrogen absorption and desorption have been calculated from a van't Hoff plot as −21.7 ± 0.1 kJ/mol H_2 and −99.8 ± 0.2 J/mol H_2/K for absorption and 25.4 ± 0.1 kJ/mol H_2 and 108.5 ± 0.2 J/mol H_2/K for desorption, indicating the presence of a significant hysteresis effect.

Copyright © 2011, Hydrogen Energy Publications, LLC. Published by Elsevier Ltd. All rights reserved.

1. Introduction

There are currently concerns about the impact that fossil fuels have on the environment and their increasing price to the consumer. These concerns have led to research being undertaken to investigate other energy carriers that will be comparable to fossil fuels. Significant interest has been associated with hydrogen [1]. Hydrogen can be produced using abundant and diverse domestic resources including fossil sources, biological methods, renewable energy sources and nuclear energy. A range of different approaches have been suggested to effectively store hydrogen including storage as a pressurized gas, cryogenic liquid and also solid state options. These solid state solutions include chemical or physical combination of hydrogen with materials such as metal hydrides, complex hydrides and carbon materials. Among the different hydrogen storage systems, metal hydrides are most attractive due to their high volumetric energy densities and in some cases their favourable heat of formation that allows reversible hydrogen storage at ambient temperatures.

Much research has been undertaken to investigate the hydrogen storage properties of various types of metal hydride families such as Mg-based systems, BCC alloys and intermetallic systems (AB, AB_2 (Laves phase), AB_3 and AB_5) [1,2]. Intermetallic systems often consist of a stable hydride forming element with an element forming a nonstable hydride. In these systems the A elements are usually Ti, Zr, Hf, Th or a lanthanide, whilst the B elements can be a variety of transition and non-transition metals.

Research on intermetallic compounds for hydrogen storage has been ongoing for approximately 40 years. However, at the present time they do not satisfy the requirements for mobile storage due to low gravimetric storage

* *Corresponding author*. Tel.: +61 8 92663532; fax: +61 8 92662377.
E-mail address: C.Buckley@curtin.edu.au (C.E. Buckley).
0360-3199/$ – see front matter Copyright © 2011, Hydrogen Energy Publications, LLC. Published by Elsevier Ltd. All rights reserved.
doi:10.1016/j.ijhydene.2011.03.137

capacities (<2 wt.%) and often high material cost. The storage capacity limitation is less important for stationary storage applications including thermodynamic devices (refrigerator and air conditioner) and energy storage units in remote regions. In addition, there are no weight problems in using heavy hydrogen storage tanks if hydrogen is used as a future fuel or fuel additive for sea transportation (because the extra weight can be used to provide ballast to keep the ship stable). An inexpensive intermetallic system with the requisite sorption pressure at a desired temperature with adequate kinetics has the potential to be a hydrogen storage material for these markets [2].

Among the intermetallic systems for hydrogen storage, $TiMn_2$ based Laves phase alloys have attracted attention due to their easy activation, modest hydrogen sorption temperature, rapid kinetics and low cost [3,4]. The hydrogen storage capacity of $TiMn_2$ alloys is reasonably modest compared to other metal hydrides but is higher than 1.0 H/M (hydrogen per metal formula unit) [5,6] making it suitable for many static hydrogen storage applications. If weight is not an issue, then there are two main factors to consider, the cost of the hydride, and its long term stability (cycling properties). The $Ti_{0.97}Zr_{0.019}V_{0.439}Fe_{0.097}Cr_{0.045}Al_{0.026}Mn_{1.5}$ alloy contains relatively inexpensive elements, with the exception of vanadium, however ferro-vanadium (V with Fe impurity) is an order of magnitude less expensive than pure vanadium. Thus, having a hydrogen storage alloy with V and Fe components allows for a reduced system cost. The addition of elemental additives to the $TiMn_2$ system is required to enhance its hydrogenation and dehydrogenation cycling properties for long term use [7]. There are other problems with Ti–Mn alloys including their comparatively high equilibrium plateau pressure (between 0.8 MPa and 1.2 MPa) under near ambient temperatures and the fact that these alloys possess a large sorption pressure hysteresis effect [6,8] during hydrogen cycling. In order to reduce these disadvantages, research has been undertaken on altering $TiMn_2$ alloys by partial substitution of Ti or/and Mn with other elements [8–11], by using different $TiMn_2$ composition/stoichiometries [6,12] or through catalysed $TiMn_2$ alloys [13,14]

In this study, the $Ti_{0.97}Zr_{0.019}V_{0.439}Fe_{0.097}Cr_{0.045}Al_{0.026}Mn_{1.5}$ alloy was characterized with respect to its structure, morphology and hydriding properties in order to understand the effect of substituting Zr for the Ti site and V, Fe, Cr and Al for the Mn site within Ti–Mn alloy.

2. Experimental

The $Ti_{0.97}Zr_{0.019}V_{0.439}Fe_{0.097}Cr_{0.045}Al_{0.026}Mn_{1.5}$ alloy was investigated as-supplied without further alteration from Sigma–Aldrich Australia. The lattice parameter of the alloy before and after hydrogenation was determined by X-Ray Diffraction (XRD) using a Bruker D8 Advance diffractometer (CuK_α radiation) with a 2θ range of 30–100° using 0.02° steps and a 0.8 s count time per step with operating conditions of 40 kV and 40 mA. Samples were loaded into XRD low background sample holders in an argon glove box and sealed within a poly(methylmethacrylate) (PMMA) air-tight holder to prevent oxygen/moisture contamination during data collection. The structural parameters were refined from the diffraction data using Rietveld refinement in TOPAS (Bruker AXS, Karlsruhe, Germany) via a fundamental parameters approach.

Microstructural observations of as-received and hydrogen cycled alloys were conducted on a Philips XL-30 Scanning Electron Microscopy (SEM) using a secondary electron detector operating at 15 keV. The microscope was coupled with an Oxford Instruments energy dispersive X-Ray spectrometer (EDS) for elemental analysis. Samples were briefly (<1–2 min) exposed to air and were not coated with gold prior to imaging in the SEM.

The hydrogen sorption properties of the alloy were determined using a custom-built automated Sieverts apparatus (details can be found elsewhere [15]). Before any measurements were undertaken the sample was first evacuated for 1 h at 25 °C to remove any adsorbed gas. Activation of the alloy was then undertaken by first introducing 50 bar of hydrogen into the sample chamber at room temperature for 1 h, followed by an evacuation step. This hydrogen absorption/desorption activation cycle was undertaken 3 times. After completion of the activation process, the residual hydrogen within the sample was removed via evacuation at room temperature for 24 h. The pressure-composition isotherm (PCI) measurements were subsequently performed at 25, 40 and 60 °C while being careful to verify that the sample was at a true hydrogen equilibrium at each collected data point.

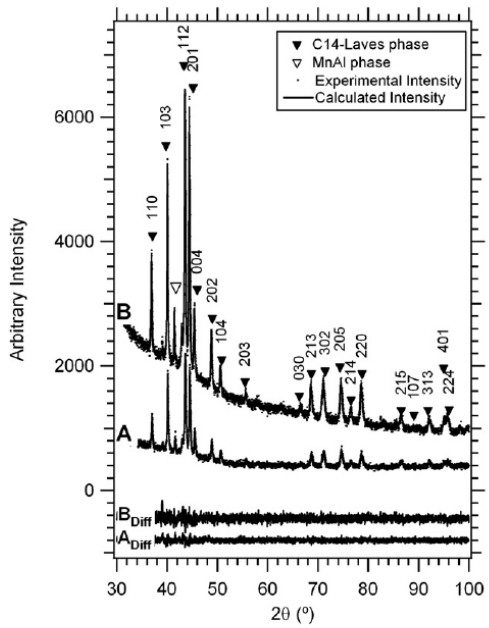

Fig. 1 – X-Ray Diffraction (XRD) of $Ti_{0.97}Zr_{0.019}V_{0.439}Fe_{0.097}Cr_{0.045}Al_{0.026}Mn_{1.5}$: (a) as-received and (b) after absorption and desorption at 25, 40 and 60 °C. Rietveld fits to the data are also displayed along with difference plots.

Table 1 – Unit cell parameters of $Ti_{0.97}Zr_{0.019}V_{0.439}$

	a (nm)	*c* (nm)	V (nm^3)
Unhydrided	0.4861 ± 0.0001	0.7966 ± 0.0002	0.1630 ± 0.0001
After multiple hydrogenation and dehydrogenation cycles	0.4869 ± 0.0001	0.7981 ± 0.0001	0.1639 ± 0.0001
$TiMn_2$ C14 Laves phase PDF No. 07-0133	0.4825	0.7917	0.1596

3. Results and discussion

3.1. X-Ray diffraction (XRD) analysis

X-ray diffraction (XRD) data was collected on the $Ti_{0.97}Zr_{0.019}V_{0.439}Fe_{0.097}Cr_{0.045}Al_{0.026}Mn_{1.5}$ alloy before and after hydrogen sorption measurements were undertaken as shown in Fig. 1(a) and (b). The alloy was indexed as a hexagonal C14 Laves phase ($P6_3/mmc$ space group) as shown in Fig. 1. A single peak in the alloy sample pattern at $2\theta = 42.0°$ was indexed to MnAl phase. The diffraction data was further analysed using the Rietveld method to determine the lattice parameters before and after hydrogenation and dehydrogenation as listed in Table 1.

Hydrogen atoms are stored at interstitial sites in the host metal lattice during the absorption process. This causes the lattice to expand and lose some of its symmetry. The co-existence of the non-expanded solid solution phase and anisotropically expanded hydride phase, gives rise to lattice defects and internal strain, ultimately causing the decrepitation of the brittle host metals. For $Ti_{0.97}Zr_{0.019}V_{0.439}Fe_{0.097}Cr_{0.045}Al_{0.026}Mn_{1.5}$ the calculated crystallite size is found to slightly increase from 33 ± 1 nm to 39 ± 1 nm after multiple cycles of hydrogenation and dehydrogenation however the particle size was found to significantly decrease as discussed in the following section. The stored hydrogen atoms within the absorbed sample are later released during the desorption process [16,17], and for $Ti_{0.97}Zr_{0.019}V_{0.439}Fe_{0.097}Cr_{0.045}Al_{0.026}Mn_{1.5}$ the hydrogen is desorbed from the material under ambient pressure and temperature. Therefore lattice expansions cannot be detected using ex-situ XRD as the sample cannot be analysed in the hydride state. It should be noted that it is possible to perform ex-situ XRD on hydrided alloys but they need to be kinetically stable so that they don't desorb hydrogen, often requiring them to be first oxidised [18].

From the XRD results provided in Fig. 1 and Table 1 it is apparent that there is no structural change after hydrogenation and dehydrogenation cycling. However, an expansion of the crystal lattice for $Ti_{0.97}Zr_{0.019}V_{0.439}Fe_{0.097}Cr_{0.045}Al_{0.026}Mn_{1.5}$ is found to be larger than for pure $TiMn_2$ due to the incorporation of substituted elements as shown in Table 1.

3.2. Microstructure

The microstructure of the $Ti_{0.97}Zr_{0.019}V_{0.439}Fe_{0.097}Cr_{0.045}Al_{0.026}Mn_{1.5}$ alloy was investigated using scanning electron microscopy (SEM) before and after hydrogenation and dehydrogenation cycling. SEM micrographs are showed in Fig. 2 (a) for the as-received alloy and Fig. 2 (b) and (c) for particles after hydrogenation and dehydrogenation cycling. The average particle size before hydrogen sorption is 50–200 μm. After the sample is cycled multiple times with hydrogen the particle size decreases to generally less than 20 μm and the fractured particle surfaces appear to consist of smooth crystallographic facets. According to previous studies, Ti–Mn alloys are rapidly pulverized into fine powder only by the first hydrogenation cycle and the subsequent hydrogenation cycles result in a slow pulverization process [6,16]. During the first hydrogenation cycle, hydrogen introduces strain into the alloy surface and when the strain reaches a critical value for cracking, spalling occurs at the surface. The freshly created surfaces provide larger surface area and shorter distances for H to diffuse. These factors bring about rapid hydrogen sorption kinetics. This decrepitating process occurs to some degree with each hydrogenation cycle and can lead to internal cleavage fractures in the particles as seen in Fig. 2 (c). During the SEM investigations energy dispersive spectroscopy (EDS) was undertaken to verify the elemental composition of the alloy. The EDS results (Fig. 3) are compared to inductively coupled plasma (ICP) results reported by Sigma–Aldrich in Table 2. It is evident that the composition of the alloy is consistent between analysis techniques and as such the elemental composition $Ti_{0.97}Zr_{0.019}V_{0.439}Fe_{0.097}Cr_{0.045}Al_{0.026}Mn_{1.5}$ is accurate.

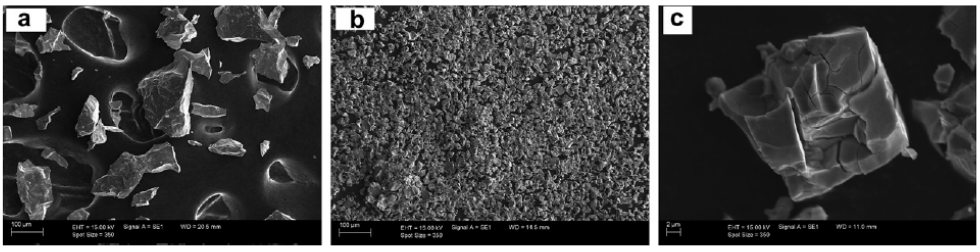

Fig. 2 – (a) SEM of the as-received $Ti_{0.97}Zr_{0.019}V_{0.439}Fe_{0.097}Cr_{0.045}Al_{0.026}Mn_{1.5}$ alloy and (b & c) after hydrogenation cycling.

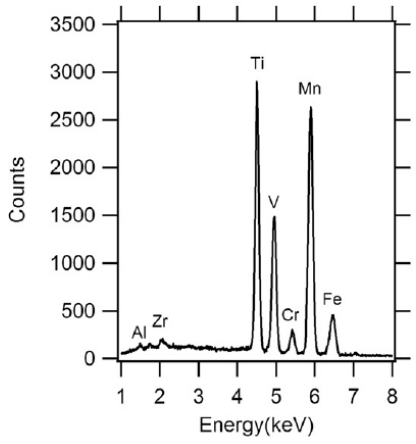

Fig. 3 – EDS spectra of $Ti_{0.97}Zr_{0.019}V_{0.439}Fe_{0.097}Cr_{0.045}Al_{0.026}Mn_{1.5}$ alloy.

3.3. Hydrogen sorption

Hydrogen sorption pressure-composition isotherms (PCI's) at 25, 40 and 60 °C are shown in Fig. 4. Each data point is the result of a kinetic sorption measurement until hydrogen equilibrium is achieved. The size of the plateau region decreases as a function of temperature. With increasing sorption temperature from 25 °C, 40 °C to 60 °C, the amount of absorbed hydrogen decreases from 1.71 ± 0.01 wt.%, 1.56 ± 0.01 wt.% and 1.43 ± 0.01 wt.% respectively. The maximum hydrogen storage capacity at room temperature (1.71 wt.%) is lower than for the pure $TiMn_{1.5}$ system (1.86 wt.%) [6]. This is likely due to the presence of a MnAl impurity phase within the $Ti_{0.97}Zr_{0.019}V_{0.439}Fe_{0.097}Cr_{0.045}Al_{0.026}Mn_{1.5}$ commercial alloy that does not react sufficiently with hydrogen. The hysteresis factor, defined as $\ln P_{abs}/P_{des}$, for $Ti_{0.97}Zr_{0.019}V_{0.439}Fe_{0.097}Cr_{0.045}Al_{0.026}Mn_{1.5}$ was also found to be a function of temperature as shown in Table 3. Both the absorption and desorption plateaus increased with increasing temperature and this feature along with the hydrogen capacity and hysteresis result conform to the classic behaviour of metal-hydride systems [8,20].

The kinetics of hydrogen absorption and desorption were measured by recording pressure data at the different temperatures at which PCIs were collected. Fig. 5(a) and (b) show the kinetic curves for absorption and desorption, respectively, at the midpoint of the plateau. The sorption kinetics show that the alloy reaches a hydrogen sorption equilibrium within 15 min.

Table 2 – Elemental composition of alloy.

Element	ICP (Sigma–Aldrich) wt.%	EDS (SEM) wt.%
Mn	50.9	50.2 ± 0.33
Ti	28.7	29.3 ± 0.26
V	13.8	13.6 ± 0.22
Fe	3.35	3.51 ± 0.21
Cr	1.45	1.45 ± 0.15
Zr	1.10	1.36 ± 0.22
Al	0.43	0.45 ± 0.07

The enthalpy (ΔH) and entropy (ΔS) of hydrogen desorption can be calculated from the van't Hoff equation:

$$\ln\left(\frac{f_{H2}}{f_0}\right) = \frac{\Delta H}{RT} - \frac{\Delta S}{R} \quad (1)$$

where f_{H2} is the hydrogen fugacity corresponding to the absorption or desorption plateau pressures (see elsewhere for more information [15]). The van't Hoff plot provided in Fig. 6 was constructed from the absorption/desorption pressure of the PCI curves (Fig. 4) at a wt.% of 0.9–1.0 according to Eq. (1). This allows for the hydride formation (absorption) and decomposition (desorption) thermodynamics (ΔH and ΔS) to be determined using a weighted least-squares method from the fit in the van't Hoff plot ($\ln f$ versus $1/T$). The calculated ΔH and ΔS values are provided in Table 4 in comparison to other similar Ti–Mn systems in the literature.

As the Ti content increases within a Ti–Mn alloy, the amount of absorbed H increases uniformly. At a Ti content of 37 at.%, there is a sudden increase of the amount of absorbed H indicating that there is a minimum lattice constant required to absorb a large amount of H within the Laves phase structure

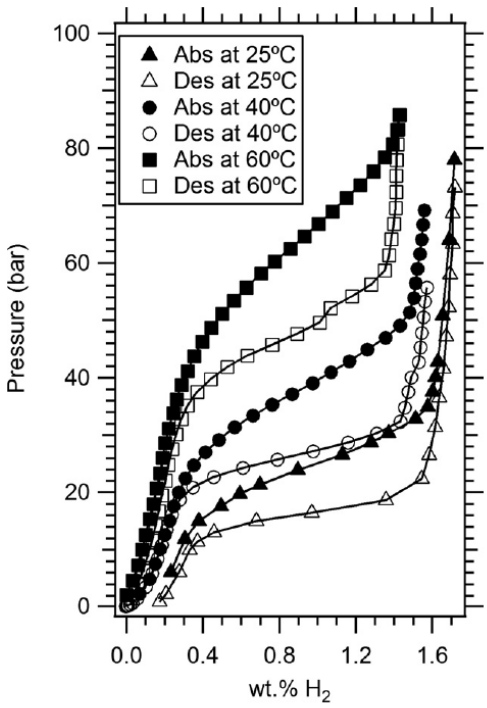

Fig. 4 – PCI curves of the $Ti_{0.97}Zr_{0.019}V_{0.439}Fe_{0.097}Cr_{0.045}Al_{0.026}Mn_{1.5}$ alloy for hydrogen absorption and desorption at 25, 40 and 60 °C.

Table 3 – Hydrogen sorption properties of $Ti_{0.97}Zr_{0.019}V_{0.439}Fe_{0.097}$

Temperature (°C)	Maximum Capacity (wt.% H_2)	Plateau Pressure		
		P_{Abs} (bar)	P_{Des} (bar)	Hysteresis $\ln P_{abs}/P_{des}$
25	1.71 ± 0.01 at 78 bar	25.20 ± 0.03	16.15 ± 0.02	0.445 ± 0.002
40	1.56 ± 0.01 at 69 bar	39.01 ± 0.03	27.05 ± 0.04	0.366 ± 0.002
60	1.43 ± 0.01 at 86 bar	62.70 ± 0.04	47.06 ± 0.09	0.287 ± 0.003

[6]. The amount of desorbed H also increases until the Ti content reaches about 40 at.% ($TiMn_{1.5}$). At this concentration the amount of desorbed H then decreases [6]. This may be due to the β-Ti phase existing within high Ti-content alloys, forming a very stable hydride where most of absorbed H is trapped within titanium. Therefore $TiMn_{1.5}$ shows the most desirable properties as hydrogen storage material. The maximum absorbed hydrogen reported for the pure $TiMn_{1.5}$ system is 1.86 wt.% and the maximum desorbed hydrogen is 1.53 wt.% [6]. This data demonstrates that the $TiMn_{1.5}$ system contains hydrogen even after desorption at 20 °C. The partial substitution of Ti and/or Mn with other elements in the $TiMn_{1.5}$ system has been studied in multiple variations such as Ti–Mn ternary ($Ti_{1-x}Zr_xMn$), quaternary ($Ti_{1-x}Zr_xMn_{2-y}B_y$) and quinary ($Ti_{1-x}Zr_xMn_{2-y-z}B_yC_z$) systems [9,21,22]. With increasing substitution, the lattice constant increases which leads to a decrease of both the plateau pressure and the hysteresis in conjunction with an increased hydrogen capacity [6,10].

For the $Ti_{1-x}Zr_xMn$ system, the increase in x (Zr content) results in a decrease of the quantity of desorbed hydrogen despite an increase in the absorbed hydrogen [6,23]. Both the absorption and desorption plateau pressure decrease with the increase of Zr in the system. The reason for the increase in the quantity of absorbed hydrogen is that Zr has a stronger affinity for hydrogen and larger metallic radius than Ti whilst the decrease in desorbed hydrogen is related to the stability of titanium hydride [24]. The plateau pressure of Zr hydride is lower than Ti hydride. Therefore Zr hydride is more stable than Ti hydride. As a result, a high Zr content results in difficulties with hydrogen desorption from the Ti–Mn system. For the $Ti_{1-x}Zr_xMn_{2-y}B_y$ system, where B is any element, as x (Zr content) increases or y (substituted element content) decreases, the dissociation pressure decreases due to a larger lattice constant and provides an increased hydrogen absorption capacity. The influence of the substitution for Mn by other elements was correlated with the metallic radius and the affinity with H of the substitution elements [8,9]. In the case of Al and V substitution, the metallic radius was larger than that of Mn, so the lattice constant increased and the plateau pressure was reduced. In the case of Fe, the metallic radius is smaller than Mn, therefore the lattice constant decreased and the plateau pressure increased. However in the case of Cr, the lattice constant increases slightly even though the metallic radius is almost the same as that of Mn. The residual hydrogen is also less of a problem in this system compared to $TiMn_{1.5}$ and $TiMn_{2-y}B_y$ systems [6]. As for the $Ti_{1-x}Zr_xMn_{2-y-z}B_yC_z$

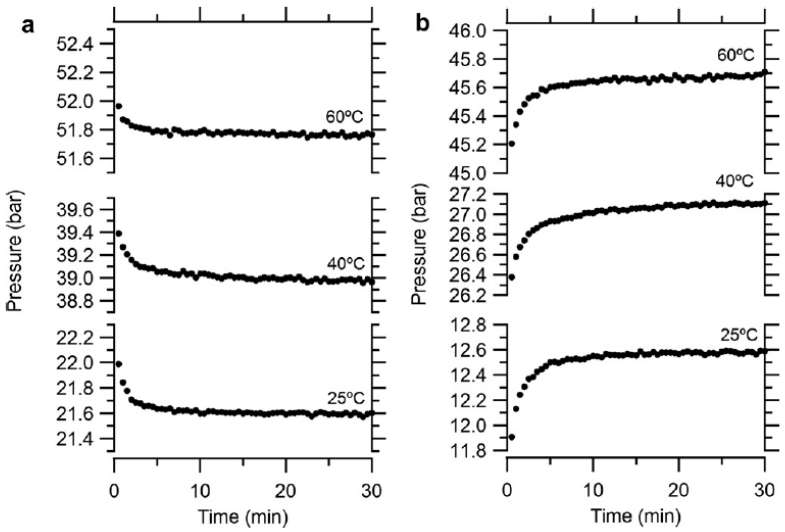

Fig. 5 – Hydrogenation kinetics on (a) absorption and (b) desorption at different temperatures in $Ti_{0.97}Zr_{0.019}V_{0.439}Fe_{0.097}Cr_{0.045}Al_{0.026}Mn_{1.5}$.

Table 4 – Comparison of ΔH and ΔS values of several Ti–Mn alloy systems.

System	Absorption		Desorption			
	ΔH (kJ/mol H_2)	ΔS (J/mol H_2/K)	ΔH (kJ/mol H_2)	ΔS (J/mol H_2/K)	1 bar desorption equilibrium temperature (°C)	Calculated P_{Des} at 20 °C (bar)
A: $Ti_{0.97}Zr_{0.019}V_{0.439}Fe_{0.097}Cr_{0.045}Al_{0.026}Mn_{1.5}$	−21.7 ± 0.1	−99.8 ± 0.2	25.4 ± 0.1	108.5 ± 0.2	−39.0 ± 0.5	13.9 ± 0.3
B: $Ti_{0.98}Zr_{0.02}V_{0.43}Fe_{0.09}Cr_{0.05}Mn_{1.5}$ [19]	–	–	27.4	112.0	−28.5	9.29
C: $Ti_{0.98}Zr_{0.02}V_{0.41}Fe_{0.08}Cr_{0.05}Mn_{1.46}$[20]	–	–	29.2	121.2	−32.2	13.42
D: $Ti_{0.95}Zr_{0.05}V_{0.43}Fe_{0.08}Al_{0.01}Mn_{1.48}$ [20]	−25.6	–	29.4	106.5	2.9	2.11
E: $Ti_{0.955}Zr_{0.045}V_{0.43}Fe_{0.12}Al_{0.03}Mn_{1.52}$ [20]	–	–	28.7	116.9	−27.6	9.82

*Experimental P_{Des} reported for system C ($Ti_{0.98}Zr_{0.02}V_{0.41}Fe_{0.08}Cr_{0.05}Mn_{1.46}$) and D ($Ti_{0.95}Zr_{0.05}V_{0.43}Fe_{0.08}Al_{0.01}Mn_{1.48}$) are 6.5 bar and 3.4 bar respectively.

systems, where B and C are different elements, these compositions have been studied to further improve the properties of $Ti_{1-x}Zr_xMn_{2-y}B_y$ systems, where the type of elements used (C) can further alter the properties of the Ti–Mn system to optimise the properties of the hydrogen storage material [21,22].

From Table 4, it shown that the increase in Zr content results in a decrease in equilibrium pressure and the introduction of V, Cr and Al leads to further reduction in the hydrogen equilibrium pressure of these alloy systems. The plateau pressure of system A ($Ti_{0.97}Zr_{0.019}V_{0.439}Fe_{0.097}Cr_{0.045}Al_{0.026}Mn_{1.5}$), B ($Ti_{0.98}Zr_{0.02}V_{0.43}Fe_{0.09}Cr_{0.05}Mn_{1.5}$) and E ($Ti_{0.955}Zr_{0.045}V_{0.43}Fe_{0.12}Al_{0.03}Mn_{1.52}$) are 13.9 ± 0.3, 9.29 and 9.82 bar respectively at 20 °C. For both system C ($Ti_{0.98}Zr_{0.02}V_{0.41}Fe_{0.08}Cr_{0.05}Mn_{1.46}$) and D ($Ti_{0.95}Zr_{0.05}V_{0.43}Fe_{0.08}Al_{0.01}Mn_{1.48}$) the experimental equilibrium pressures do not match the pressures calculated from the thermodynamic properties. The discrepancy between the calculated and measured equilibrium pressures indicates that the reported thermodynamic data is not appropriate for these systems. The differences in composition between the alloys in Table 4 obviously lead to changes in the hydrogen sorption behaviour.

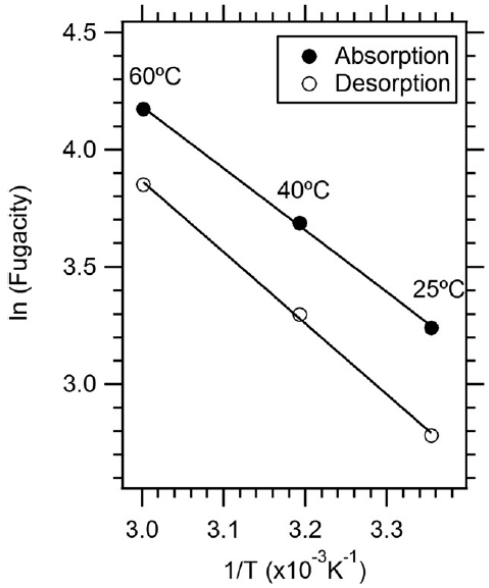

Fig. 6 – van't Hoff plot for the $Ti_{0.97}Zr_{0.019}V_{0.439}Fe_{0.097}Cr_{0.045}Al_{0.026}Mn_{1.5}$ alloy.

4. Conclusions

We have studied a $TiMn_{1.5}$ type alloy ($Ti_{0.97}Zr_{0.019}V_{0.439}Fe_{0.097}Cr_{0.045}Al_{0.026}Mn_{1.5}$). The enthalpy (ΔH) and entropy (ΔS) of hydrogen absorption and desorption have been calculated from a van't Hoff plot as −21.7 ± 0.1 kJ/mol H_2 and −99.8 ± 0.2 J/mol H_2/K for absorption and 25.4 ± 0.1 kJ/mol H_2 and 108.5 ± 0.2 J/mol H_2/K for desorption. The investigation herein provides a detailed analysis of the thermodynamics of one $TiMn_{1.5}$ type alloy in contrast to other studies that often do not provide complete thermodynamic information. SEM results were also provided to demonstrate the microstructural evolution of the $TiMn_{1.5}$ alloy upon hydrogenation cycling to provide insight into the kinetic benefit of hydrogen activation of these alloys.

Typically $TiMn_{1.5}$ alloy systems present very fast kinetics and adequate equilibrium pressures for room temperature service, and this is also true for the $Ti_{0.97}Zr_{0.019}V_{0.439}Fe_{0.097}Cr_{0.045}Al_{0.026}Mn_{1.5}$ system. The major drawback to the $TiMn_{1.5}$ type alloys is the modest gravimetric hydrogen storage capacity along with the incorporation of a high quantity of

high-cost vanadium. However the incorporation of iron in addition to vanadium allows for ferro-vanadium to be used as a starting reagent, dropping the vanadium cost by an order of magnitude.

Acknowledgements

J.A.M. would like to thank E. Miller and W. Rickard at Curtin University for their technical assistance during SEM investigations. J.A.M thanks the Malaysian Government for a Ph.D. Scholarship. C.E.B. acknowledges the financial support of the Australian Research Council through a 2007 LEIF grant LE0775551, which enabled the XRD studies to be undertaken, and the International Aluminum Institute (IAI) for financial support. D.A.S thanks Curtin University for funding from a Curtin Strategic Research Grant.

REFERENCES

[1] Sakintuna B, Lamari-Darkrim F, Hirscher M. Metal hydride materials for solid hydrogen storage: a review. Int J Hydrogen Energy 2007;32:1121–40.
[2] Dantzer P. Properties of intermetallic compounds suitable for hydrogen storage applications. Mater Sci Eng A 2002;329-331:313–20.
[3] Bououdina M, Grant D, Walker G. Review on hydrogen absorbing materials–structure, microstructure, and thermodynamic properties. Int J Hydrogen Energy 2006;31:177–82.
[4] Hagström MT, Klyamkin SN, Lund PD. Effect of substitution on hysteresis in some high-pressure AB_2 and AB_5 metal hydrides. J Alloys Compd 1999;293-295:67–73.
[5] Shoemaker DP, Shoemaker CB. Concerning atomic sites and capacities for hydrogen absorption in the AB_2 Friauf-Laves phases. J Less-Common Met 1979;68:43–58.
[6] Gamo T, Moriwaki Y, Yanagihara N, Yamashita T, Iwaki T. Formation and properties of titanium-manganese alloy hydrides. Int J Hydrogen Energy 1985;10:39–47.
[7] Gamo T, Moriwaki Y. Yanagihara NIwaki, T. Life properties of Ti-Mn alloy hydrides and their hydrogen purification effect. J Less-Common Met 1983;89:495–504.
[8] Moriwaki Y, Gamo T, Iwaki T. Control of hydrogen equilibrium pressure for C14-type laves phase alloys. J Less-Common Met 1991;172-174:1028–35.
[9] Bobet JL, Chevalier B, Darriet B. Crystallographic and hydrogen sorption properties of $TiMn_2$ based alloys. Intermetallics 2000;8:359–63.
[10] Bobet JL, Darriet B. Relationship between hydrogen sorption properties and crystallography for $TiMn_2$ based alloys. Int J Hydrogen Energy 2000;25:767–72.
[11] Huang T, Wu Z, Sun G. Xu. Microstructure and hydrogen storage characteristics of $TiMn_{2-x}V_x$ alloys. Intermetallics 2007;15:593–8.
[12] Semboshi S, Masahashi N, Konno TJ, Sakurai M, Hanada S. Composition dependence of hydrogen absorbing properties in melt quenched and annealed $TiMn_2$ based alloys. J Alloys Compd 2004;379:290–7.
[13] Chu H, Zhang Y, Sun L, Qiu S, Xu F, Yuan H, et al. Structure, morphology and hydrogen storage properties of composites prepared by ball milling $Ti_{0.9}Zr_{0.2}Mn_{1.5}Cr_{0.3}V_{0.3}$ with La-Mg-based alloy. Int J Hydrogen Energy 2007;32:3363–9.
[14] Yu XB, Guo YH, Yang ZX, Guo ZP, Liu HK, Dou SX. Synthesis of catalyzed magnesium hydride with low absorption/desorption temperature. Scr Mater 2009;61:469–72.
[15] Paskevicius M, Sheppard DA, Buckley CE. Thermodynamic changes in Mechanochemically Synthesized magnesium hydride Nanoparticles. J Am Chem Soc 2010;132:5077–83.
[16] Semboshi S, Masahashi N, Hanada S. Degradation of hydrogen absorbing capacity in cyclically hydrogenated $TiMn_2$. Acta Mater 2001;49:927–35.
[17] Semboshi S, Masahashi N, Hanada S. Effect of composition on hydrogen absorbing properties in binary $TiMn_2$ based alloys. J Alloys Compd 2003;352:210–7.
[18] Reilly JJ, Wiswall RH. Formation and properties of iron titanium hydride. Inorg Chem 1974;13:218–22.
[19] Hagström MT, Vanhanen JP, Lund PD. AB_2 metal hydrides for high-pressure and narrow temperature interval applications. J Alloys Compd 1998;269:288–93.
[20] Klyamkin SN, Zakharkina NS. Hysteresis and related irreversible phenomena in $CeNi_5$-based intermetallic hydrides: I. Peculiarities of the first hydrogenation. J Alloys Compd 2003;361:200–5.
[21] Bernauer O, Töpler J, Noréus D, Hempelmann R, Richter D. Fundamentals and properties of some Ti/Mn based Laves phase hydrides. Int J Hydrogen Energy 1989;14:187–200.
[22] Skripnyuk VM, Ron M. Hydrogen desorption kinetics in intermetallic compounds C2, C51 and C52 with Laves phase structure. Int J Hydrogen Energy 2003;28:303–9.
[23] Taizhong H, Zhu W, Xuebin Y, Jinzhou C, Baojia X, Tiesheng H, et al. Hydrogen absorption-desorption behavior of zirconium-substituting Ti-Mn based hydrogen storage alloys. Intermetallics 2004;12:91–6.
[24] Yukawa H, Matsumura T, Morinaga M. Chemical bond state and hydride stability of hydrogen storage alloys. J Alloys Compd 1999;293-295:227–30.

APPENDIX B: A LIST OF MAJOR COMPANIES IN FUEL CELL TRANSPORTATION, SMALL STATIONARY AND PORTABLE SECTOR.

Several major fuel cell companies in the small stationary sector[29].

Company	Website	Location	Details
Altergy	www.altergy.com	USA	Fuel cell tacks and systems for the UPS market
ClearEdge	www.clearedgepower.com	USA	5 kW CE5 natural gas fuelled CHP unit
Ebara Ballard		Japan	JV between Ballard and Ebara, 1 kWe PEM system
Eneos Celltech		Japan	JV between Sanyo Electric and Nippon Oil, PEM and SOFC residential units
Hydrogenics	www.hydrogenics.com	USA	HyPM-XR for integration in UPS datacenter cabinets and HyUPS for mobile phone
IdaTech	www.idatech.com	USA	Has deal to supply up to 30,000 5kW UPS systems to the Indian ACME group
Matsushita		Japan	Delivered 650-1 kW stacks
P21	www.p-21.de	Germany	Pin out from Vodaphone, now supplies PEM UPS systems
Plug Power	www.plugpower.com	USA	GenSys low temperature units I being marketed to telecommunication sector
Toshiba FCP		Japan	1 kW wants to be shipping 40,000 units per annum in Japan by 2015

Major companies in the portable PEMFC sector[30].

Company	Website	Location	Details
CMR Fuel cells	Cmrfuelcells.com	UK	25 W hybrid DMFC laptop battery charger
Jadoo power systems	Adoopower.com	USA	Chemical hydride fuel cells, 100 W portable electric power supply for aeromedical evacuation applications
Horizon	Horizonfuelcell.com	China	H-racer series of toy and gadgets, hobbyist fuel cell systems
MTI micro	Timicrofuellcells.com	USA	Collaboration with equipment manufactures about external chargers including universal chargers
Neah power systems	Neahpower.com	USA	DMFC units
Samsung DSI	Amsungdi.com	Korea	Military DMFC battery with up to 800% more durability and 54% more power
Sony	sony.co.jp	Japan	DMFC powered recharging devices for laptops and mobile phones
Toshiba	Toshiba.co.jp	Japan	10 W DMFC battery charger

A list of key companies in the fuel cell transportation sector[31,32].

Company	Website	Location	Details
Ballard	ballard.com	Canada	FC forklifts; HD6, their next generation engine for hybrid fuel-cell buses
H2Logic	h2logic.com	Denmark	FC forklifts, focusing on the European market
Hydrogenics	hydrogenics.com	Canada	20 kW minibuses, APUs and range extenders
Nuvera	nuvera.com	USA	PowerEdge, hybrid FC forklifts, 82 kW FC bus
Oorja Protonics	oorjaprotonics.com	USA	DMFC-based charger for forklifts' batteries
Proton Motor	proton-motor.de	Germany	FC powered street sweeper, light duty truck
Tropical S.A.	tropical.gr	Greece	Hybrid FC bikes and scooters with the FC charging the battery
Protonex	PROTONEX.com	USA	APUs, UAVs (Unmanned Aerial Vehicles)
Volvo	volvo.com	Sweden	APUs

APPENDIX C: ITERATIVE SOLVING TECHNIQUE

Summary of an iterative solving technique in order to calculate the actual pressure for alane during absorption process heated at 323K, 373K and 423K respectively. This technique was applied in the case where a pressure indicator was not used.

Modified gas law is expressed as

$$\frac{P_1V_1}{Z_1R_1T_1} = \frac{P_2V_2}{Z_2R_2T_2}$$

whereP_1 ,V_1, T_1, $R_1$and $Z_1$are the initial pressure, volume, temperature, gas constant and compressibilitywhile P_2 ,V_2,T_2 and Z_2 are the final pressure, volume, temperature, gas constant and compressibility. Assumed both volume $(V_1 and V_2)$ and gas constant $(R_1 and R_2)$ are the same values.So the above equation can be derived as

$$\frac{P_1}{Z_1T_1} = \frac{P_2}{Z_2T_2}$$

For 298K

$$\frac{290.68}{(1.513).77} = \frac{P_2}{Z_2.298}$$

743.535 x Z_2 = P_2

TryZ_2 = 1.958(when pressure = 1500 bar)

743.535x 1.958 = 1455 bar

Try Z_2 = 1.931 (when pressure = 1455 bar)

743.535 x 1.931 = 1435bar

Try Z_2 = 1.919 (when pressure = 1435 bar)

743.535 x 1.919 = 1426bar

Try Z_2 = 1.913 (when pressure = 1426 bar)

743.535x 1.913 = 1422 bar

Try Z_2 = 1.911 (when pressure = 1422 bar)

917.082 x 1.911 = 1420 bar

So pressure was increased from 280 bar at 77K to 1420 bar at 298K.

For 323K

$$\frac{290.68}{(1.513).77} = \frac{P_2}{Z_2.323}$$

805.913 x Z_2 = P_2

TryZ_2 = 1.884 (when pressure = 1500 bar)

805.913 x 1.884 = 1518 bar

Try Z_2 = 1.894 (when pressure = 1518 bar)

805.913 x 1.894 = 1526bar

Try Z_2 = 1.898 (when pressure = 1526 bar)

805.913 x 1.898 = 1529bar

Try Z_2 = 1.9 (when pressure = 1529 bar)

805.913x 1.9 = 1531 bar

Try Z_2 = 1.901 (when pressure = 1531 bar)

805.913x 1.901 = 1532 bar

So pressure was increased from 280 bar at 77K to 1532 bar at 323K.

For 373K

$$\frac{290.68}{(1.513).77} = \frac{P_2}{Z_2.373}$$

930.667 x Z_2 = P_2

TryZ_2 = 1.765 (when pressure = 1500 bar)

930.667 x 1.765 = 1642 bar

Try Z_2 = 1.834 (when pressure = 1642 bar)

930.667x 1.834 = 1706bar

Try Z_2 = 1.864 (when pressure = 1706 bar)

930.667x 1.864 = 1734bar

So pressure was increased from 280 bar at 77K to 1734 bar at 373K.

For 423K

$$\frac{290.68}{(1.513).77} = \frac{P_2}{Z_2.423}$$

1055.421 x Z_2 = P_2

TryZ_2 = 1.675 (when pressure = 1500 bar)

1055.421 x 1.675 = 1767 bar

Try Z_2 = 1.787 (when pressure = 1767 bar)

1055.421x 1.787 = 1886bar

Try Z_2 = 1.835 (when pressure = 1886 bar)

1055.421x 1.835 = 1936bar

Try Z_2 = 1.855 (when pressure = 1936 bar)

1055.421x 1.855 = 1957 bar

Try Z_2 = 1.864 (when pressure = 1957 bar)

917.082 x 1.864 = 1967 bar

So pressure was increased from 280 bar at 77K to 1967 bar at 423K.

APPENDIX D: HYDROGEN SORPTION CALCULATIONS

Ambient sorption

The change in the number of moles of hydrogen at ambient temperature can be calculated by using

$$n_{ADS} = n_r + n_s - n_e$$

$$n_r = \frac{P_r V_r}{Z_r R T_r}$$

$$n_s = \frac{P_s\left(V_s - V_{sample}\right)}{Z_s R T_s}$$

$$n_e = \frac{P_e\left(V_r + V_s - V_{sample}\right)}{Z_e R T_e}$$

Where

n_r - the initial number of moles of hydrogen in the reference side volume

n_s - the initial number of moles of hydrogen in sample side volume

n_e - the final number of mole of hydrogen at equilibrium

V_r - the reference volume

V_s -the sample side volume

V_{sample} -the volume that the sample displaces within the sample side volume which can be calculated from its mass and density

P_r -the initial reference side pressure

P_s -the initial sample side pressure,

P_e -the final equilibrium pressure

T_r -the initial reference side temperature

T_s -the initial sample side temperature

T_e -the final equilibrium temperature

Z_r -the compressibility associated with P_r and T_r

Z_s -the compressibility associated with P_s and T_s

Z_e -the compressibility associated with P_e and T_e.

R –the universal gas constant (8.314472 $JK^{-1}mol^{-1}$)

.

Non-ambient sorption

The change in the number of mole of hydrogen at non-ambient temperature can be calculated by the following

$$n_{ADS} = n_r + n_s - n_e$$

$$n_r = \frac{P_r V_r}{Z_r R T_r}$$

$$n_s = \frac{P_s(V_s - V_{na})}{Z_s R T_s} + \frac{P_s\left(V_{na} - V_{sample}\right)}{Z_{na} R T_{na}}$$

$$n_e = \frac{P_e V_r}{Z_e R T_e} + \frac{P_e(V_s - V_{na})}{Z_e R T_e} + \frac{P_e\left(V_{na} - V_{sample}\right)}{Z_{ena} R T_{na}}$$

Where

n_r - the initial number of moles of hydrogen in the reference volume

n_s - the initial number of moles of hydrogen in sample side volume

V_{na} - the non-ambient sample side volume

n_e - the final number of mole of hydrogen at equilibrium

$V_r$is the reference volume

V_s - the sample side volume

V_{sample} -the volume that the sample displaces within the sample side volume which can be calculated from its mass and density

P_r -the initial reference pressure

P_s -the initial sample side pressure

P_e -the final equilibrium pressure

T_r -the initial reference temperature

T_s -theinitial sample side temperature

T_{na} -the non-ambient sample side temperature

T_e-the final equilibrium temperature

Z_r -the compressibility associated with the initial reference measurements

Z_s -the compressibility associated with the initial sample side measurements

Z_{na} -the compressibility associated with the initial ample side non-ambient measurements.

Z_e -the compressibility associated with the final equilibrium ambient temperature measurements

Z_{ena}-the compressibility associated with the final equilibrium non-ambient measurements.

R -the gas constant (8.314472 $JK^{-1}mol^{-1}$).

APPENDIX E: COPYRIGHT FORMS

Copies of copyright permission for use of 3rd party information/reproduction.

PERMISSION TO USE COPYRIGHT MATERIAL AS SPECIFIED BELOW:

Full article from the following article;

J.A. Murshidi, M. Paskevicius, D.A. Sheppard, C.E. Buckley. Structure, morphology and hydrogen storage properties of a $Ti_{0.97}Zr_{0.019}V_{0.439}Fe_{0.097}Cr_{0.045}Al_{0.026}Mn_{1.5}$ alloy. International Journal of Hydrogen Energy. Volume 36, Issue 13, July 2011, Pages 7587–7593.

I hereby give permission for **Julie Andrianny Murshidi** to include the abovementioned material in her higher degree thesis for the Curtin University of Technology, and to communicate this material via the Australasian Digital Thesis Program. This permission is granted on a non-exclusive basis and for an indefinite period.

I confirm that I am the copyright owner of the specified material.

Permission to use this material is subject to the following conditions: [Delete if not applicable]

Signed: E. Veziroglu

Name: EMRE A. VEZIROGLU

Position: EDITOR-IN-CHIEF, IJHE

Date: 11 AUG. 2012

Please return signed form to;

Julie Andrianny Murshidi
Department of Imaging and Applied Physics
GPO Box U1987 Perth
Western Australia 6845

Or email completed copy to;
j.murshidi@student.curtin.edu.au

PERMISSION TO USE COPYRIGHT MATERIAL AS SPECIFIED BELOW:

Figure 6 and 10 from the following article;

Gamo, T.; Moriwaki, Y.; Yanagihara, N.; Yamashita, T.; Iwaki, T. Formation and properties of titanium-manganese alloy hydrides. International Journal of Hydrogen Energy. Volume 10, Issue 1, 1985, Pages 39–47.

I hereby give permission for **Julie Andrianny Murshidi** to include the abovementioned material in her higher degree thesis for the Curtin University of Technology, and to communicate this material via the Australasian Digital Thesis Program. This permission is granted on a non-exclusive basis and for an indefinite period.

I confirm that I am the copyright owner of the specified material.

Permission to use this material is subject to the following conditions: [Delete if not applicable]

Signed: E. Veziroglu

Name: EMRE A. VEZIROGLU

Position: EDITOR-IN-CHIEF, IJHE

Date: 11 AUG. 2012

Please return signed form to;

Julie Andrianny Murshidi
Department of Imaging and Applied Physics
GPO Box U1987 Perth
Western Australia 6845

Or email completed copy to;
j.murshidi@student.curtin.edu.au

PERMISSION TO USE COPYRIGHT MATERIAL AS SPECIFIED BELOW:

Figure 1 and 3 from the following article;

I.P. Jain. Hydrogen the fuel for 21st century. International Journal of Hydrogen Energy, Volume 34, Issue 17, September 2009, Pages 7368-7378.

I hereby give permission for **Julie Andrianny Murshidi** to include the abovementioned material in her higher degree thesis for the Curtin University of Technology, and to communicate this material via the Australasian Digital Thesis Program. This permission is granted on a non-exclusive basis and for an indefinite period.

I confirm that I am the copyright owner of the specified material.

Permission to use this material is subject to the following conditions: [Delete if not applicable]

Signed: E. Veziroglu

Name: EMRE A. VEZIROGLU

Position: EDITOR-IN-CHIEF, IJHE

Date: 11 AUG. 2012

Please return signed form to;

Julie Andrianny Murshidi
Department of Imaging and Applied Physics
GPO Box U1987 Perth
Western Australia 6845

Or email completed copy to;
j.murshidi@student.curtin.edu.au

PERMISSION TO USE COPYRIGHT MATERIAL AS SPECIFIED BELOW:

Figure 5 from the following article;

Bobet, J. L.; Darriet, B. Relationship between hydrogen sorption properties and crystallography for $TiMn_2$ based alloys. International Journal of Hydrogen Energy. Volume 25, Issue 8, 1 August 2000, Pages 767-772.

I hereby give permission for **Julie Andrianny Murshidi** to include the abovementioned material in her higher degree thesis for the Curtin University of Technology, and to communicate this material via the Australasian Digital Thesis Program. This permission is granted on a non-exclusive basis and for an indefinite period.

I confirm that I am the copyright owner of the specified material.

Permission to use this material is subject to the following conditions: [Delete if not applicable]

Signed: E. Veziroglu

Name: EMRE A. VEZIROGLU

Position: EDITOR-IN-CHIEF, IJHE

Date: 11 AUG. 2012

Please return signed form to;

Julie Andrianny Murshidi
Department of Imaging and Applied Physics
GPO Box U1987 Perth
Western Australia 6845

Or email completed copy to;
j.murshidi@student.curtin.edu.au

PERMISSION TO USE COPYRIGHT MATERIAL AS SPECIFIED BELOW:

Figure 2 from the following article;

Singh, B. K.; Singh, A. K.; Imam, A. M.; Srivastava, O. N. On the structural characteristics and hydrogenation behaviour of TiMn1.5 hydrogen storage material. International Journal of Hydrogen Energy. Volume 26, Issue 8, August 2001, Pages 817-821.

I hereby give permission for **Julie Andrianny Murshidi** to include the abovementioned material in her higher degree thesis for the Curtin University of Technology, and to communicate this material via the Australasian Digital Thesis Program. This permission is granted on a non-exclusive basis and for an indefinite period.

I confirm that I am the copyright owner of the specified material.

Permission to use this material is subject to the following conditions: [Delete if not applicable]

Signed: E. Veziroglu

Name: EMRE A. VEZIROGLU

Position: EDITOR-IN-CHIEF, IJHE

Date: 11 AUG. 2012

Please return signed form to;

Julie Andrianny Murshidi
Department of Imaging and Applied Physics
GPO Box U1987 Perth
Western Australia 6845

Or email completed copy to;
j.murshidi@student.curtin.edu.au

PERMISSION TO USE COPYRIGHT MATERIAL AS SPECIFIED BELOW:

Figure 4 from the following article;

Chu, H.; Zhang, Y.; Sun, L.; Qiu, S.; Xu, F.; Yuan, H.; Wang, Q.; Chuang, D. Structure, morphology and hydrogen storage properties of composites prepared by ball milling $Ti_{0.9}Zr_{0.2}Mn_{1.5}Cr_{0.3}V_{0.3}$ with La-Mg-based alloy. International Journal of Hydrogen Energy. Volume 32, Issue 15, October 2007, Pages 3363-3369.

I hereby give permission for **Julie Andrianny Murshidi** to include the abovementioned material in her higher degree thesis for the Curtin University of Technology, and to communicate this material via the Australasian Digital Thesis Program. This permission is granted on a non-exclusive basis and for an indefinite period.

I confirm that I am the copyright owner of the specified material.

Permission to use this material is subject to the following conditions: [Delete if not applicable]

Signed:

Name:
Emre A. Veziroglu

Position:
Editor – in Chief, International Journal of Hydrogen Energy

Date:
1 September 2012

Please return signed form to;

Julie Andrianny Murshidi
Department of Imaging and Applied Physics
GPO Box U1987 Perth
Western Australia 6845

Or email completed copy to;
j.murshidi@student.curtin.edu.au

License Details

This is a License Agreement between JULIE ANDRIANNY MURSHIDI ("You") and Elsevier ("Elsevier"). The license consists of your order details, the terms and conditions provided by Elsevier, and the payment terms and conditions.

Get the printable license.

License Number	2962910178001
License date	Aug 06, 2012
Licensed content publisher	Elsevier
Licensed content publication	Materials Today
Licensed content title	Materials for hydrogen storage
Licensed content author	Andreas Züttel
Licensed content date	September 2003
Licensed content volume number	6
Licensed content issue number	9
Number of pages	10
Type of Use	reuse in a thesis/dissertation
Portion	figures/tables/illustrations
Number of figures/tables/illustrations	1
Format	both print and electronic
Are you the author of this Elsevier article?	No
Will you be translating?	No
Order reference number	None
Title of your thesis/dissertation	HYDROGEN STORAGE STUDIES OF NANOPARTICULATE Al AND TiMn BASED COMPOUNDS
Expected completion date	Sep 2012
Estimated size (number of pages)	150
Elsevier VAT number	GB 494 6272 12
Permissions price	0.00 USD
VAT/Local Sales Tax	0.0 USD / 0.0 GBP
Total	0.00 USD

License Details

This is a License Agreement between JULIE ANDRIANNY MURSHIDI ("You") and Elsevier ("Elsevier"). The license consists of your order details, the terms and conditions provided by Elsevier, and the payment terms and conditions.

Get the printable license.

License Number	2962900042757
License date	Aug 06, 2012
Licensed content publisher	Elsevier
Licensed content publication	Journal of Alloys and Compounds
Licensed content title	A panoramic overview of hydrogen storage alloys from a gas reaction point of view
Licensed content author	Gary Sandrock
Licensed content date	20 December 1999
Licensed content volume number	293–295
Number of pages	12
Type of Use	reuse in a thesis/dissertation
Portion	figures/tables/illustrations
Number of figures/tables/illustrations	1
Format	both print and electronic
Are you the author of this Elsevier article?	No
Will you be translating?	No
Order reference number	None
Title of your thesis/dissertation	HYDROGEN STORAGE STUDIES OF NANOPARTICULATE Al AND TiMn BASED COMPOUNDS
Expected completion date	Sep 2012
Estimated size (number of pages)	150
Elsevier VAT number	GB 494 6272 12
Permissions price	0.00 USD
VAT/Local Sales Tax	0.0 USD / 0.0 GBP
Total	0.00 USD

License Details

This is a License Agreement between JULIE ANDRIANNY MURSHIDI ("You") and Elsevier ("Elsevier"). The license consists of your order details, the terms and conditions provided by Elsevier, and the payment terms and conditions.

Get the printable license.

License Number	2963420232332
License date	Aug 06, 2012
Licensed content publisher	Elsevier
Licensed content publication	Journal of Alloys and Compounds
Licensed content title	Thermodynamics of hydride formation and decomposition for TiMn2-H2system at pressure up to 2000 atm
Licensed content author	S.N. Klyamkin,V.N. Verbetsky,V.A. Demidov
Licensed content date	March 1994
Licensed content volume number	205
Licensed content issue number	1–2
Number of pages	2
Type of Use	reuse in a thesis/dissertation
Portion	figures/tables/illustrations
Number of figures/tables/illustrations	1
Format	both print and electronic
Are you the author of this Elsevier article?	No
Will you be translating?	No
Order reference number	None
Title of your thesis/dissertation	HYDROGEN STORAGE STUDIES OF NANOPARTICULATE Al AND TiMn BASED COMPOUNDS
Expected completion date	Sep 2012
Estimated size (number of pages)	150
Elsevier VAT number	GB 494 6272 12
Permissions price	0.00 USD
VAT/Local Sales Tax	0.0 USD / 0.0 GBP

License Details

This is a License Agreement between JULIE ANDRIANNY MURSHIDI ("You") and Elsevier ("Elsevier"). The license consists of your order details, the terms and conditions provided by Elsevier, and the payment terms and conditions.

Get the printable license.

License Number	2962910288674
License date	Aug 06, 2012
Licensed content publisher	Elsevier
Licensed content publication	Intermetallics
Licensed content title	Mechanical milling/alloying of intermetallics
Licensed content author	C.C. Koch,J.D. Whittenberger
Licensed content date	1996
Licensed content volume number	4
Licensed content issue number	5
Number of pages	17
Type of Use	reuse in a thesis/dissertation
Portion	figures/tables/illustrations
Number of figures/tables/illustrations	1
Format	both print and electronic
Are you the author of this Elsevier article?	No
Will you be translating?	No
Order reference number	None
Title of your thesis/dissertation	HYDROGEN STORAGE STUDIES OF NANOPARTICULATE Al AND TiMn BASED COMPOUNDS
Expected completion date	Sep 2012
Estimated size (number of pages)	150
Elsevier VAT number	GB 494 6272 12
Permissions price	0.00 USD
VAT/Local Sales Tax	0.0 USD / 0.0 GBP
Total	0.00 USD

License Details

This is a License Agreement between JULIE ANDRIANNY MURSHIDI ("You") and Elsevier ("Elsevier"). The license consists of your order details, the terms and conditions provided by Elsevier, and the payment terms and conditions.

Get the printable license.

License Number	2962931186902
License date	Aug 06, 2012
Licensed content publisher	Elsevier
Licensed content publication	Journal of Alloys and Compounds
Licensed content title	Aluminum hydride as a hydrogen and energy storage material: Past, present and future
Licensed content author	J. Graetz,J.J. Reilly,V.A. Yartys,J.P. Maehlen,B.M. Bulychev,V.E. Antonov,B.P. Tarasov,I.E. Gabis
Licensed content date	September 2011
Licensed content volume number	509
Licensed content issue number	ment 2
Number of pages	12
Type of Use	reuse in a thesis/dissertation
Portion	figures/tables/illustrations
Number of figures/tables/illustrations	5
Format	both print and electronic
Are you the author of this Elsevier article?	No
Will you be translating?	No
Order reference number	None
Title of your thesis/dissertation	HYDROGEN STORAGE STUDIES OF NANOPARTICULATE Al AND TiMn BASED COMPOUNDS
Expected completion date	Sep 2012
Estimated size (number of pages)	150
Elsevier VAT number	GB 494 6272 12
Permissions price	0.00 USD
VAT/Local Sales Tax	0.0 USD / 0.0 GBP
Total	0.00 USD

License Details

This is a License Agreement between JULIE ANDRIANNY MURSHIDI ("You") and Elsevier ("Elsevier"). The license consists of your order details, the terms and conditions provided by Elsevier, and the payment terms and conditions.

Get the printable license.

License Number	2962821278546
License date	Aug 05, 2012
Licensed content publisher	Elsevier
Licensed content publication	Current Opinion in Solid State & Materials Science
Licensed content title	Materials-based hydrogen storage: Attributes for near-term, early market PEM fuel cells
Licensed content author	Scott McWhorter,Carole Read,Grace Ordaz,Ned Stetson
Licensed content date	April 2011
Licensed content volume number	15
Licensed content issue number	2
Number of pages	10
Type of Use	reuse in a thesis/dissertation
Portion	figures/tables/illustrations
Number of figures/tables/illustrations	1
Format	electronic
Are you the author of this Elsevier article?	No
Will you be translating?	No
Order reference number	None
Title of your thesis/dissertation	HYDROGEN STORAGE STUDIES OF NANOPARTICULATE Al AND TiMn BASED COMPOUNDS
Expected completion date	Sep 2012
Estimated size (number of pages)	150
Elsevier VAT number	GB 494 6272 12
Permissions price	0.00 USD
VAT/Local Sales Tax	0.0 USD / 0.0 GBP
Total	0.00 USD

License Details

This is a License Agreement between JULIE ANDRIANNY MURSHIDI ("You") and Springer ("Springer"). The license consists of your order details, the terms and conditions provided by Springer, and the payment terms and conditions.

Get the printable license.

License Number	2962941396726
License date	Aug 06, 2012
Licensed content publisher	Springer
Licensed content publication	Journal of Phase Equilibria (and diffusion)
Licensed content title	Thermodynamic evaluation of the Al-H system
Licensed content author	Caian Qiu
Licensed content date	Jan 1, 2004
Volume number	25
Issue number	6
Type of Use	Thesis/Dissertation
Portion	Figures
Author of this Springer article	No
Title of your thesis / dissertation	HYDROGEN STORAGE STUDIES OF NANOPARTICULATE Al AND TiMn BASED COMPOUNDS
Expected completion date	Sep 2012
Estimated size(pages)	150
Total	0.00 USD

License Details

This is a License Agreement between JULIE ANDRIANNY MURSHIDI ("You") and Elsevier ("Elsevier"). The license consists of your order details, the terms and conditions provided by Elsevier, and the payment terms and conditions.

Get the printable license.

License Number	2978521377107
License date	Aug 29, 2012
Licensed content publisher	Elsevier
Licensed content publication	Journal of Alloys and Compounds
Licensed content title	The location of Ti containing phases after the completion of the NaAlH4+*x*TiCl3milling process
Licensed content author	M.P. Pitt,P.E. Vullum,M.H. Sørby,D. Blanchard,M.P. Sulic,H. Emerich,M. Paskevicius,C.E. Buckley,J. Walmsley,R. Holmestad,B.C. Hauback
Licensed content date	5 February 2012
Licensed content volume number	513
Number of pages	9
Type of Use	reuse in a thesis/dissertation
Portion	figures/tables/illustrations
Number of figures/tables/illustrations	1
Format	both print and electronic
Are you the author of this Elsevier article?	No
Will you be translating?	No
Order reference number	None
Title of your thesis/dissertation	HYDROGEN STORAGE STUDIES OF NANOPARTICULATE Al AND TiMn BASED COMPOUNDS
Expected completion date	Sep 2012
Estimated size (number of pages)	150
Elsevier VAT number	GB 494 6272 12
Permissions price	0.00 USD
VAT/Local Sales Tax	0.0 USD / 0.0 GBP
Total	0.00 USD

License Details

This is a License Agreement between JULIE ANDRIANNY MURSHIDI ("You") and Springer ("Springer"). The license consists of your order details, the terms and conditions provided by Springer, and the payment terms and conditions.

Get the printable license.

License Number	2962931431435
License date	Aug 06, 2012
Licensed content publisher	Springer
Licensed content publication	Doklady Physical Chemistry
Licensed content title	Kinetics of Formation of Metallic Aluminum upon Thermal and Photolytic Decomposition of Aluminum Trihydride and Trideuteride as Probed by NMR
Licensed content author	V. P. Tarasov
Licensed content date	Dec 1, 2003
Volume number	393
Issue number	4
Type of Use	Thesis/Dissertation
Portion	Figures
Author of this Springer article	No
Country of republication	other
Title of your thesis / dissertation	HYDROGEN STORAGE STUDIES OF NANOPARTICULATE Al AND TiMn BASED COMPOUNDS
Expected completion date	Sep 2012
Estimated size(pages)	150
Total	0.00 USD

License Details

This is a License Agreement between JULIE ANDRIANNY MURSHIDI ("You") and Elsevier ("Elsevier"). The license consists of your order details, the terms and conditions provided by Elsevier, and the payment terms and conditions.

Get the printable license.

License Number	2962940318000
License date	Aug 06, 2012
Licensed content publisher	Elsevier
Licensed content publication	Journal of Alloys and Compounds
Licensed content title	Alkali metal hydride doping of α-AlH3for enhanced H2desorption kinetics
Licensed content author	Gary Sandrock,James Reilly,Jason Graetz,Wei-Min Zhou,John Johnson,James Wegrzyn
Licensed content date	14 September 2006
Licensed content volume number	421
Licensed content issue number	1–2
Number of pages	5
Type of Use	reuse in a thesis/dissertation
Portion	figures/tables/illustrations
Number of figures/tables/illustrations	1
Format	both print and electronic
Are you the author of this Elsevier article?	No
Will you be translating?	No
Order reference number	None
Title of your thesis/dissertation	HYDROGEN STORAGE STUDIES OF NANOPARTICULATE Al AND TiMn BASED COMPOUNDS
Expected completion date	Sep 2012
Estimated size (number of pages)	150
Elsevier VAT number	GB 494 6272 12
Permissions price	0.00 USD
VAT/Local Sales Tax	0.0 USD / 0.0 GBP
Total	0.00 USD

License Details

This is a License Agreement between JULIE ANDRIANNY MURSHIDI ("You") and Elsevier ("Elsevier"). The license consists of your order details, the terms and conditions provided by Elsevier, and the payment terms and conditions.

Get the printable license.

License Number	2962930154724
License date	Aug 06, 2012
Licensed content publisher	Elsevier
Licensed content publication	Journal of Alloys and Compounds
Licensed content title	Stability enhancement by particle size reduction in AlH3
Licensed content author	P. Vajeeston,P. Ravindran,H. Fjellvåg
Licensed content date	September 2011
Licensed content volume number	509
Licensed content issue number	ment 2
Number of pages	5
Type of Use	reuse in a thesis/dissertation
Portion	figures/tables/illustrations
Number of figures/tables/illustrations	2
Format	both print and electronic
Are you the author of this Elsevier article?	No
Will you be translating?	No
Order reference number	None
Title of your thesis/dissertation	HYDROGEN STORAGE STUDIES OF NANOPARTICULATE Al AND TiMn BASED COMPOUNDS
Expected completion date	Sep 2012
Estimated size (number of pages)	150
Elsevier VAT number	GB 494 6272 12
Permissions price	0.00 USD
VAT/Local Sales Tax	0.0 USD / 0.0 GBP
Total	0.00 USD

To: permissions@iop.org,
Cc:
Bcc:
Subject: Permission to use copyright material from journal Nanotechnology
From: Julie Andrianny <julieanndrianny@gmail.com> - Wednesday 08/08/2012 02:01

2 attachments

PermissionLetterKiChulKim.docx IMG_0001.pdf

Dear Sir/Madam,

Attached are the documents to get permission to use copyright material from journal Nanotechnology. I look forward to hearing from you and thank you in advance for your cooperation of my request.

PERMISSION TO REPRODUCE AS REQUESTED IS GIVEN PROVIDED THAT:

(a) the consent of the author(s) is obtained
(b) the source of the material including author, title of article, title of journal, volume number, issue number (if relevant), page range (or first page if this is the only information available), date and publisher is acknowledged.
(c) for material being published electronically, a link back to the original article should be provided (via DOI).

IOP Publishing Ltd
Temple Circus
Temple Way
BRISTOL
BS1 6BE

09/08/2012
Date

Sarah Ryde
Rights & Permissions